

STUDY OF ACTIVE NEMATICS: CONTINUUM THEORY AND
PARTICLE SIMULATIONS

By

Sheng Chen

A DISSERTATION

Submitted to
Michigan State University
in partial fulfillment of the requirements
for the degree of

Mechanical Engineering – Doctor of Philosophy

2021

ABSTRACT

STUDY OF ACTIVE NEMATICS: CONTINUUM THEORY AND PARTICLE SIMULATIONS

By

Sheng Chen

The concept of ‘active matter’ refers to a system that is far away from equilibrium. It comprises internal self-driven units that consume a local fuel (e.g., chemical fuel) from surroundings and transforms it into mechanical work. It is ubiquitous not only in the macroworld such as flocking of fish, birds or animal herds, but also pervasive in the microworld. Examples include biological swimmers such as bacteria and microalgae, synthetic colloidal surfers actuated by chemical reactions, as well as purified biopolymers (e.g., microtubules (MTs)) mixed with molecular motors. In contrast to the previously well-studied passive systems where the instability mainly comes from the thermodynamic fluctuations, the inherent spontaneity of the active matter endows itself with a complex and ever-changing dynamics and structure, the study of which is still nascent.

In this thesis, we focus primarily on a specific type of active system in the microscale that is featured by comprising self-driven particles with elongated shape, i.e., the rod-like particles. Such system is described as ‘active nematics’ due to its resemblance to nematic liquid crystals. The out-of-equilibrium pattern formation of active nematics is caused by the inextricable interplay between the short-range steric interaction and the long-range hydrodynamics. As a result, the dynamics and structure of active nematics display hallmarks of

collective motion of particles, chaotic flow structure and the concomitantly long-ranged nematic order and motile topological defect. To gain a physical insight to such complex while intriguing phenomena, we develop a coarse-grained Q-tensor continuum theory coupled with low-Reynold fluid dynamics. With the assistance of computational framework for simulating suspensions of rigid particles in Newtonian Stokes flow, we are able to conduct large-scale particle simulations to mimic many-particle couplings.

The thesis is organized as follows: In chapter 1, we study the complex dynamics of a two-dimensional suspension comprising non-motile active particles confined in an annulus. A coarse-grained liquid crystal model is employed to describe the nematic structure evolution, and hydrodynamically couples with the Stokes equation to solve for the induced active flows in the annulus. In chapter 2, We study fluid and mass transport in a dilute apolar active suspension confined in a rectangular channel. By using a Galerkin mixed finite element method, we are able to reveal various patterns of spontaneous coherent flows that can be unidirectional, traveling-wave, and chaotic. In chapter 3, we study the long-time rotational Brownian diffusivity in a crowded bath of hard rods with finite aspect ratios, where the topological constraint dominate over hydrodynamics. In chapter 4, we study the nonlinear dynamics of an undulatory microswimmer in a quasi-2D liquid-crystal polymer solution.

ACKNOWLEDGMENTS

In the first place, my sincere gratitude goes to my advisor Dr. Tong Gao for his mentoring and support throughout my PhD period and the completion of this dissertation. His expertise in fluid mechanics and mathematics lays a sound theoretical foundation for my research at Michigan State University and I believe will definitely have a far-reaching impact on my future study. Also thanks for his friendly advice on my career plans and his heartwarming support during my hard times.

Besides this, I would like to thank my thesis committee members, Dr. Yingda Cheng, Dr. Farhad Jaber, and Dr. André Bénard for their support and suggestions to this dissertation, and for their great course in computational fluid mechanics. I appreciate Dr. Chang Wang for his course in perturbation theory. The perturbation techniques I learned from Dr. Wang and my advisor Dr. Gao accounts for a considerable proportion of my theoretical study. I also thank Dr. Charles Petty for his multiphase fluids course that is beneficial to my research and thanks Dr. Indrek Wichman for being my teaching mentor.

I am also deeply grateful to my group colleagues: Dr. Andrew Michael Hess, and Dr. Zhaowu Lin. Their kindly assistance, expertise in different research field contribute to the completion of different part of this thesis.

Last but not least, I would like to thank my parents and my grandma for their unconditional support and love. Thank Jing Ke, for being both a best friend and a soulmate all the way through.

TABLE OF CONTENTS

LIST OF FIGURES	vii
1 DYNAMICS AND STRUCTURE OF AN APOLAR ACTIVE SUSPENSION IN AN ANNULUS	1
1.1 Abstract	1
1.2 Introduction	1
1.3 Mathematical model	4
1.4 Results and Discussion	6
1.4.1 Dilute Suspension	7
1.4.2 Concentrated Suspension	15
1.5 Conclusion	19
2 TRANSPORT OF AN APOLAR ACTIVE SUSPENSION IN A RECTANGULAR CHANNEL	21
2.1 Abstract	21
2.2 Introduction	22
2.3 Mathematical model	25
2.4 Analysis and simulation results	27
2.4.1 Spontaneous Coherent Flows	27
2.4.2 Concatenation of Hydrodynamic Instabilities	28
2.4.3 Active Transport of Circular Cylinders	34
2.5 Conclusion	39
3 SCALING LAW OF BROWNIAN ROTATION IN CONCENTRATED HARD-ROD SUSPENSIONS	41
3.1 Abstract	41
3.2 Introduction	41
3.3 Numerical method	44
3.3.1 Complementarity formulation and equation of motion	44
3.4 Results	46
3.4.1 Equilibrium PDF of the Doi-Onsager Model	46
3.4.2 Measuring D_r from quadratic OACFs	49
3.4.3 Scaling law delineated by modified tube model	53
3.4.4 Approximations of the double-configurational averages	58
3.5 Conclusion	59
3.6 Future plan	60
4 Q -TENSOR MODEL FOR UNDULATORY SWIMMING IN A LIQUID CRYSTAL	61

4.1 Abstract	61
4.2 Introduction	62
4.3 Mathematical Model	64
4.4 Numerical method	68
4.5 Asymptotic analysis	72
4.5.1 Isotropic cases	75
4.5.2 Nearly-aligned cases	78
4.6 Results and Discussion	80
4.7 Conclusion	88
5 PUBLICATION	90
BIBLIOGRAPHY	92

LIST OF FIGURES

- Figure 1.1: (a-c) Characteristic flow patterns (streamline overlaid on the colormap of vorticity Ω) and (d-f) nematic structures (nematic director \mathbf{m} field overlaid on the colormap of scalar order parameter s) when choosing $R_1 = 1.0$ and $R_2 = 2.0$. Insets in (a) and (d) are the comparisons between the analytical (solid lines) and numerical (open circles) results for normalized u_θ and $D_{r\theta}$ components taken along the white lines when $|\alpha|$ slightly goes beyond the critical value $|\alpha|_{cr} = 1.23$ for the Isotropy-Circulation instability. (g) Phase diagram of $(|\alpha|, R_2 - R_1)$ when fixing $R_1 = 1.0$. The solid and dashed lines characterize the Isotropy-Circulation instability in an annulus and a straight channel, respectively. The dash-dot line characterizes the Circulation-Traveling wave instability in a straight channel for sharply-aligned rods by neglecting the rotational diffusion. 7
- Figure 1.2: (a) Growth rate $\text{Re}(\sigma)$ for the long-wave (diamonds) and finite-wavelength (lines) instabilities as a function of wavenumber k for Isotropy-Circulation instabilities in a periodic straight channel when choosing $h = 0.5$, $d_T = d_R = 0.025$. (b) Streamlines overlaid on the colormap of u velocity component at $\alpha = -4.0$. (c) Velocity profiles at $\alpha = -2.0$ ($u_{max} = 0.07$) and $\alpha = -4.0$ ($u_{max} = 0.13$), respectively. 9
- Figure 1.3: (a) Growth rate $\text{Re}(\sigma)$ as a function of wavenumber k for bending instabilities of the sharply-aligned Extensors when confined in a periodic straight channel when choosing $h = 0.5$, $d_R = 0$ and $d_T = 0.025$. The maximum growth rates at the critical wavenumbers k_{cr} are marked by solid circles. (b) and (c) show the vorticity field Ω as bending instability start to grow at $\alpha = -4.0$ and $\alpha = -8.0$, respectively. The solid black scales represent the length scales π/k_{cr} that match the separation distance between the neighboring vortices. 10

Figure 1.4: Equilibrium solutions of nematically-aligned states at different values of α when choosing $R_1 = 1.0$ and $R_2 = 2.0$, nematic director field overlaid on the colormap of s . Inset in panel(d): Comparisons between the analytical (solid line) and numerical (open symbols) results at $\alpha = -0.5, -2.0$ for D_{rr} component. The numerical data are taken along the white line marked in panel(c).	16
Figure 1.5: Evolution of the flow patterns for a concentrated Extensor suspension when choosing $\alpha = -2.0$, $R_1 = 1.0$ and $R_2 = 2.0$. Insets: nematic director field overlaid on the colormap of s . . .	17
Figure 1.6: Flow patterns (streamline overlaid on the colormap of Ω , upper row) and nematic structures (nematic director field overlaid on the colormap of s , lower row) that characterize the long-time dynamics of a confined Extensor suspension when choosing $\alpha = -2.0$, $R_1 = 0.75$ and $R_2 = 2.0$	17
Figure 1.7: Short-time evolution of the flow (velocity vector overlaid the colormap of on Ω , upper row) and nematic (nematic director overlaid on the colormap of s , lower row) fields for the case shown in figure 1.6. In (e-h), the black arrows shows the direction of the crack formation and $+1/2$ defect movement. . .	18
Figure 2.1: Typical (quasi-)steady coherent flows (a,c,e) and nematic orders (b,d,f) for unidirectional flow (a,b), traveling wave (c,d), and chaos (e,f). Simulations are performed when choosing the half channel width $H = 0.5$, $d_R = d_T = 0.025$, and $\alpha = -2.0, -8.0, -20.0$. Comparison of simulation and analytical solutions of the velocity profile is shown in inset of (a) where the maximum velocity is $u_{max} = 0.57$. (g) Phase diagram of $(\alpha , 2H)$. The solid line are the marginal stability curves from the analyses of the Q-U and U-T instabilities. The dashed lines are the predictions using the geometrically-selected high-order modes. The dotted line is our previous prediction when using a sharp-alignment assumption ([1]).	23

- Figure 2.2: Unstable modes and growth rates $\text{Re}(\sigma)$ of linear stability analyses for Q-U (a), U-T (b), and T-C (c) instabilities. In (a,b), the channel width is chosen as $H = 0.5$; in (c), $\alpha = -4.0$ is fixed. The open diamond symbols (in panel(a) at $k = 0$) represent the long-wavelength (M0) mode associated with the unidirectional flow solution. The solid, dashed, and dotted lines in (a-c) represent the 1st (M1), 2nd (M2), and 3rd (M3) unstable modes, corresponding to the single, double, and triple vortex arrays, respectively. The colorfields for vorticity and streamlines exhibit flow patterns, and are selected at the critical wavenumbers (circular red dots). 32
- Figure 2.3: Active flow past a fixed cylinder of $R = 0.1$ in the channel center: rescaled (a) u and (b) v velocity component, and the surface distribution of (c) pressure force, (d) viscous force, and (e) active force. In (a)-(e), the upper row are the simulation results when choosing $\alpha = -2.0$, and the bottom row shows the normalized analytical results. 34
- Figure 2.4: Transport of free-moving cylinders in active flows. (a) FEM results of typical time evolutions of the migration velocities for cylinders of different sizes when choosing $\alpha = -2.0$ and $H = 0.5$. (b) Solid lines represent the normalized steady-state migration velocities as functions of re-scaled radius. Symbols are the FEM results. (c) FEM results of cylinder trajectories ($R = 0.1$) in traveling wave flows. (d) FEM results of time-averaged velocity profiles at different cylinder volume fractions when choosing $R = 0.1$ and $H = 0.5$. The solid and dashed lines correspond to $\alpha = -4.0$ and -6.0 , respectively. . . 38
- Figure 3.1: Equilibrium orientational order parameter S as a function of ϕ . The open squares represent the GCBD simulation data. The solid lines are calculated using Ψ_{eq} in Eq. (3.12). Inset: Instantaneous snapshots at $\phi = 20\%$ and 40% for $\gamma = 10$ correspond to the I and N phase, respectively. 47
- Figure 3.2: Examples of orientational PDF for $\gamma = 10$ at $\phi = 20\%, 30\%, 40\%$. Open squares represent the GCBD data, and the solid lines represent the results by using Ψ_{eq} in Eq.(2) in the main text. 48

Figure 3.3: Orientation relaxation characterized by $\langle \mathbf{p}(t) \cdot \mathbf{p}(0) \rangle$ (a) and $\langle (\mathbf{p}(t) \cdot \mathbf{p}(0))^2 \rangle$ (b) across ϕ for $\gamma = 20$. The open symbols represent the GCBD data. Schematics of configurational space of $\mathbf{p}(t)$ are highlighted at the bottom for the different phases. In panel(b), the solid lines represent the fitting function in Eq. (3.13). Inset: Zoom-in window highlights that the short-time relaxation of OACF fits an exponential decay governed by a single time scale τ_R 50

Figure 3.4: D_r/D_{r0} as functions of $n\ell^3$ across ϕ for various γ . The open squares represent the data extracted from GCBD simulations via Eq. (3.18). The solid and dashed lines represent the scaling laws in Eq. (3.20) and (3.25), respectively. The solid red square on the $\gamma = 20$ curve marks the location of the data for fitting β . Inset: $\langle |\mathbf{p} \times \mathbf{p}'| \rangle_{p'}^p$ and $\langle |\mathbf{p} \cdot \mathbf{p}'| \rangle_{p'}^p$ as functions of S , evaluated by using Ψ_{eq} (solid lines) and the quadratic-closure approximation (dashed lines) [2], respectively. 53

Figure 3.5: GCBD simulations motivate a new *tube* model. (a) Schematic of a virtual *tube* with penetrations from both the sidewall and the two ends. (b) Fractional contributions of the averaged collision numbers on the sidewall (λ_I) and the ends (λ_{II}) for $\gamma = 5$ and 20 as functions of ϕ . (c) The collision number ratio $\lambda_I/(\gamma\lambda_{II})$ as functions of S for various γ . (d) The OPCF $g(r_\perp)$ in the nematic regime as functions of the dimensionless transverse distance r_\perp/b 56

Figure 4.1: Convergence tests of a parallel moving swimmer with the time-dependent C.O.M. velocity $\mathbf{U}(U_x, U_y)$ by varying (a) domain size ($\Delta t = 6.25 \times 10^{-5}$, $h = 1/128$), (b) Eulerian grid width ($\Omega_f = 2 \times 2$), and (c) Lagrangian grid spacing ($\Omega_f = 2 \times 2$, $h = 1/128$). These parameters are fixed: $Pe = 10$, $Pe_t = 100$, $Er = 1$, $\beta = 0.005$, $\zeta = 8$, $L = 1$, $A = 0.05$, $k = 2\pi$, $\omega = 2\pi$, $\sigma_b = 0.5$, $\sigma_s = 1500$ 69

Figure 4.2: Time-averaged C.O.M. speed U_{OB} for undulatory swimming motion in an Oldroyd-B fluid. These parameters are fixed: $\Omega_f = 8 \times 8$, $h = 1/64$, $N_s = 64$, $\eta_p/\eta_s = 1/2$, $L = 4$, $De = 1$, and $\Delta t = 2.5 \times 10^{-4}$ 72

- Figure 4.3: The time-dependent C.O.M. velocity $\mathbf{U}(U_x, U_y)$ for a parallel moving swimmer when choosing different values of bending stiffness σ_b . These parameters are fixed: $\Omega_f = 2 \times 2$, $\Delta t = 6.25 \times 10^{-4}$, $h = 1/128$, $Pe = 10$, $Pe_t = 100$, $Er = 1$, $\beta = 0.005$, $\zeta = 8$, $L = 1$, $N_s = 32$, $A = 0.05$, $k = 2\pi$, $\omega = 2\pi$, $\sigma_s = 1500$ 73
- Figure 4.4: I-N phase transition led anisotropic swimming. (a) δ as a function of ζ , with the bifurcation occurring at $\zeta_c = 4$. (b) Constant and apolar distribution of $\Psi_0(\phi)$ at $\zeta = 0$ and 8. (c) U_{LC}/U_N as a function of ζ for stiff ($\sigma_b = 0.5$) and soft ($\sigma_b = 0.005$) swimmer when choosing $Pe = 1$ and $Er = 10$, for the parallel (denoted by “||”) and perpendicular (denoted by “ \perp ”) motions. 81
- Figure 4.5: Speed ratio U_{LC}/U_N as a function of Pe at $Er = 1$ and 10 obtained from numerical simulation (a-c) and asymptotic solutions (d-f). 83
- Figure 4.6: The instantaneous (a-d) and time-averaged (e-h) velocity field around a “stiff” swimmer in the body-fixed frame when choosing $\sigma_b = 0.5$, $Pe = 1$, and $Er = 10$: (a,e) Newtonian; (b,f) Isotropic, $\zeta = 2$; (c,g) Nematic and parallel, $\zeta = 8$; (d,h) Nematic and perpendicular, $\zeta = 8$. The vector field and the background color correspond to the velocity \mathbf{u} and its magnitude $|\mathbf{u}|$ 85
- Figure 4.7: The time-averaged director and polymer force fields around a stiff swimmer corresponding to Figs. 4.6(f-h). (a-c): nematic director $\langle \mathbf{m} \rangle$ superposed on the colormap of the order parameter S . (d-f): polymer force vector $\langle \mathbf{f}_p \rangle$ superimposed on the force magnitude $|\langle \mathbf{f}_p \rangle|$ 86

DYNAMICS AND STRUCTURE OF AN APOLAR ACTIVE SUSPENSION IN AN ANNULUS

1.1 Abstract

We study the complex dynamics of a two-dimensional suspension comprising non-motile active particles confined in an annulus. A coarse-grained liquid crystal model is employed to describe the nematic structure evolution, and hydrodynamically couples with the Stokes equation to solve for the induced active flows in the annulus. For dilute suspensions, coherent structures are captured by varying particle activity and gap width, including unidirectional circulations, traveling waves, and chaotic flows. For concentrated suspensions, the internal collective are featured by motile disclination defects and flows at finite gap widths. In particular, we observe an intriguing quasi-steady state at certain gap widths during which $+1/2$ -order defects oscillate around equilibrium positions accompanying traveling-wave flows that switch circulating directions periodically. We perform linear stability analyses to reveal the underlying physical mechanisms of pattern formations during a concatenation of instabilities.

1.2 Introduction

Active matter is a class of far-away-from-equilibrium systems comprising self-driven particles ([3, 4, 5]). When they are immersed in a fluid, motile

microstructures exert forces upon the ambient liquid which itself acts as a coupling medium for generation of multiscale dynamics, which presents challenges in design, analysis, and control of novel active materials. To take advantage of the anomalous properties (e.g., large-scale induced motion, enhanced diffusion, and energy conversion), it is essential to guide active matter to perform useful mechanical work. One way of doing this is to tune the suspension concentration and the amount of chemical fuels ([6, 7, 8]). Alternatively, it is possible to make use of the particle interactions, either individually or collectively, with obstacles and geometric boundaries for more direct manipulation. By trapping active suspensions (such as Pusher swimmers and Quincke rollers) within straight and curved boundaries, experimental and numerical studies have revealed stable coherent structures and flow types ([9, 10, 11, 12, 13, 14, 15, 16, 17, 18]).

In this paper, we study the complex dynamics of a two-dimensional (2D) apolar active suspension confined in an annulus. The rod-like microparticles are non-motile but mobile, and only advected by fluid flow. In the meantime, they elongate through nearly symmetric stretching or growth to exert extensile dipolar stresses on the solvent, and interact with each other through hydrodynamic coupling and steric alignment torques, which we referred to as the “Extensor” particles ([19, 20]). Examples include bacterial cell division ([21]), microtubule (MT) bundles undergoing polarity sorting driven by molecular motors ([7]), and tripartite Au-Pt-Au nanomotors generating surface flows due to catalytic reactions ([22, 23]). In the previous works by [19] and [20], a macroscale liquid crystal model, i.e., “BQ”-tensor theory, has been

derived from a kinetic theory that describes Extensors' ensemble dynamics. Compared to the macro models for the motile suspensions ([24]) where the coupled evolution equations for the suspension concentration, polarity, and tensorial-order parameter need to be solved together, we have shown that the apolar BQ-tensor model naturally conserves the local concentration and the global particle numbers, and can be characterized by the evolution equation of the second-moment tensor only. Through theoretical analyses and numerical simulations for Extensor suspensions in both unbounded domains and confined in circular chambers, we have demonstrated that this active fluid model, while being apolar, inherits all the basic transitions and instabilities associated with motile suspensions, and exhibits a rich set of collective dynamics.

We examine both the dilute and concentrated Extensor suspensions confined in an annulus geometry. For the dilute cases, we identify emergent coherent structures that resemble those observed in “polar” active suspensions of Pusher particles ([25, 17]) by varying particle activity and annulus gap width. Linear stability analyses are performed to reveal the underlying physical mechanisms of a series of hydrodynamic instabilities starting from a near-isotropic state. At a finite concentration, we show that the internal collective dynamics can be effectively inhibited when confined in thin gaps; they rise when the gap width is large enough so that the bending instability can develop in the radial direction to generate active nematic flows. In particular, we capture an intriguing quasi-steady state at a finite gap width featured by oscillating $+1/2$ -order defects and traveling-wave flows that switch circulating directions periodically.

1.3 Mathematical model

We consider a collection of Extensors particles suspended in a Newtonian fluid. These active particles are non-motile but can elongate or stretch near symmetrically to produce extensional flows that effectively exert dipolar stresses upon the liquid. As shown by [19, 20], the ensemble dynamics of Extensor particles whose center-of-mass position locates at \mathbf{x} with an orientation \mathbf{p} ($|\mathbf{p}| = 1$) can be described by a probability distribution function $\Psi(\mathbf{x}, \mathbf{p}, t)$ through a Smoluchowski equation. The particles exert stresses Σ on the liquid to drive fluid motion which is governed by the (dimensionless) incompressible Stokes equation:

$$\nabla p - \Delta \mathbf{u} = \nabla \cdot \Sigma, \quad (1.1)$$

$$\nabla \cdot \mathbf{u} = 0, \quad (1.2)$$

where \mathbf{u} and p are the fluid velocity and pressure, respectively. The extra stress tensor Σ can be written as ([26, 27]):

$$\Sigma = \alpha \mathbf{D} + \beta \mathbf{S} : \mathbf{E} - 2\zeta\beta (\mathbf{D} \cdot \mathbf{D} - \mathbf{S} : \mathbf{D}) \quad (1.3)$$

where $\mathbf{E} = 1/2 (\nabla \mathbf{u} + \nabla \mathbf{u}^T)$ is the rate-of-strain tensor; $\mathbf{D} = \int_p \mathbf{p} \mathbf{p} \Psi d\mathbf{p}$ and $\mathbf{S} = \int_p \mathbf{p} \mathbf{p} \mathbf{p} \mathbf{p} \Psi d\mathbf{p}$ are the second- and fourth-moment tensors respectively, and are calculated by taking the average of \mathbf{p} on the surface of a unit sphere. In equation (1.3), the first term represents a dipolar extensile stress that arises from the local extensional flows with the dimensionless coefficient $\alpha < 0$ quantifying particle activity ([28, 26]). The second term is a constraining stress due to particle rigidity ([29, 30]) with an effective shape factor $\beta > 0$ characterizing particle's aspect ratio. The third term is due to steric

interactions through a Maier-Saupe potential with a strength coefficient ζ ([31, 30, 27]). Note that both the constraining and steric interaction stresses are proportional to the effective volume fraction of the suspension, and hence cannot be neglected for concentrated suspensions ([30, 27]).

The flow equation is coupled with the evolution equation of \mathbf{D} tensor, which is derived from the kinetic model by taking a standard moment average ([29, 19, 20]):

$$\mathbf{D}^\nabla + 2\mathbf{E} : \mathbf{S} = 4\zeta (\mathbf{D} \cdot \mathbf{D} - \mathbf{S} : \mathbf{D}) + d_T \Delta \mathbf{D} - 4d_R \left(\mathbf{D} - \frac{\mathbf{I}}{2} \right) \quad (1.4)$$

where $\mathbf{D}^\nabla = \frac{\partial \mathbf{D}}{\partial t} + \mathbf{u} \cdot \nabla \mathbf{D} - (\nabla \mathbf{u} \cdot \mathbf{D} + \mathbf{D} \cdot \nabla \mathbf{u}^T)$ is an upper-convected derivative, d_R and d_T are the rotational and translational diffusion coefficients, respectively. It is worthwhile to mention that in the classical Landau-de Gennes approach for liquid crystalline fluids ([32]), d_R and d_T are essentially the linear terms in a Landau potential and the Frank elastic constant for a nematic liquid crystal respectively. In nondimensionalization, we assume there are N Extensor particles of length l and width b ($b/l \ll 1$) distributed in a volume V , and introduce an effective volume fraction $\nu = nbl^2$ where $n = N/V$ is the mean number density ([30, 19, 20]). Then we choose the length scale $l_c = b/\nu$, the velocity scale $|u_0|$ which represents the surface velocity due to elongation or stretching motion, and the stress scale $\mu|u_0|/l_c$. Equation (2.2) can be closed by expressing the fourth-moment tensor \mathbf{S} in terms of \mathbf{D} through the so-called Bingham closure ([33, 34, 19]) which reconstructs a distribution function $\Psi_B(\mathbf{x}, \mathbf{p}, t)$ in terms of a traceless

symmetric tensor $\mathbf{T}(\mathbf{x}, t)$ to yield

$$\Psi_B[\mathbf{T}] = \frac{\exp(\mathbf{T} : \mathbf{p}\mathbf{p})}{\int_p \exp(\mathbf{T} : \mathbf{p}\mathbf{p}) d\mathbf{p}}. \quad (1.5)$$

We determine tensor \mathbf{T} numerically by solving the relation $\mathbf{D} = \int_p \Psi_B[\mathbf{T}] \mathbf{p}\mathbf{p} d\mathbf{p}$. Given \mathbf{T} , the fourth-moment tensor \mathbf{S} is then approximated by $\mathbf{S}_B = \int_p \Psi_B[\mathbf{T}] \mathbf{p}\mathbf{p}\mathbf{p}\mathbf{p} d\mathbf{p}$ as Ψ_B is determined by assuming \mathbf{S} and \mathbf{D} are co-aligned in \mathbf{D} 's principal coordinates. We refer to the above model as the BQ-tensor model ([19, 20]). In the following, we define the 2D tensor-order parameter $\mathbf{Q}(\mathbf{x}, t) = \mathbf{D}/\phi(\mathbf{x}, t) - \mathbf{I}/2$ (here $\phi(\mathbf{x}, t) = \int_p \Psi d\mathbf{p}$ is the concentration) whose maximal non-negative eigenvalue λ_{max} of \mathbf{Q} satisfying $0 \leq \lambda_{max} \leq 1/2$. We call its associated unit eigenvector the nematic director \mathbf{m} , and $0 \leq s = 2\lambda_{max} \leq 1$ the scalar order parameter.

1.4 Results and Discussion

When simulating the confined active fluid motion, we solve the \mathbf{D} dynamics equation (2.2) together with the incompressible Navier-Stokes equation at small Reynolds numbers ($\text{Re} = 10^{-3}$) using a mixed finite element method ([35, 36, 19]). At the inner ($r = R_1$) and outer ($r = R_2$) boundaries, a no-slip condition $\mathbf{u} = \mathbf{0}$ is imposed for the velocity field, and a no-flux condition $(\mathbf{n} \cdot \nabla)\mathbf{D} = \mathbf{0}$ is used for the second moment tensor \mathbf{D} . Note that in this way, we do not enforce any particular alignment direction at the boundary but guarantees the global particle number conservation. For all the simulation results below, we vary α and $R_{1,2}$, and fix $d_T = d_R = 0.025$ (for both dilute and concentrated suspensions), as well as $\zeta = 0.5, \beta = 0.874$ (for concentrated suspensions).

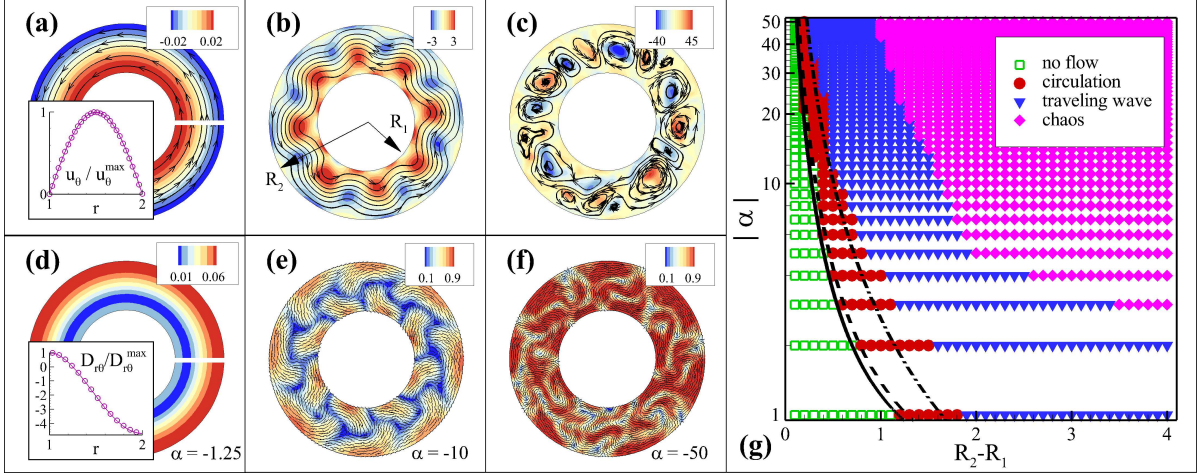


Figure 1.1: (a-c) Characteristic flow patterns (streamline overlaid on the colormap of vorticity Ω) and (d-f) nematic structures (nematic director \mathbf{m} field overlaid on the colormap of scalar order parameter s) when choosing $R_1 = 1.0$ and $R_2 = 2.0$. Insets in (a) and (d) are the comparisons between the analytical (solid lines) and numerical (open circles) results for normalized u_θ and $D_{r\theta}$ components taken along the white lines when $|\alpha|$ slightly goes beyond the critical value $|\alpha|_{cr} = 1.23$ for the Isotropy-Circulation instability. (g) Phase diagram of $(|\alpha|, R_2 - R_1)$ when fixing $R_1 = 1.0$. The solid and dashed lines characterize the Isotropy-Circulation instability in an annulus and a straight channel, respectively. The dash-dot line characterizes the Circulation-Traveling wave instability in a straight channel for sharply-aligned rods by neglecting the rotational diffusion.

1.4.1 Dilute Suspension

We first examine the cases of a confined dilute suspension by neglecting both the steric interaction stress ($\zeta = 0$) and the constraining stress ($\beta = 0$), and start simulations from an initially near-isotropic state. As shown in figure 2.1(a-f) where $R_1 = 1.0$ and $R_2 = 2.0$ are fixed, characteristic nematic structures and flow patterns are highlighted at different regimes of $|\alpha|$. As shown in panel(a), a unidirectional circulating flow first appears when $|\alpha|$ goes beyond a certain critical value α_{cr} (in this case $\alpha_{cr} = -1.23$). While the nematic order is still low as shown in panel(d), it clearly shows that particles

become aligned in the azimuthal direction due to fluid shear ([26, 37]), with a stronger alignment near rigid walls. As $|\alpha|$ further increases up to 10.0 in panel(b), a circulating flow pattern still dominates but the streamlines exhibit periodic bending deformations in the radial direction to form traveling waves, leading to counterclockwise (CCW) and clockwise (CW) vortices near the inner and outer boundaries, respectively. Such oscillatory patterns have also been seen in other active liquid crystal systems owing to the bending (or splay) deformations ([38, 39, 40]). In panel(e), the flow-induced alignment is further enhanced to form low-order structures (blue color). At even higher values of $|\alpha|$, the flow pattern in panel(c) becomes seemingly chaotic. The resultant nematic field exhibits a typical active liquid-crystalline phase ([7, 41, 42, 27, 5]) in which $\pm 1/2$ disclination defects stream around, and are constantly generated/annihilated during interactions (see panel(f)).

Note that while our model is apolar, the observed phenomena are very similar to those reported for polar active suspensions where effects of self-swimming motions of microparticles (e.g., bacterium) are taken into account ([43, 25, 17]). It is essential to recognize that the nonlinear dynamics is governed by a concatenation of hydrodynamic instabilities as α increases, and can be characterized by a series of instabilities including Isotropy to Circulation, Circulation to Traveling wave, and Traveling wave to Chaos. The overview of instabilities is highlighted in a phase diagram plotted in the $(|\alpha|, R_2 - R_1)$ plane in panel(g) where R_1 is fixed to be 1.0. Furthermore, the marginal stability curve that delineates the Isotropy-Circulation instability can be calculated analytically in the polar coordinates. To do this, we perturb the

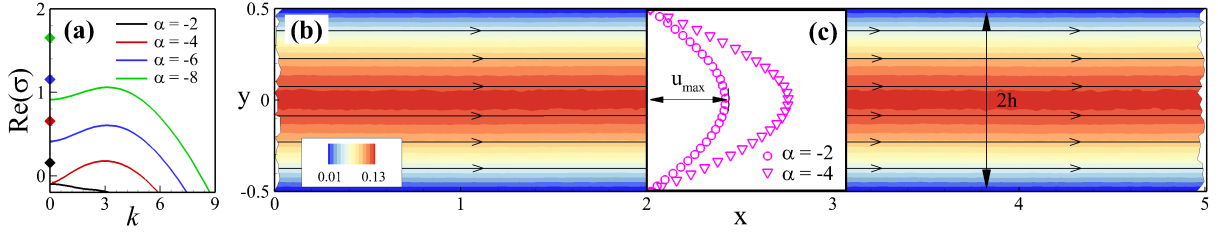


Figure 1.2: (a) Growth rate $\text{Re}(\sigma)$ for the long-wave (diamonds) and finite-wavelength (lines) instabilities as a function of wavenumber k for Isotropy-Circulation instabilities in a periodic straight channel when choosing $h = 0.5$, $d_T = d_R = 0.025$. (b) Streamlines overlaid on the colormap of u velocity component at $\alpha = -4.0$. (c) Velocity profiles at $\alpha = -2.0$ ($u_{\max} = 0.07$) and $\alpha = -4.0$ ($u_{\max} = 0.13$), respectively.

near-isotropic solutions as $\mathbf{D} = \mathbf{I}/2 + \epsilon \mathbf{D}'(r)$ and $\mathbf{u} = \epsilon \mathbf{u}'(r)$ ($\epsilon \ll 1$) by assuming azimuthal symmetry. Following the procedure by [9], we examine an initially exponential growth $\frac{\partial \mathbf{D}'}{\partial t} = \kappa \mathbf{D}'$ with the growing factor $\kappa \geq 0$. After some algebra, we find $D'_{rr} = D'_{\theta\theta} = 0$, and the hydrodynamic instability arises from the coupled linearized equations for u'_θ and $D'_{r\theta}$ below:

$$\frac{\partial u'_\theta}{\partial r} - \frac{u'_\theta}{r} + \alpha D'_{r\theta} = \frac{A_0}{2r^2}, \quad (1.6)$$

$$r^2 \frac{\partial^2 D'_{r\theta}}{\partial r^2} + r \frac{\partial D'_{r\theta}}{\partial r} + (\gamma r^2 - 4) D'_{r\theta} = -\frac{A_0}{4d_T}, \quad (1.7)$$

where $\gamma = -\frac{16d_R + 4\kappa + \alpha}{4d_T}$. We are able to seek the solutions $D'_{r\theta} = -\frac{A_0}{4\gamma d_T r^2} + A_1 \frac{\partial J_2(\sqrt{\gamma}r)}{\partial r} + A_2 \frac{\partial N_2(\sqrt{\gamma}r)}{\partial r}$ and $u'_\theta = -\frac{A_0}{2r} \left(1 + \frac{\alpha}{4\gamma d_T}\right) + \frac{2A_1}{\sqrt{\gamma}} J_1(\sqrt{\gamma}r) + \frac{2A_2}{\sqrt{\gamma}} N_1(\sqrt{\gamma}r) + A_3 r$, where J_j and N_j are respectively the Bessel functions of the first and the second kind, with coefficients A_j to be determined. By applying boundary conditions $\frac{\partial D'_{r\theta}}{\partial r} = 0$ and $u'_\theta = 0$ on the two walls, we then solve the eigenvalues of γ numerically at $\kappa = 0$ (solid line in panel(g)), as well as the velocity and \mathbf{D} field (insets in panels(a,d)), which, again, confirm our simulation results.

Next, we reveal the nature of hydrodynamic instabilities and gain physical

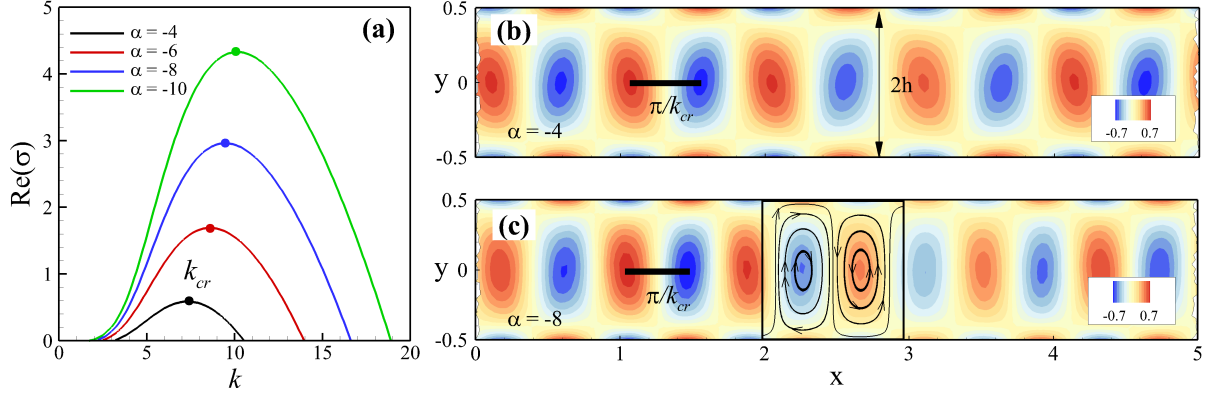


Figure 1.3: (a) Growth rate $\text{Re}(\sigma)$ as a function of wavenumber k for bending instabilities of the sharply-aligned Extensors when confined in a periodic straight channel when choosing $h = 0.5$, $d_R = 0$ and $d_T = 0.025$. The maximum growth rates at the critical wavenumbers k_{cr} are marked by solid circles. (b) and (c) show the vorticity field Ω as bending instability start to grow at $\alpha = -4.0$ and $\alpha = -8.0$, respectively. The solid black scales represent the length scales π/k_{cr} that match the separation distance between the neighboring vortices.

insights into formation of the observed coherent structures in figure 2.1. As shown below, while analytical approaches are feasible for the Isotropy-Circulation and Circulation-Traveling wave transitions, the Traveling wave-Chaos instability is highly nonlinear and hence can only be explored numerically. Here we avoid tedious mathematical manipulations in the polar coordinates to simplify our analysis by considering confinement in a straight periodic channel (i.e., in the limit $R_{1,2} \rightarrow \infty$) where very similar collective dynamics and hydrodynamic instabilities are observed ([17]). For the two cases considered, we employ a homogeneous base-state solution of \mathbf{D}_0 without background flow (i.e., $\mathbf{u}_0 = \mathbf{0}$, $p_0 = 0$), and introduce perturbations

$(\mathbf{D}', \mathbf{u}', p')$ to yield the following linearized equations:

$$\begin{aligned} \frac{\partial \mathbf{D}'}{\partial t} - (\nabla \mathbf{u}') \cdot \mathbf{D}_0 - \mathbf{D}_0 \cdot (\nabla \mathbf{u}'^T) + 2\mathbf{E}' : \mathbf{S}_0 \\ = d_T \nabla^2 \mathbf{D}' - 4d_R \mathbf{D}', \end{aligned} \quad (1.8)$$

$$\nabla p' - \Delta \mathbf{u}' = \nabla \cdot (\alpha \mathbf{D}'), \quad (1.9)$$

$$\nabla \cdot \mathbf{u}' = 0, \quad (1.10)$$

with boundary conditions $\frac{\partial \mathbf{D}'}{\partial y} = 0$ and $\mathbf{u}' = 0$ on the upper ($y = h$) and bottom ($y = -h$) walls. (Note here $D'_{11} + D'_{22} = 0$.) We then take Fourier transform in the x direction of all perturbed quantities \mathbf{f}' such that $\mathbf{f}'(x, y) = \tilde{\mathbf{f}}(k, y) \exp(ikx + \sigma t)$, where $\tilde{\mathbf{f}}$ is the amplitude function, k is the wavenumber, and σ is the complex-valued growth rate.

Case 1: Isotropy-Circulation Instability. In this case the instability grows from an initially isotropic state, i.e., $\mathbf{D}_0 = \mathbf{I}/2$. The linearized equations in (2.3) and (2.4) become

$$(\delta^{(2)} - k^2)^2 \tilde{v} + 2\alpha k^2 \delta \tilde{D}_{11} - ik\alpha (\delta^{(2)} + k^2) \tilde{D}_{12} = 0, \quad (1.11)$$

$$2d_T (\delta^{(2)} - \omega) \tilde{D}_{11} - \delta \tilde{v} = 0, \quad (1.12)$$

$$4d_T k (\delta^{(2)} - \omega) \tilde{D}_{12} + i (\delta^{(2)} + k^2) \tilde{v} = 0, \quad (1.13)$$

where $\delta^{(n)} = \frac{d^n}{dy^n}$ represents the n th derivative of y , and $\omega = \frac{\sigma + 4d_R}{d_T} + k^2$. We find that the general solution of the above equations has the vector form

$$\begin{aligned} (\tilde{D}_{11}, \tilde{D}_{12}, \tilde{v}) &= (B_1 \mathbf{F}_1 + B_2 \mathbf{F}_2) e^{ky} + (B_3 \mathbf{F}_3 + B_4 \mathbf{F}_4) e^{-ky} \\ &+ B_5 \mathbf{F}_5 e^{\sqrt{\omega}y} + B_6 \mathbf{F}_6 e^{-\sqrt{\omega}y} + B_7 \mathbf{F}_7 e^{i\sqrt{-\chi}y} + B_8 \mathbf{F}_8 e^{-i\sqrt{-\chi}y}, \end{aligned} \quad (1.14)$$

where $\chi = \omega + \frac{\alpha}{4d_T}$, and \mathbf{F}_j can be written as:

$$\begin{aligned}
\mathbf{F}_1 &= \{ik, k, 2id_T(k^2 - \omega)\}, \\
\mathbf{F}_2 &= \{ik^2y, k^2y, 2id_T[k(k^2 - \omega)y + k^2 + \omega]\}, \\
\mathbf{F}_3 &= \{-ik, k, 2id_T(k^2 - \omega)\}, \\
\mathbf{F}_4 &= \{-ik^2y, k^2y, 2id_T[k(k^2 - \omega)y - k^2 - \omega]\}, \\
\mathbf{F}_5 &= \{i(k^2 + \omega), 2\sqrt{\omega}k, 0\}, \\
\mathbf{F}_6 &= \{-i(k^2 + \omega), 2\sqrt{\omega}k, 0\}, \\
\mathbf{F}_7 &= \{2k\sqrt{-\chi}, -\chi - k^2, -i\alpha k\}, \\
\mathbf{F}_8 &= \{-2k\sqrt{-\chi}, -\chi - k^2, -i\alpha k\}.
\end{aligned}$$

By implementing the eight boundary conditions $\delta\tilde{D}_{11} = \delta\tilde{D}_{12} = \delta\tilde{v} = \tilde{v} = 0$ at $y = \pm h$, we obtain a linear system for B_j . The existence of non-trivial solutions gives ω and hence σ . On the other hand, we find that the long-wave solution has to be solved separately due to singularity at $k = 0$. By making use of the fact that the solution is unidirectional, we are able obtain the equilibrium solution: $(\tilde{D}_{11}, \tilde{D}_{12}, \tilde{v}) = (0, \sin\left(\sqrt{\frac{\alpha+4\sigma+16d_R}{4d_T}}y\right), \cos\left(\sqrt{\frac{\alpha+4\sigma+16d_R}{4d_T}}y\right))$, which yields the growth rate

$$\sigma = -\frac{\alpha}{4} - \left(\frac{\pi}{2h}\right)^2 d_T - 4d_R, \quad \text{at } k = 0. \quad (1.15)$$

As shown by the comparisons in figure 1.2(a), we find the real part of the growth rates of the long-wave modes (diamond symbols) are always larger than those of the corresponding finite-wavelength ones (solid lines), and hence dominate instability. Moreover, equation (1.15) suggests a marginal stability condition: $|\alpha| > 4\left(\frac{\pi}{2h}\right)^2 d_T + 16d_R$, which recovers the theoretical predictions for unbounded suspensions in the limit $h \rightarrow \infty$ ([27]). When making

connections to the annulus geometry by replacing the gap width $2h$ by $R_2 - R_1$, we find the marginal instability curve in figure 2.1(g) can be accurately fitted as a function of the form $K (R_2 - R_1)^{-2} d_T + 16d_R$ but with a different constant K due to curved geometries (in this case $K \approx 28.7$). It is apparent that the prediction in the straight periodic channel (dashed line in figure 2.1(g)) agrees well with that of the curved annulus, suggesting that equation (1.15) in fact provides a reasonable estimate of the time scale of the Isotropy-Circulation instability under a general parallel confinement.

Case 2: Circulation-Traveling wave Instability. It needs to keep in mind that the Circulation-Traveling wave instability is in fact a secondary instability developed from a shear-induced aligned state whose analytical form, however, is lacking. Nevertheless, we consider a reduced model where all the Extensor particles are initially aligned in the x direction, and neglect the rotational diffusion by choosing $d_R = 0$ ([19]). For such a “sharply-aligned” configuration, the homogeneous base-state solution is simply $\mathbf{D}_0 = \text{diag}\{1, 0\}$. After some algebra, we are able to eliminate several unknown variables, and show that the hydrodynamic instability is determined by the following six-order ODE for the off-diagonal component \tilde{D}_{12} :

$$\begin{aligned} & \delta^{(6)} \tilde{D}_{12} - k^2 \left(\frac{\sigma}{d_T k^2} + 3 \right) \delta^{(4)} \tilde{D}_{12} \\ & + k^4 \left(\frac{2\sigma - \alpha}{d_T k^2} + 3 \right) \delta^{(2)} \tilde{D}_{12} - k^6 \left(\frac{\sigma + \alpha}{d_T k^2} + 1 \right) \tilde{D}_{12} = 0 \end{aligned} \quad (1.16)$$

which admits the general solution $\tilde{D}_{12} = \sum_{j=1}^6 C_j \exp(\lambda_j y)$. The eigenvalues λ_j and hence the growth rate σ are then solved numerically by applying the converted boundary conditions $(\sigma + d_T k^2) \tilde{D}_{12} - d_T \delta^{(2)} \tilde{D}_{12} = 0$ and

$\delta\tilde{D}_{12} = \delta^{(3)}\tilde{D}_{12} = 0$ at $y = \pm h$, and seeking for non-trivial solutions. The real part of the growth rates as a function of k are plotted in figure 1.3(a) at different values of α , showing the maximum growth rates occurring at finite critical wavenumbers $k_{cr} > 0$. In panels(b,c), we set up the corresponding numerical simulations with the same initial conditions, and highlight the snapshots of the vorticity field $\Omega = \frac{\partial u}{\partial y} - \frac{\partial v}{\partial x}$. The simulations results show the generation of fluid jets that are perpendicular to the particle alignment direction due to the nematic bending instability, which leads to uniformly spaced vortices of alternating signs. The separation distance between the neighboring vortex pair can be accurately measured by the characteristic length scale π/k_{cr} .

While the above analysis is for a reduced model by assuming particle alignment in the x direction without background flow, it reveals the finite-wavelength nature of the bending instability, and provides quantitative measurements for the intrinsic time and length scales selected by the parallel confinement. Similar to Case 1, the predicted Circulation-Traveling wave borderline (dash-dot line in panel(g)) in the straight channel indeed agrees with the simulation results of the annulus geometry, especially in the regime of high $|\alpha|$ and small $R_2 - R_1$ where particles are strongly aligned and hence close to the sharp alignment approximation. Beyond the traveling-wave regime, the transition towards chaotic flows is highly non-linear, and can only be determined by numerical simulations.

1.4.2 Concentrated Suspension

In this section we examine the nonlinear dynamics of concentrated suspensions where both β and ζ are non-zero. A mean-field torque is introduced to govern the rotational dynamics of Extensor particles in the kinetic model through a Maier-Saupe steric potential ([31]). As shown by [27, 44, 19], for rod-like particles, the resultant enhanced steric interactions spontaneously drive the systems away from an initially isotropic state to form a nematic-like state when $\zeta > 4d_R$.

Compared to the dilute cases where isotropy is the only admissible equilibrium state, we have obtained the steady-state solutions of \mathbf{D} without flows at relatively small values of $|\alpha|$, which exhibit much more complicated nematic configurations as shown in figure 1.4. For passive particles when choosing $\alpha = 0$, figure 1.4(a) reveals that the system quickly relaxes to a homogeneous nematic state where the equilibrium solution satisfies a 2D distribution of Bingham form ([27, 19, 20])

$$\Psi_B(\phi) = \frac{\exp [\delta (\xi) \cos (2\phi)]}{\int_0^{2\pi} d\phi' \exp [\delta (\xi) \cos (2\phi')]} \quad (1.17)$$

where ϕ is the rod's orientation angle, and δ is a function of coefficient $\xi = 2\zeta/d_R$. Therefore, the degree of alignment is in fact determined by the ratio between ζ and d_R . As α increases, it is seen that the nematic field lines in figure 1.4(b) become distorted to spiral outwards to the annulus boundaries, reminiscent of the defect structures of active nematics when confined in a circular disk ([9, 19]). As $|\alpha|$ approximately goes beyond 0.5, the nematic structures in figure 1.4(c,d) switch to become azimuthal-symmetric and independent of the values of α , which can be solved analytically by setting the

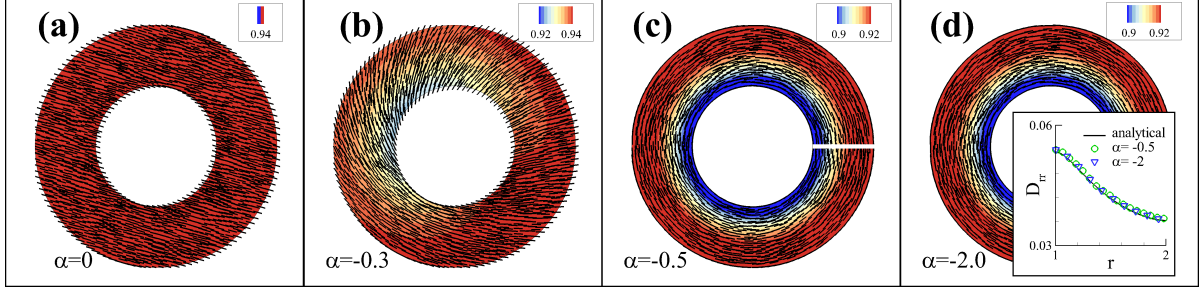


Figure 1.4: Equilibrium solutions of nematically-aligned states at different values of α when choosing $R_1 = 1.0$ and $R_2 = 2.0$, nematic director field overlaid on the colormap of s . Inset in panel(d): Comparisons between the analytical (solid line) and numerical (open symbols) results at $\alpha = -0.5, -2.0$ for D_{rr} component. The numerical data are taken along the white line marked in panel(c).

right-hand-side of equation (1.5) to be zero, and then seeking for the steady-state solution of \mathbf{D} as a function of r only. The observed variations in the equilibrium nematic states can be illustrated by examining the system's transient dynamics that evolves from near-isotropy. One interesting example is shown in figure 1.5 when choosing $\alpha = -2.0$. An Isotropy-Circulation instability first occurs in figure 1.5(a) to reorient particles, due to the combined effect of the circulating flow and the Maier-Saupe steric interactions. However, in this case the confinement effect in the thin gap is so strong that it suppresses the bending deformation occurring in the radial direction. As a result, the induced circulating flow gradually diminishes, and the system eventually relaxes to an axisymmetric equilibrium state where all particles are approximately aligned in the azimuthal direction; see insets in figure 1.5(b-d).

Increasing gap width relaxes the confinement effect to facilitate the active flow generation through bending instability, which can be similarly explained by the analysis in the dilute cases above. As shown in figure 1.6, system's

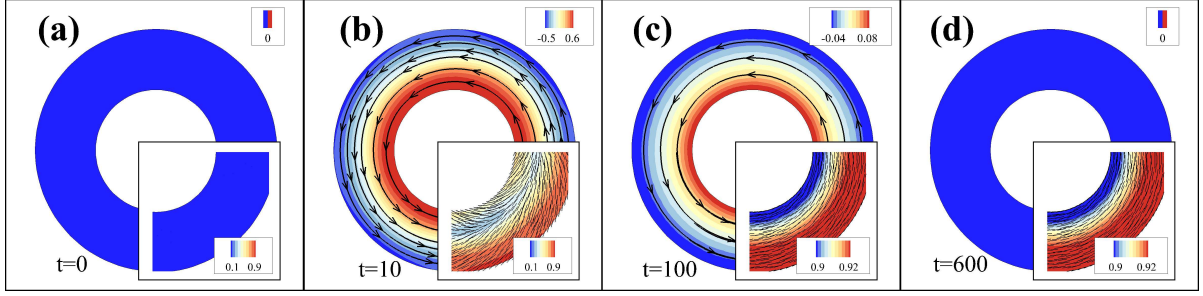


Figure 1.5: Evolution of the flow patterns for a concentrated Extensor suspension when choosing $\alpha = -2.0$, $R_1 = 1.0$ and $R_2 = 2.0$. Insets: nematic director field overlaid on the colormap of s .

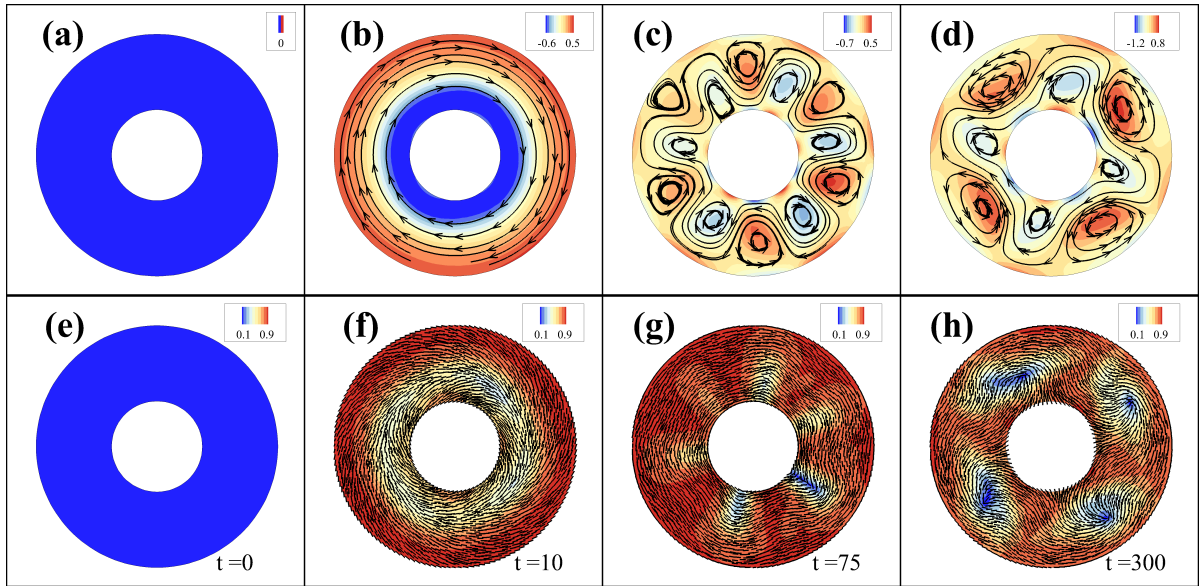


Figure 1.6: Flow patterns (streamline overlaid on the colormap of Ω , upper row) and nematic structures (nematic director field overlaid on the colormap of s , lower row) that characterize the long-time dynamics of a confined Extensor suspension when choosing $\alpha = -2.0$, $R_1 = 0.75$ and $R_2 = 2.0$.

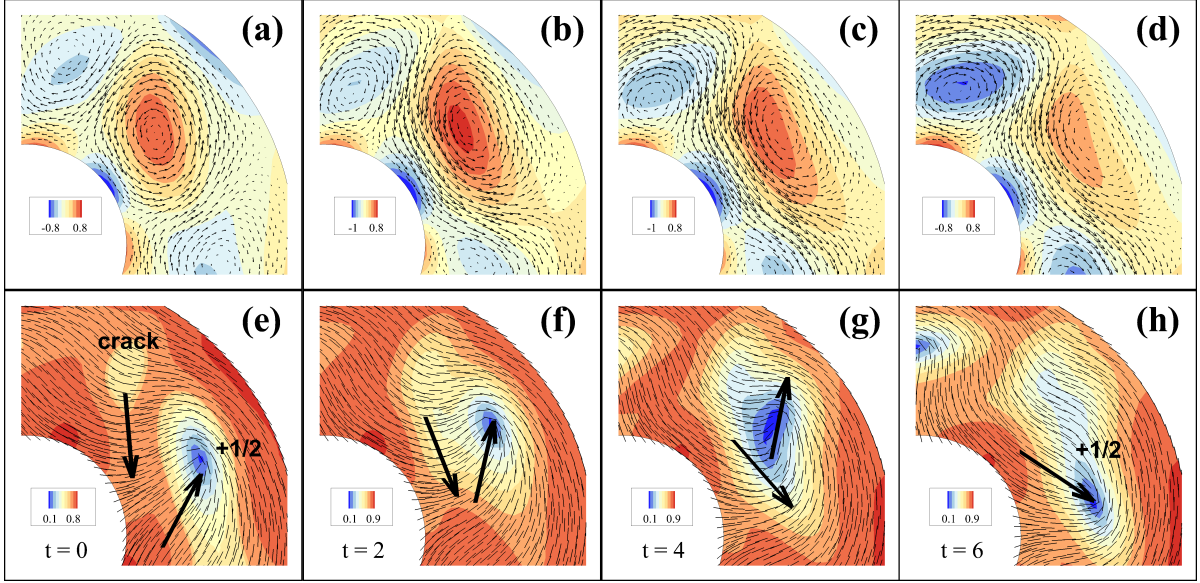


Figure 1.7: Short-time evolution of the flow (velocity vector overlaid the colormap of on Ω , upper row) and nematic (nematic director overlaid on the colormap of s , lower row) fields for the case shown in figure 1.6. In (e-h), the black arrows shows the direction of the crack formation and $+1/2$ defect movement.

long-time dynamics clearly exhibits an Isotropy-Circulation (panels(b,f)) and then a Circulation-Traveling wave (panels(c,g)) instability. Compared to the stable structures observed in the dilute cases, structure formation and evolution in concentrated suspensions are much more complicated. In panel(c), it is shown that active flows bend the streamlines to form traveling waves, leading to six evenly-spaced “incipient cracks” growing from the inner wall into the bulk regime shown in panel(g). Disclination defects of charge $\pm 1/2$ are seen to be born along these cracks, move around, and undergo nucleation/annihilation when interacting with each other as well as with rigid boundaries. Interestingly, the system gradually approaches a quasi steady-state where four $+1/2$ defects oscillate around their equilibrium positions; see panel(h). The flow field remains to be traveling-wave like but also periodically

switches directions; see panel(d). The reader is referred to the supplementary movie S1 for the entire history of the complex dynamics.

As shown in figure 1.7, a close look at the short-time dynamics of oscillating $+1/2$ defects and the accompanying swirling flow reveals the subtle interplay among the nematic structure variation, the active flow generation, as well as their interactions with the curved walls. The swirling flow drives the upward movement of the $+1/2$ disclination defect, and in the mean time, induces an opposite bending deformation nearby to form an incipient crack. As shown in panels(f,g), the crack “head” keeps moving downward to become a $+1/2$ defect (see panel(h)); while its “tail” gradually merges with the up-moving $+1/2$ defect before it hits the wall. Corresponding to the nematic structure change, the resultant CCW (CW) vorticity is seen to be strengthened (weakened) when the crack and defect interact, and then weakened (strengthened) during their annihilation. We find such an oscillating state is very robust when choosing R_1 less than 1.5, and the gap width $R_2 - R_1$ between 1.0 and 1.5 (also see movie S2 for the similar dynamics observed in a smaller annulus). As shown in movie S3, more complex defect dynamics and seemingly chaotic flows dominate when $R_2 - R_1 > 2.0$, resembling the active nematic flows observed in an unbounded domain ([19, 27]).

1.5 Conclusion

In this work we have studied the nonlinear dynamics and flow patterns of apolar Extensor suspensions confined in an annulus geometry through modeling and simulation. The BQ-tensor model with the Bingham closure,

which was coarse-grained from a mesoscale kinetic model, is used to describe the evolution of the second-moment \mathbf{D} tensor ([19]). The \mathbf{D} dynamics equation is coupled with the incompressible Navier-Stokes equation which are solved by using a Galerkin mixed element method at low Reynolds numbers. We have observed active flow generation and spontaneous coherent structures in both dilute and concentrated suspensions. We have gained physical insights of the analytical structure, hydrodynamic instabilities, and characteristic time and length scales under parallel confinement by performing stability analyses for dilute suspensions in a periodic straight channel. In particular, we have shown analytically the long-wave and finite-wavelength nature of the Isotropy-Circulation and Circulation-Traveling wave instabilities, respectively. By using similar models and analyses, we will be able to explore more challenging situations when active fluids are confined in complex geometries at high dimensions.

TRANSPORT OF AN APOLAR ACTIVE SUSPENSION IN A RECTANGULAR CHANNEL

2.1 Abstract

We study fluid and mass transport in a dilute apolar active suspension confined in a rectangular channel. We adopt a coarse-grained active liquid crystal model to describe collective unstable dynamics of non-motile but mobile rod-like particles, i.e., the “Extensors”, in Stokes flows. By using a Galerkin mixed finite element method, we are able to reveal various patterns of spontaneous coherent flows that can be unidirectional, traveling-wave, and chaotic. Comparing with our previous work by [1], we extend our analysis in weak flows to strong flow regimes by solving steady unidirectional flows of finite strengths analytically, and then perform more rigorous analyses to precisely capture the marginal stability curve of the unidirectional flow to traveling-wave instability. More interestingly, we find that the concatenation of instabilities may produce unique high-order unstable modes selected by geometric confinement, which can also be used to predict all the different kinds of instabilities shown in the phase diagram. In addition, we study transport of a circular cylinder in active flows, and have identified intriguing trajectories by varying the cylinder size, channel width, and Extensor particle activity. The weakening effects of active flow are observed when a large cylinder blocks the channel or when multiple cylinders are transported at a

high volume fraction.

2.2 Introduction

Manipulating small volumes of fluids is critical in a wide range of biological and engineering processes such as mixing, separation, targeted drug delivery, and micropumps. In a microfluidic environment that is typically within sub-millimeter, accomplishing these functions requires us to implement efficient fluid actuation methods via external controls from pressure or electric/magnetic/optical fields, in order to overcome fluid resistance. Recent advances of active matter, a novel class of non-equilibrium systems comprising self-driven constituents that consume a local fuel (e.g., chemical fuel) to generate particle motions or induce flows ([3, 4]), can potentially serve as new “engines” for precisely manipulating fluid in engineering applications.

In “wet” active matter systems, suspended motile microparticles effectively exert stresses upon the ambient liquid, which itself acts as a coupling medium for complex collective dynamics with ordering transition, fluctuating density and force/stress generation. Examples include biological swimmers such as bacteria and microalgae ([45]), synthetic colloidal surfers actuated by chemical reactions ([46]), as well as purified biopolymers (e.g., microtubules (MTs)) mixed with molecular motors (e.g. kinesin) [7, 27]. More interestingly, in concentrated active suspensions, the enhanced particle interactions may lead to a myriad of dynamic states such as active crystalline phases that are featured by spontaneous coherent structures such as streaming topological defects and coherent flows ([18]).

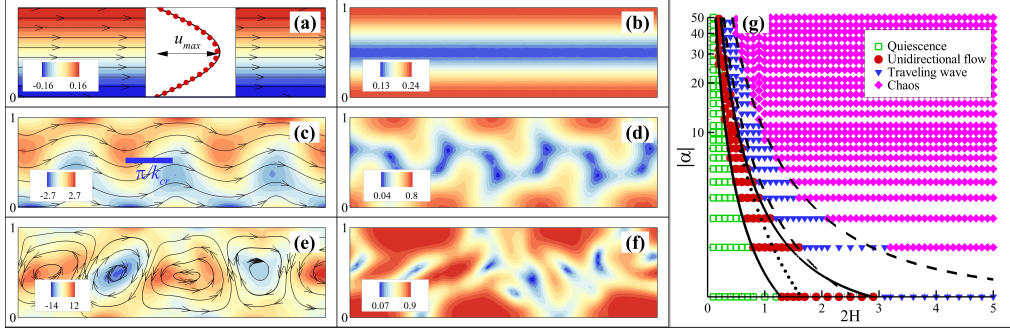


Figure 2.1: Typical (quasi-)steady coherent flows (a,c,e) and nematic orders (b,d,f) for unidirectional flow (a,b), traveling wave (c,d), and chaos (e,f). Simulations are performed when choosing the half channel width $H = 0.5$, $d_R = d_T = 0.025$, and $\alpha = -2.0, -8.0, -20.0$. Comparison of simulation and analytical solutions of the velocity profile is shown in inset of (a) where the maximum velocity is $u_{max} = 0.57$. (g) Phase diagram of $(|\alpha|, 2H)$. The solid line are the marginal stability curves from the analyses of the Q-U and U-T instabilities. The dashed lines are the predictions using the geometrically-selected high-order modes. The dotted line is our previous prediction when using a sharp-alignment assumption ([1]).

As we glean a higher level understanding of active matter, it is intriguing to exploit their anomalous physical properties for doing useful mechanical work. Indeed, recently several microfluidic experiments have shown that active matter, when appropriately guided by boundaries, can be used to pump/mix fluids ([12, 25]), transport cargos ([47]), and power microgears ([48]). These intriguing experimental observations have given rise to new, as yet unanswered questions: How will microparticle propulsion and local interactions change the near-wall dynamics, and hence bulk coherent flows? Will active flows selectively deliver cargos of particular sizes and shapes? To a large extent, the fundamental understandings of how collective dynamics interact with the complex microfluidic environment will shed light upon novel fluid and mass transport mechanisms promised by active matter.

Here we study the transport mechanisms of a dilute active suspension confined by two parallel plates. We employ a reduced model for non-motile but mobile rod-like particles that are only advected by fluid flow. These particles elongate or stretch to exert extensile dipolar stresses on the solvent, and interact with each other through hydrodynamic coupling and steric alignment torques, which is referred to as the “Extensors”. As shown by [19], from a mesoscale kinetic model, we are able to derive a macroscale active liquid crystal model, i.e., “ BQ ”-tensor theory, to describe Extensors’ ensemble dynamics by solving the evolution equation of the second moment tensor. Using this model, we have successfully revealed unstable collective dynamics and pattern formation of Extensor suspensions confined in an annulus geometry ([1]).

Compared with our previous work ([1]) where analyses were performed under some ad-hoc assumptions (e.g., being isotropic or sharply-aligned) in weak flow regimes, here we make analytical efforts in strong active flows by solving the analytical solutions of unidirectional flows with finite strengths. Therefore, we are able to capture the unidirectional flow to traveling wave instability accurately. More interestingly, we show that besides the leading-order modes that characterize the main flow features, the existence of the geometrically-selected high-order modes at the current flow regime provides accurate predictions of the flow transition at the next level. Next, we investigate transport behaviors of circular cylinders in apolar active flows, and find that their dynamics, when either fixed or free-moving, can be analytically solved in the weak flow regime. Furthermore, we perform numerical

simulations in strong flow regimes to capture intriguing trajectories in traveling wave flows for cylinders of different sizes, as well as weakened active flows for transport of a large cylinder or multiple cylinders at a high volume fraction.

2.3 Mathematical model

Here we briefly describe the mathematical model for the ensemble dynamics of a collection of Extensor particles suspended in a Newtonian fluid. More details can be found in our previous publications ([19, 20, 1]). In this model, we assume rod-like particles are non-motile but mobile. They exert dipolar stresses upon the ambient liquid through nearly symmetric elongation or stretching. The resultant active fluid is governed by the following (dimensionless) incompressible Stokes equation driven by an extra particle stress:

$$\nabla \cdot \mathbf{u} = 0, \quad \nabla p - \Delta \mathbf{u} = \nabla \cdot (\alpha \mathbf{D}) \quad (2.1)$$

where \mathbf{u} and p are the fluid velocity and pressure, respectively. For dilute suspensions, the evolution equation of \mathbf{D} tensor follows the evolution equation:

$$\frac{\partial \mathbf{D}}{\partial t} + \mathbf{u} \cdot \nabla \mathbf{D} - (\nabla \mathbf{u}) \cdot \mathbf{D} - \mathbf{D} \cdot (\nabla \mathbf{u})^T + 2\mathbf{E} : \mathbf{S} - d_T \Delta \mathbf{D} + 4d_R \left(\mathbf{D} - \frac{\mathbf{I}}{2} \right) = \mathbf{0}, \quad (2.2)$$

where $\mathbf{E} = 1/2 (\nabla \mathbf{u} + \nabla \mathbf{u}^T)$ is the rate-of-strain tensor, d_R and d_T are the rotational and translational diffusion coefficients, respectively. The right-hand-side of equation (2.1) is attributed to a dipolar active stress $\alpha \mathbf{D}$ whose strength coefficient α ($\alpha < 0$) characterizes activity of microswimmer. Here

\mathbf{D} and \mathbf{S} are the second- and fourth-rank symmetric tensors respectively, which are the corresponding second- and fourth-order orientation moments in terms of the particle orientation vector \mathbf{p} ($|\mathbf{p}| = 1$), and can be defined by taking the average of \mathbf{p} on the surface of a unit sphere via a probability distribution function $\Psi(\mathbf{x}, \mathbf{p}, t)$ such that $\mathbf{D} = \int_p \mathbf{p}\mathbf{p}\Psi d\mathbf{p}$ and $\mathbf{S} = \int_p \mathbf{p}\mathbf{p}\mathbf{p}\mathbf{p}\Psi d\mathbf{p}$ ([29]). The model is referred to as the *BQ*-tensor model ([19, 1]) since a 2D tensor-order parameter is defined as $\mathbf{Q}(\mathbf{x}, t) = \mathbf{D} - \mathbf{I}/2$ with its maximal non-negative eigenvalue $0 \leq \lambda_{max} \leq 1/2$. We call its associated unit eigenvector the nematic director \mathbf{m} , and $0 \leq s = 2\lambda_{max} \leq 1$ the scalar order parameter.

In nondimensionalization, we assume that there are N Extensor particles of length l and width b ($b/l \ll 1$) distributed in a volume V , and hence introduce an effective volume fraction $\nu = nl^3$ where $n = N/V$ is the mean number density ([49]). Then we choose the length scale $l_c = (nl^2)^{-1}$, the velocity scale $|u_0|$ which represents the surface velocity due to elongation or stretching motion, and the stress scale $\mu|u_0|/l_c$. Equation (2.2) can be closed by expressing the fourth-moment tensor \mathbf{S} in terms of \mathbf{D} through the so-called Bingham closure ([33, 19]).

In numerical simulation, we solve the \mathbf{D} dynamics equation (2.2) together with the incompressible Navier-Stokes equation at small Reynolds numbers (10^{-3}) using a mixed finite element method ([19, 1]). For all the simulation results below, we fix $d_T = d_R = 0.025$. To resolve the confined geometries as well as stationary and moving obstacles, a no-flux condition $(\mathbf{n} \cdot \nabla)\mathbf{D} = \mathbf{0}$ is used for the second moment tensor \mathbf{D} on geometric boundaries. To solve the velocity field, we imposed a no-slip condition ($\mathbf{u} = \mathbf{0}$) on the top and bottom

walls, i.e., $y = \pm H$. The freely-moving cargo, whose center-of-mass position is denoted by \mathbf{x}_c , follows a rigid-body motion such that $\mathbf{u} = \mathbf{U} + \boldsymbol{\Omega} \times (\mathbf{x} - \mathbf{x}_c)$ is imposed on the surface, where \mathbf{U} and $\boldsymbol{\omega}$ are respectively the translational and rotational speed, and are determined by the force and torque free conditions. An Arbitrary Lagrangian-Eulerian finite element method with a moving-mesh technique is used to simulate obstacle motions in confined active flows ([36, 35]).

2.4 Analysis and simulation results

2.4.1 Spontaneous Coherent Flows

Generally speaking, the unstable dynamics of confined active flows are determined by a delicate competition between the (destabilizing) active nematic force due to aligned structures against the (stabilizing) viscous force and topological constraints of channel walls. As $|\alpha|$ goes beyond a certain critical value, the system deviates from an initially isotropic state to form spontaneous coherent flows as the pattern changes from unidirectional flows to traveling waves, and eventually turns into chaos.

As shown in Figure 2.1, we have captured three transitions, namely quiescence to unidirectional flow (Q-U), unidirectional flow to traveling wave (U-T), and traveling wave to chaos (T-C), by systematically varying $|\alpha|$ and channel width. As shown in panel(a), in the weak flow regimes of small $|\alpha|$, when fixing the channel width, an Q-U instability first occurs, during which randomly-oriented microparticles become more aligned, accompanying development of a unidirectional flow with an approximately parabolic velocity

profile. As $|\alpha|$ increases, as shown in panel (b), the fluid velocity field gradually loses symmetry as the streamlines bend in the transverse direction to form rotating vortices, yielding wavy patterns with a clear separation of high and lower order zones. Further increasing $|\alpha|$ eventually leads to chaotic flows and motile defects. The constrained collective dynamics resemble those of Extensor particles trapped in a annulus, or Pusher particles in race-track geometries ([25, 17, 1]).

2.4.2 Concatenation of Hydrodynamic Instabilities

Next, we go beyond the analyses of weak flows ([1]) to investigate concatenation of hydrodynamic instabilities that occur in both weak and strong flow regimes, aiming to obtain a thorough physical understanding of the observed flow transitions in the phase diagram in figure 2.1(g). We first derive the analytical solutions of steady-state unidirectional flows with finite strengths. To begin with, we linearize the governing equations (2.1)-(2.2) by introducing the base-state (denoted by subscript “0”) and disturbance solutions (denoted by superscript “,”) such that $\mathbf{D} = \mathbf{D}^0 + \epsilon \mathbf{D}'$ and $\mathbf{u} = \mathbf{u}^0 + \epsilon \mathbf{u}'$ ($\epsilon \ll 1$), which lead to the following coupled equations:

$$\begin{aligned} \frac{\partial \mathbf{D}'}{\partial t} + \mathbf{u}^0 \cdot \nabla \mathbf{D}' + \mathbf{u}' \cdot \nabla \mathbf{D}^0 - \nabla \mathbf{u}^0 \cdot \mathbf{D}' - \mathbf{D}' \cdot \nabla (\mathbf{u}^0)^T \\ - \nabla \mathbf{u}' \cdot \mathbf{D}^0 - \mathbf{D}^0 \cdot \nabla \mathbf{u}'^T \\ + 2\mathbf{E}^0 : \mathbf{S}' + 2\mathbf{E}' : \mathbf{S}^0 = d_T \Delta \mathbf{D}' - 4d_R \mathbf{D}', \end{aligned} \quad (2.3)$$

$$\nabla \cdot \mathbf{u}' = 0, \quad \nabla p' - \Delta \mathbf{u}' = \nabla \cdot (\alpha \mathbf{D}'), \quad (2.4)$$

with no-flux and no-slip boundary conditions imposed on the top and bottom plates. We then take Fourier transform in x -direction of all disturbance

quantities \mathbf{f}' such that $\mathbf{f}'(x, y) = \tilde{\mathbf{f}}(k, y) \exp(ikx + \sigma t)$, where $\tilde{\mathbf{f}}$ is the amplitude, k is the wavenumber, and σ is the complex-valued growth rate.

Quiescence-Unidirectional Flow Instability. Consider initially rods are randomly oriented, corresponding to an isotropic state without flows. The base-state solutions are simply $\mathbf{D}^0 = \mathbf{I}/2$ and $\mathbf{u}^0 = \mathbf{0}$ (hence $\mathbf{E}^0 = \mathbf{0}$). From an microscopic perspective, this state can be described by a constant distribution function $\Psi_0 = 1/2\pi$ which yield the fourth-order moment $S_{ijkl}^0 = \frac{1}{8}(\delta_{ij}\delta_{kl} + \delta_{ik}\delta_{jl} + \delta_{il}\delta_{jk})$. As shown in our previous work by [1], the system first undergoes an Q-U instability. Due to the singularity at $k = 0$, we solved the long-wavelength mode separately to obtain the growth rate $\text{Re}(\sigma) = -\frac{\alpha}{4} - \left(\frac{\pi}{2H}\right)^2 d_T - 4d_R$ (here Re denotes the real part).

We were also able to derive analytically both the long-wavelength disturbance solution $u' = \Phi_0 H \cos\left(\frac{\pi}{2H}y\right)$, $v' = D'_{11} = -D'_{22} = 0$ and $D'_{12} = \frac{\Phi_0 \pi}{2\alpha} \sin\left(\frac{\pi}{2H}y\right)$ (Φ_0 is a unknown coefficient), as well as the other unstable modes which can be represented by a linear combination of eight vector polynomials in Fourier space (see details in [1]). As shown in figure 2.2(a), these high-order unstable modes grow more slowly and are of finite-wavelength with the maximum growth rate occurring at $k > 0$.

Unidirectional Flow-Traveling Wave Instability. As $|\alpha|$ further increases, the enhanced unidirectional flows will realign Extensor microparticles in the flow direction. As we have previously proven ([27, 1]), extensile rod-rod interactions with a nematically-aligned configuration are hydrodynamically unstable, and will drive a shear-induced secondary instability that grows perpendicular to the alignment direction to bend streamlines in the transverse

directions and create traveling-wave patterns, leading to counterclockwise (CCW) and clockwise (CW) vortices near the walls.

In the strong flow regime, while the exact unidirectional steady-state solutions are unfeasible, analytical manipulation is still possible if good approximations can be made for the rods of aligned configurations. To do this, we expand Ψ near isotropy such that $\Psi = \Psi^0 + \Psi' = A_0 + \mathbf{A}_1 : (\epsilon \mathbf{D}')$ where the two constants $A_0 = 1/2\pi$ and $\mathbf{A}_1 = \frac{2}{\pi}(\mathbf{p}\mathbf{p} - \frac{\mathbf{I}}{2})$ can be determined by comparing with the zeroth (i.e., concentration $\phi = \int_p \Psi d\mathbf{p}$) and the second-order moment \mathbf{D} ([20]). At the leading order, the fourth-moment tensor \mathbf{S} is then calculated as

$$S_{ijkl}^0 = \int_p p_i p_j p_k p_l \Psi_0 dp = -\frac{1}{24} (\delta_{ij} \delta_{kl} + \delta_{ik} \delta_{jl} + \delta_{il} \delta_{jk}) + \frac{1}{6} (\delta_{ij} D_{kl} + \delta_{ik} D_{jl} + \delta_{il} D_{jk} + \delta_{jk} D_{il} + \delta_{jl} D_{ik} + \delta_{kl} D_{ij}).$$

After substituting \mathbf{S}_0 into equation (2.2) and eliminating x -dependency, we can simplify the governing equations at steady state as

$$\delta^{(2)} D_{11}^0 = 4 \frac{d_R}{d_T} \left(D_{11}^0 - \frac{1}{2} \right) + \frac{\alpha}{d_T} (D_{12}^0)^2, \quad (2.5)$$

$$\delta^{(2)} D_{12}^0 = \left(\frac{16d_R + 3\alpha}{4d_T} - \frac{\alpha}{d_T} D_{11}^0 \right) D_{12}^0, \quad (2.6)$$

$$\delta^{(1)} u^0 = -\alpha D_{12}^0, \quad (2.7)$$

where $\delta^{(n)} = \frac{d^n}{dy^n}$ represents the n th derivative of y . As suggested by the analytical disturbance solutions, we find it is reasonable to assume the nematic field solutions to be of trigonometric form $D_{11}^0 = 1 - D_{22}^0 = B_0 + B_1 \cos(\frac{\pi}{H}y)$ and $D_{12}^0 = -B_2 \sin(\frac{\pi}{2H}y)$, with the unknown coefficients B_i . Then we can solve the velocity components as $u^0 = -\frac{2H\alpha B_2}{\pi} \cos(\frac{\pi}{2H}y)$ and $v^0 = 0$. By using the expressions of \mathbf{D}^0 and \mathbf{u}^0

and applying boundary conditions at the two walls, we are able to obtain B_i analytically after some algebra as $B_0 = \frac{1}{2} + \frac{\gamma_1\gamma_2}{\alpha\gamma_3}$, $B_1 = -\frac{d_R\gamma_2}{\alpha\gamma_3}$, and $B_2 = \sqrt{-\frac{8d_R\gamma_1\gamma_2}{\alpha^2\gamma_3}}$, where $\gamma_1 = \frac{\pi^2}{4H^2}d_T + d_R$, $\gamma_2 = \frac{\pi^2}{H^2}d_T + \alpha + 16d_R$, and $\gamma_3 = \frac{\pi^2}{H^2}d_T + 6d_R$ (hence $B_1 \ll B_0$). As shown in the inset of figure 2.1(a) for the velocity profile, this solution agrees well with the simulation results. In addition, it can be easily verified that setting $\gamma_2 = 0$ recovers the isotropic solution, and yields the marginal stability curve of the Q-U instability in the phase diagram.

Substituting the base-state solutions into (2.3) and (2.4) yields the linearized equations in Fourier space as:

$$\begin{aligned} & \left(d_T \delta^{(2)} - \omega + \frac{2iHk\alpha C_2}{\pi} \cos\left(\frac{\pi}{2H}y\right) \right) \tilde{D}_{11} + \frac{\alpha C_2}{2H} \sin\left(\frac{\pi}{2H}y\right) \tilde{D}_{12} \\ & + \left(ikC_2 \sin\left(\frac{\pi}{2H}y\right) + \frac{\pi C_1}{H} \sin\left(\frac{\pi}{H}y\right) \right) \tilde{v} \\ & - \left(\frac{1}{2}\delta^{(1)} + \frac{i}{k}C_2 \sin\left(\frac{\pi}{2H}y\right)\delta^{(2)} \right) \tilde{v} = 0, \end{aligned} \quad (2.8)$$

$$\begin{aligned} & \left(d_T \delta^{(2)} - \omega + \frac{2iHk\alpha C_2}{\pi} \cos\left(\frac{\pi}{2H}y\right) \right) \tilde{D}_{12} - \frac{\alpha C_2}{2H} \sin\left(\frac{\pi}{2H}y\right) \tilde{D}_{11} \\ & + \left(\frac{\pi}{2H}C_2 \cos\left(\frac{\pi}{2H}y\right) + ik\left(C_1 \cos\left(\frac{\pi}{H}y\right) + C_0 - \frac{1}{4}\right) \right) \\ & - \left(\frac{i}{k}\left(C_1 \cos\left(\frac{\pi}{H}y\right) + C_0 - \frac{3}{4}\right)\delta^{(2)} \right) \tilde{v} = 0, \end{aligned} \quad (2.9)$$

$$\left(\delta^{(4)} - 2k^2\delta^{(2)} + k^4 \right) \tilde{v} = -2k^2\alpha\delta^{(1)}\tilde{D}_{11} + (\alpha k i \delta^{(2)} + \alpha k^3 i)\tilde{D}_{12}, \quad (2.10)$$

where $\omega = \sigma + 4d_R + d_T k^2$. By sweeping values of α and H , we numerically solve the eigenvalue problem to obtain the growth rate σ for non-trivial solutions. The $\text{Re}(\sigma) - k$ curves in figure 2.2(b) show that the U-T instability is dominated by unstable modes of a finite wavelength whose maximum growth rate occurs at a critical wavenumber $k_{cr} > 0$. Also as shown in figure 2.1(b), the predicted characteristic length π/k_{cr} (solid blue line) agrees with

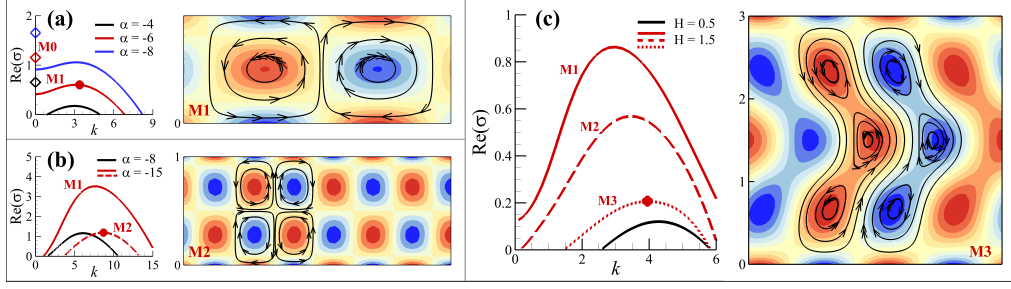


Figure 2.2: Unstable modes and growth rates $\text{Re}(\sigma)$ of linear stability analyses for Q-U (a), U-T (b), and T-C (c) instabilities. In (a,b), the channel width is chosen as $H = 0.5$; in (c), $\alpha = -4.0$ is fixed. The open diamond symbols (in panel(a) at $k = 0$) represent the long-wavelength (M0) mode associated with the unidirectional flow solution. The solid, dashed, and dotted lines in (a-c) represent the 1st (M1), 2nd (M2), and 3rd (M3) unstable modes, corresponding to the single, double, and triple vortex arrays, respectively. The colorfields for vorticity and streamlines exhibit flow patterns, and are selected at the critical wavenumbers (circular red dots).

the separation distance between the neighboring CW and CCW vortices from simulation results. Comparing to our previous results of “sharply-aligned” rods by assuming perfect alignment and neglecting the rotational diffusion ([1]), the newly predicted U-T transition agrees much better with the numerical results.

Geometrically-Selected Unstable Modes. A thorough understanding of the phase diagram in figure 2.1 requires uncovering the transition mechanisms of the T-C instability. Nevertheless, directly performing stability analysis is unfeasible due to the lack of analytical traveling-wave solutions at the base state. Besides the leading-order modes, we find that the selection and development of high-order modes in different flow transitions not only reflect the effects of geometrical confinement but also are “concatenated” in the sense the emergent high-order modes captured in each instability can be used to

predict the next-level flow transition.

We start from the lowest level Q-U transition with a leading-order unidirectional solution (denoted by M0 mode) as shown in figure 2.1(a). Stability analyses show that when H ($|\alpha|$) is fixed, the unstable modes associated with finite-wavelength instability as predicted in figure 2.2(a) only occur when $|\alpha|$ (H) goes beyond a certain critical value. Interestingly, we also find these finite-wavelength modes coexist with M0, and are all appear to be wavy. The corresponding vorticity maps show one vortex array in the channel center (denoted as M1), reminiscent of the traveling wave solutions. When comparing our results with the phase diagram, we find that examining the high-order modes of the disturbance solution yields a critical curve (black dashed line) of (α_{cr}, k_{cr}) that agree well with the previous determined marginal stability curve of U-T transition.

To further verify our conjecture, we explore the T-C transition by examining the high-order modes captured in the U-T analysis in figure 2.2 (b,c). As an example shown in Figure 2.2(b), we fix $H = 0.5$ and examine unstable modes by systematically increasing $|\alpha|$. As $3.5 < |\alpha| < 10$, the stability analyses yield only one branch of solution, corresponding to the leading-order traveling wave solutions (black solid line, M1 mode). When $|\alpha|$ goes beyond 10, the eigenvalue search picks another branch of solutions (marked by dashed line) that represents the high-order modes featured by double vortex arrays (denoted by M2). Likewise, as shown in panel(c), when fixing $\alpha = -4$ and increasing H from 0.45 (i.e., U-T transition) to approximately 1.5, more complex patterns are captured. Especially in a wide channel, double (M2) and even triple vortex

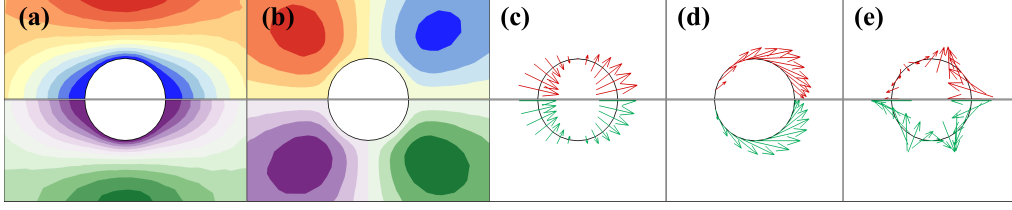


Figure 2.3: Active flow past a fixed cylinder of $R = 0.1$ in the channel center: rescaled (a) u and (b) v velocity component, and the surface distribution of (c) pressure force, (d) viscous force, and (e) active force. In (a)-(e), the upper row are the simulation results when choosing $\alpha = -2.0$, and the bottom row shows the normalized analytical results.

arrays (denoted by M3) exhibit, which suggests that the chaotic motions are in fact resultant from nonlinear interactions between multiple unstable modes with different length and time scales. The transition occurs at $H_{cr} \approx 0.9$. When sweeping values of α and H , the obtained critical curve that characterizes the mode switch from M1 to M2 and M3 indeed agree with the borderline for the T-C transition on the phase diagram.

2.4.3 Active Transport of Circular Cylinders

Next, we study how macro obstacles transport in the spontaneous coherent flows in the rectangular channel, which will be determined by the resultant hydrodynamic and nematic forces. To facilitate analytical manipulation and analysis, we consider the case of circular cylinder with possibly the simplest geometry.

Fixed Cylinder. We first consider the case of a circular cylinder fixed in the channel center. As shown by [19], it is convenient to introduce a 2D stream function $\varphi(x, y)$ to represent the disturbance velocity field as $\mathbf{u}' = (u', v') = (\partial\varphi/\partial y, -\partial\varphi/\partial x)$. Substituting $\varphi(x, y)$ into the governing

equations and assuming isotropy, we can derive a reduced linearized equation for φ as: $\frac{\partial \Delta^2 \varphi}{\partial t} + \left(\frac{\alpha}{4} + 4d_R\right) \Delta^2 \varphi - d_T \Delta^3 \varphi = 0$. We then replace the bi-harmonic operator using a scalar function such that $\Delta^2 \varphi = \psi$, leading to a steady-state equation of an elliptic form:

$$\left(\Delta - \left(\frac{\alpha + 16d_R}{4d_T} \right) \right) \psi = 0, \quad (2.11)$$

which will be solved in the half domain $x \geq 0$, $-H \leq y \leq H$, and on the cylinder surface $x^2 + y^2 = R^2$ with R the cylinder radius.

We first seek the general solution of ψ , and then solve an inhomogeneous Poisson equation to obtain the scalar stream function φ . After some algebraic manipulations, we have found that the solution can be written as:

$$\begin{aligned} \frac{\varphi(\hat{x}, \hat{y})}{H} = & \frac{2C_0}{\pi} \sin\left(\frac{\pi}{2}\hat{y}\right) \\ + \text{Re} \left(\sum_{n=1}^N \left\{ \begin{aligned} & C_n \begin{pmatrix} \cosh \xi_n \sinh \xi_n \hat{y} \\ -\hat{y} \sinh \xi_n \cosh \xi_n \hat{y} \end{pmatrix} e^{i\xi_n \hat{x}} \\ & + D_n \begin{pmatrix} \sinh \eta_n \cosh \eta_n \hat{y} \\ -\hat{y} \cosh \eta_n \sinh \eta_n \hat{y} \end{pmatrix} e^{i\eta_n \hat{x}} \end{aligned} \right\} \right), \end{aligned} \quad (2.12)$$

where $\hat{x} = x/H$ and $\hat{y} = y/H$, and C_n and D_n are unknown coefficients. In the above, the first part is attributed to the long-wavelength weak flow solution of the Q-U instability without cylinder. The second part satisfies the no-slip condition on the top and bottom walls by using an expansion of Papkovitch-Fadle (PF) eigenfunctions ([50]). The corresponding eigenvalues ξ_n and η_n ($n = 1, 2, 3, \dots$) are the complex roots of the equations: $\xi - \sinh \xi \cosh \xi = 0$ and $\eta + \sinh \eta \cosh \eta = 0$, with positive real and imaginary parts. The roots are ordered as $0 < \text{Im}\xi_1 < \text{Im}\xi_2 \dots$ and

$0 < \text{Im}\eta_1 < \text{Im}\eta_2 \dots$ where “Im” denotes the imaginary part. Applying the no-slip condition on the cylinder surface enable us to solve for C_n and D_n ($n > 0$) in terms of C_0 . The solution of φ (and hence \mathbf{u}') at $x < 0$ can be obtained by using the symmetry condition $\varphi(\hat{x}, \hat{y}) = \varphi(-\hat{x}, \hat{y})$. Next, we solve for the disturbance nematic field \mathbf{D}' through an elliptic equation:

$$d_T \Delta \mathbf{D}' - 4d_R \mathbf{D}' = -\frac{1}{4} \left(\nabla \mathbf{u}' + (\nabla \mathbf{u}')^T \right), \quad (2.13)$$

which yields the solution for \mathbf{D}

$$= \text{Re} \left(\sum_{n=1}^N \left\{ \begin{array}{l} E_n \begin{pmatrix} \sinh \eta_n \cosh \eta_n \hat{y} \\ -\hat{y} \cosh \eta_n \sinh \eta_n \hat{y} \end{pmatrix} e^{i\eta_n \hat{x}} \\ + F_n \begin{pmatrix} \cosh \xi_n \sinh \xi_n \hat{y} \\ -\hat{y} \sinh \xi_n \cosh \xi_n \hat{y} \end{pmatrix} e^{i\xi_n \hat{x}} \end{array} \right\} \right), \quad (2.14)$$

$$+ \text{Re} \left(\sum_{n=1}^N \left\{ \begin{array}{l} G_n \begin{pmatrix} \cosh \xi_n \sinh \xi_n \hat{y} \\ -\hat{y} \sinh \xi_n \cosh \xi_n \hat{y} \end{pmatrix} e^{i\xi_n \hat{x}} \\ + H_n \begin{pmatrix} \sinh \eta_n \cosh \eta_n \hat{y} \\ -\hat{y} \cosh \eta_n \sinh \eta_n \hat{y} \end{pmatrix} e^{i\eta_n \hat{x}} \end{array} \right\} \right). \quad (2.15)$$

with the unknown coefficients (E_n, F_n, G_n, H_n) being solved by applying the no-flux condition on the cylinder surface. In the end, \mathbf{D}' at $x < 0$ is obtained by observing that $D'_{11}(-\hat{x}, \hat{y}) = -D'_{11}(\hat{x}, \hat{y})$ and $D'_{12}(\hat{x}, \hat{y}) = D'_{12}(-\hat{x}, \hat{y})$.

In figure 2.3 we exhibit the steady-state flow (from left to right) fields and surface force distributions, and compare the results obtained by using FEM and the weak-flow analysis. In general, it is observed that the simulation

results are in good agreement with the analytical predictions. Not surprisingly, the flow field in panels(a,b) resembles the classical case of an incoming flow past a cylinder. To highlight the near surface dynamics, we break the traction exerted on the cylinder surface into the contributions from pressure field (panel(c), $\mathbf{f}_p = -p\mathbf{n}$), viscous force (panel(d), $\mathbf{f}_v = \left(\nabla \mathbf{u} + (\nabla \mathbf{u})^T \right) \cdot \mathbf{n}$), and active (nematic) force (panel(e), $\mathbf{f}_a = \alpha (\mathbf{D} - \mathbf{I}/2) \cdot \mathbf{n}$), respectively. Performing surface integration of traction yields a net rightward force exerted on the cylinder, which is largely attributed to the pressure and viscous forces due to their fore-aft asymmetry. The net nematic force is approximately zero due to the near-symmetric structure as estimated by the weak-flow analysis, although the structure will become more asymmetric in a finite unidirectional flow which has to be resolved by numerical simulations.

Free-Moving Cylinder. When released in the active flow, the cylinder will be dragged into motion. As shown in figure 2.4(a), in the weak flow regime where $|\alpha|$ is small, it is seen that the cylinder initially accelerates to reach a maximum, and then relaxes to a steady-state migration speed. Such an initial pulsative behavior is due to the hyperbolic nature of equation (2.2), somewhat reminiscent of viscoelastic fluids of Maxwell type where similar start-up behaviors are observed due to the propagation of stress waves ([51]). Furthermore, linearity of the weak-flow governing equations (2.11) and (2.13) permits analytical manipulations to obtain the steady-state cylinder migration velocity U in x -direction by decomposing the total force into two parts as $F_x = UF_x^{(1)} + C_0F_x^{(2)}$. Here $F_x^{(1)}$ and $F_x^{(2)}$ respectively represents the net force exerted on a cylinder moving in a quiescent Stokes flow at a constant speed

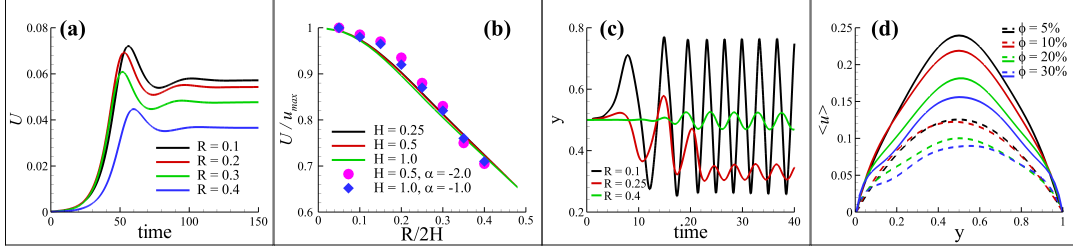


Figure 2.4: Transport of free-moving cylinders in active flows. (a) FEM results of typical time evolutions of the migration velocities for cylinders of different sizes when choosing $\alpha = -2.0$ and $H = 0.5$. (b) Solid lines represent the normalized steady-state migration velocities as functions of re-scaled radius. Symbols are the FEM results. (c) FEM results of cylinder trajectories ($R = 0.1$) in traveling wave flows. (d) FEM results of time-averaged velocity profiles at different cylinder volume fractions when choosing $R = 0.1$ and $H = 0.5$. The solid and dashed lines correspond to $\alpha = -4.0$ and -6.0 , respectively.

$U = 1$, and on a fixed cylinder by setting the unknown coefficient $C_0 = 1$. After calculating $F_x^{(1)}$ by following a similar solution procedure via PF eigenfunction expansion and substituting the previously computed results for the fixed cylinder when choosing the critical values $\alpha_{cr} = -\left(\frac{\pi}{H}\right)^2 d_T - 16d_R$ associated with the I-A instability, the migration velocity is then obtained by $U = -C_0 F_x^{(2)} / F_x^{(1)}$ for a free-moving cylinder (i.e., $F_x = 0$). In figure 2.4(b), we rescale the steady-state migration velocities by the maximum u -component of the unidirectional flow (u_{max}), and plot them in terms of the dimensionless radius that is re-scaled by the channel width $2H$. Not surprisingly, we have found that the all the analytical results computed at different channel widths collapse into one master curve, and, again, are in agreement with numerical simulation results.

In the strong flow regimes, the nonlinear dynamics of the free-moving cylinder need to be solved numerically. For cylinders whose size is much

smaller than the channel width, we expect that they will approximately follow the coherent flow patterns. As R increases, the cylinder motion may significantly impact topological structures of active flows, and hence may lead to rich dynamical behaviors. Indeed, as shown in figure 2.4(c) (also see movie S1) for three typical trajectories in traveling wave flows, a small cylinder oscillates periodically between the two parallel plates by following the wavy flow patterns. On the other hand, a finite-size cylinder, whose diameter is close to the half-wavelength of the traveling waves, seems to hardly catch the flow direction variations. Instead, the cylinder “sticks” to one plate such that it periodically hits and bounces off the boundary. Increasing the cylinder size may show some blockage effects to impede active flow development, and lead to a much slower migration velocity as more viscous damping force exerted on the cylinder. The blockage effect is further examined by studying transport behaviors of multiple cylinders in active flows. In figure 2.4 and movie S2, we show examples of the time-averaged velocity profiles of the resultant active at various cylinder volume fractions ϕ computed at $R = 0.1$ and $H = 0.5$, where significant flow damping occurs when ϕ goes beyond 10% whilst the mixture still shows active transport behavior at a even higher volume fraction (e.g., $\phi = 30\%$).

2.5 Conclusion

In this work we have combined theoretical analysis and numerical simulations in studying fluid and obstacle transport in a dilute 2D apolar active fluid confined in a rectangular channel by using the BQ -tensor model ([19]).

Compared to our previous work by [1], we have not only revealed the coherent structures in different parameter regimes but also, more importantly, precisely predicted the flow transitions that cover the entire phase diagram. To accomplish this goal, we first derived analytical solutions of steady unidirectional flows with finite strengths, which permit us to perform more rigorous stability analyses for the U-T instability without ad-hoc assumptions that were used by [1]. Moreover, by examining the existence of concatenated high-order wave modes from stability analyses at different levels, we were able to delineate the borderlines for both the U-T and T-C transitions. When a circular cylinder is placed in the apolar active fluid, we have been able to analytically solve for the flow fields and particle dynamics in the weak-flow regime for cylinders that is either fixed or free-moving. In strong coherent flows of traveling waves, we have observed intriguing trajectories for cylinders of different sizes. Suppression of active flow development has been observed when cylinder diameter is comparable of channel size, as well as when multiple cylinders are transported in active flows at a high volume fraction. We expect this study will shed light upon the new physics and novel transport phenomena of geometrically confined active fluids, which potentially suggest novel mechanisms of fluid manipulation in microfluidic devices.

SCALING LAW OF BROWNIAN ROTATION IN CONCENTRATED HARD-ROD SUSPENSIONS

3.1 Abstract

Self-diffusion in rod suspensions are subject to topological constraints because of steric interactions. This topological effect may be anisotropic when rods are nematically-aligned with their neighbors, and remains a challenge to existing theories. Via a classical Doi-Onsager kinetic model with the Maier-Saupe steric potential, we characterize the long-time rotational Brownian diffusivity D_r for dense suspensions of hard rods of finite aspect ratios, based on quadratic orientation auto-correlation functions. Furthermore, we show that the computed non-monotonic scalings of D_r as a function of volume fraction can be accurately predicted by a new *tube* model, which extends Doi and Edwards' semi-dilute theory from the isotropic phase to the nematic phase.

3.2 Introduction

Understanding diffusive transport behaviors of concentrated suspensions of rodlike microparticles (e.g., polymers, macromolecules, and colloids) in dense systems is of crucial importance in biology, physics, chemical engineering, and material sciences where the many-body interactions lead to intriguing pattern formation and material properties [52, 53, 54]. For example, the short-range steric interactions may dominate over hydrodynamic (or other

long-range interactions) at high volume fractions to drive isotropic-anisotropic order transition [32, 29, 55].

Various models have been developed to reveal the physical mechanisms of steric interactions in rod suspensions [56, 29, 55], where each rod may frequently collide with multiple neighbors. This challenges the theories of cluster-expansion type [57, 58], because of the fast-growing complexity of such expansion beyond the pairwise-level, i.e., beyond B_2 in virial expansion of free energy. Alternatively, one may construct mean-field type models by embedding one rod (a probe) into the environment of sterically interacting neighbors. The classical Doi and Edwards (DE hereafter) *tube* model [29] views such topologically-confined motion a certain “reptation” dynamics as the probe slithers among entangled rod meshwork [59, 29]. Because of the anisotropic shape of rods, the motion of this probe is confined within an imaginary *tube* formed by its neighbors, and typically exhibits restricted rotational motion (characterized by the diffusion coefficient D_r) within the *tube*. When estimating the small rotation angle of the probe before it disengages from the *tube*, DE’s model predicts $D_r/D_{r0} \sim (n\ell^3)^{-2}$ in the semi-dilute isotropic regime, where n is the rod number density, ℓ is the rod length, and D_{r0} is the rotational diffusivity of an isolated rod with no neighbors. It has been verified in several experiments and particle simulation studies [59, 60, 61, 62, 63, 64]. Nevertheless, we emphasize that most of the prior studies focus on the dilute or semi-dilute regime with D_r being extracted from the relaxation time of orientation auto-correlation functions (OACFs) which typically follows a simple exponential decay. However, the OACFs in

the nematic regime may exhibit much more complex behaviors due to phase transitions, which prevent them from being fitted into analytically trackable forms that permit clear definitions of the relaxation time scale(s). There is a general lack of accurate theoretical models for measuring D_r in the ordered phases (nematic or smectic) with strong steric confinement effect.

In this Letter, we characterize the long-time Brownian rotational diffusivity D_r for dense suspensions of rods with finite aspect ratios via a Doi-Onsager model where a Maier-Saupe (MS) potential is employed to capture the (I)sotropic-(N)ematic phase transition. When the hydrodynamic interactions are neglected, we show that the measured non-monotonic D_r can be explained by a modified DE's *tube* model, covering the entire range of volume fraction from dilute systems in the isotropic phase to dense networks in the nematic regime. By using a Geometric Constrained Brownian Dynamics (GCBD) algorithm [65], we build our theory based on extensive numerical simulation data of N Brownian spherocylinders, each with length ℓ , diameter b , and orientation \mathbf{p} , in a cubic domain of length L . This method verified the classic Brownian spherocylinders without hydrodynamic interactions investigated by [66] (see more details in Refs [65]). Our simulations cover a wide range of aspect ratio $\gamma = \ell/b$ and extend to volume fraction $\phi = \pi n \left(\frac{b^3}{6} + \frac{\ell b^2}{4} \right)$ over 50% (i.e., close to the Nematic-Smectic phase transition [66]), where $n = N/L^3$ is the particle number density. As shown by the open squares in Fig. 3.1, we perform ensemble average and calculate the (global) orientational order parameter $S = \frac{3}{2N} \sum_{i=1}^N (\mathbf{p}_i \cdot \hat{\mathbf{n}})^2 - \frac{1}{2}$ and $\hat{\mathbf{n}}$ the average orientation of spherocylinders (i.e., the director [32, 29]), which captures first-order I-N

transition as bifurcations of $S(\phi)$ curves.

3.3 Numerical method

The simulation method based on geometric constraints in this work was developed by [65]. The method is applicable for general smooth-shaped rigid bodies but we focus on spherocylinders in this work. We summarize it here briefly.

3.3.1 Complementarity formulation and equation of motion

In general, the velocity $\mathcal{U} = (U_1, \Omega_1, U_2, \Omega_2, \dots)$ of all spherocylinders in the system can be decomposed as the collision velocity \mathcal{U}_c and non-collisional velocity \mathcal{U}_{nc} :

$$\mathcal{U} = \mathcal{U}_{nc} + \mathcal{U}_c. \quad (3.1)$$

In this work the non-collisional motion refers to the translational and rotational Brownian motion.

The constraints are simply that the minimal separation distance $\Phi_\alpha(\mathcal{C})$ between each pair α of close rigid objects remain non-negative for all configurations \mathcal{C} . In total there are $n_c = O(N)$ close particle-particle pairs that may potentially collide. For each pair α , we denote the collision force magnitude between this pair of particles as γ_α . The pair $(\Phi_\alpha, \gamma_\alpha)$ must satisfy one of two conditions:

$$\text{No contact: } \Phi_\alpha > 0, \quad \gamma_\alpha = 0. \quad (3.2)$$

$$\text{In contact: } \Phi_\alpha = 0, \quad \gamma_\alpha > 0. \quad (3.3)$$

Mathematically, this yields a *complementarity problem*, written vertically over the set of pairs as:

$$0 \leq \Phi \perp \gamma \geq 0, \quad (3.4)$$

where $\Phi = (\Phi_0, \Phi_1, \dots) \in \mathbb{R}^{n_c}$ and $\gamma = (\gamma_0, \gamma_1, \dots) \in \mathbb{R}^{n_c}$ denote the collections of minimal distances and contact force magnitudes for each α .

For N rigid particles, let $D_\alpha \in \mathbb{R}^{6N}$ be a sparse column vector mapping the magnitude γ_α to the collision force (and torque) vector applied to each particle. We define a sparse matrix $\mathcal{D} \in \mathbb{R}^{6N \times n_c}$ as a collection of all D_α :

$$\mathcal{D} = [D_0 \ D_1 \ \dots \ D_{n_c}] \in \mathbb{R}^{6N \times n_c}, \quad \mathcal{F}_c = \mathcal{D}\gamma. \quad (3.5)$$

For each pair α , D_α defined in this way has 12 non-zero entries for non-spherical shapes, corresponding to 3 translational and 3 rotational degrees of freedom for each particle. For the special cases of two spheres, D_α has 6 non-zero entries, as normal collision forces induce no torques on spheres. The entries of each D_α are explicitly given in [67]. For rigid particles, there is an important relation between the transpose of \mathcal{D} and Φ :

$$\mathcal{D}^T = (\nabla_{\mathcal{C}} \Phi). \quad (3.6)$$

Euler angles.

Combining (3.4) and (3.5), we reach a differential variational inequality (DVI) for N particles and all constraints.

$$\dot{\mathcal{C}} = \mathcal{U}_{nc} + \mathcal{M}\mathcal{D}\gamma, \quad (3.7a)$$

$$0 \leq \Phi(\mathcal{C}) \perp \gamma \geq 0. \quad (3.7b)$$

Here \mathcal{U}_{nc} , \mathcal{M} , \mathcal{D} , and Φ depend only on the geometric configuration \mathcal{C} . This DVI is solvable and integrable over time once a relation between the configuration \mathcal{C} and the collision force γ is supplied, that is, a timestepping scheme. Higher order schemes such as the Runge-Kutta scheme can be used, but for simplicity of presentation we derive a first order Euler integration scheme here.

With given timestep Δt , (3.7) can be linearized as a Linear Complementarity Problem and then converted to a Constrained Quadratic Programming and be efficiently solved with gradient descent methods. Detailed derivation, discussion, and verification of our algorithm can be found in [65]. In this study, we simulate spherocylinders of length $\ell = 1\mu m$ and aspect ratio $5 \leq \gamma \leq 50$ for volume fractions $1\% \leq \phi \leq 50\%$, in cubic computation domain with the length varying between the maximum value $L = 10\ell$ (for $\gamma = 5$) and the minimum value $L = 4\ell$ (for $\gamma = 50$). The time step is chosen as $\Delta t = 1 \sim 5 \times 10^{-5}s$.

3.4 Results

3.4.1 Equilibrium PDF of the Doi-Onsager Model

A classical Doi-Onsager kinetic model [29] accurately describes the above mentioned critical behaviors via a time evolution equation

$$\frac{\partial \Psi}{\partial t} = D_r \mathcal{R} \cdot \left[\mathcal{R} \Psi + \frac{\Psi}{k_B T} \mathcal{R} U_s(\mathbf{p}) \right], \quad (3.8)$$

where Ψ is a probability distribution function (PDF) for rod's orientation (unit) vector \mathbf{p} , and $\mathcal{R} = \mathbf{p} \times (\partial/\partial \mathbf{p})$ is a rotational operator. In the above, D_r characterizes the long-time (or “collective”) Brownian rotational diffusion for

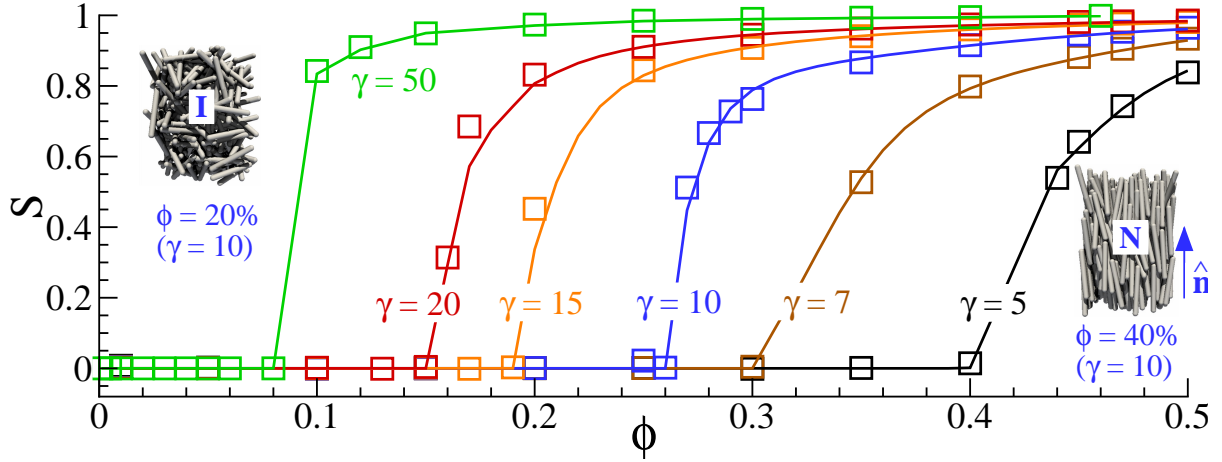


Figure 3.1: Equilibrium orientational order parameter S as a function of ϕ . The open squares represent the GCBD simulation data. The solid lines are calculated using Ψ_{eq} in Eq. (3.12). Inset: Instantaneous snapshots at $\phi = 20\%$ and 40% for $\gamma = 10$ correspond to the I and N phase, respectively.

an equilibrium rod system [29, 64]. A mean-field torque is imposed on the rod's rotational dynamics via the MS steric potential [31] $U_s(\mathbf{p}) = -\zeta_0 \mathbf{p} \mathbf{p} : \mathbf{Q}$ due to the crowdedness nature of densely packed rods, where $\mathbf{Q} = \langle \mathbf{p} \mathbf{p} - \mathbf{I}/3 \rangle$ is the nematic-order-parameter tensor with $\langle \rangle$ a configurational average of \mathbf{p} , and ζ_0 is a strength coefficient. At equilibrium (i.e., $\frac{\partial \Psi}{\partial t} = 0$), we rewrite the MS potential as $U_s^{(eq)} = -\zeta_0 \mathbf{p} \mathbf{p} : \mathbf{Q}_{eq}$ with $\mathbf{Q}_{eq} = S(\hat{\mathbf{n}} \hat{\mathbf{n}} - \mathbf{I}/3)$, and then balance the rotational diffusion and the steric torque to obtain the equilibrium PDF.

The rod system can be described by a probability distribution function $\Psi(\mathbf{p})$ as a function of the orientation vector \mathbf{p} , evolved through the Smoluchowski equation (1) in the main text. The equilibrium solution satisfies

$$\nabla_p \ln \Psi_{eq} = \frac{2\zeta_0}{k_B T} (\mathbf{I} - \mathbf{p} \mathbf{p}) \cdot \mathbf{Q} \cdot \mathbf{p} \quad (3.9)$$

In an isotropic state, $\Psi = \frac{1}{4\pi}$ with the coefficient $\zeta_0 = 0$. In the nematic regime, we assume the rods are distributed axisymmetrically around the

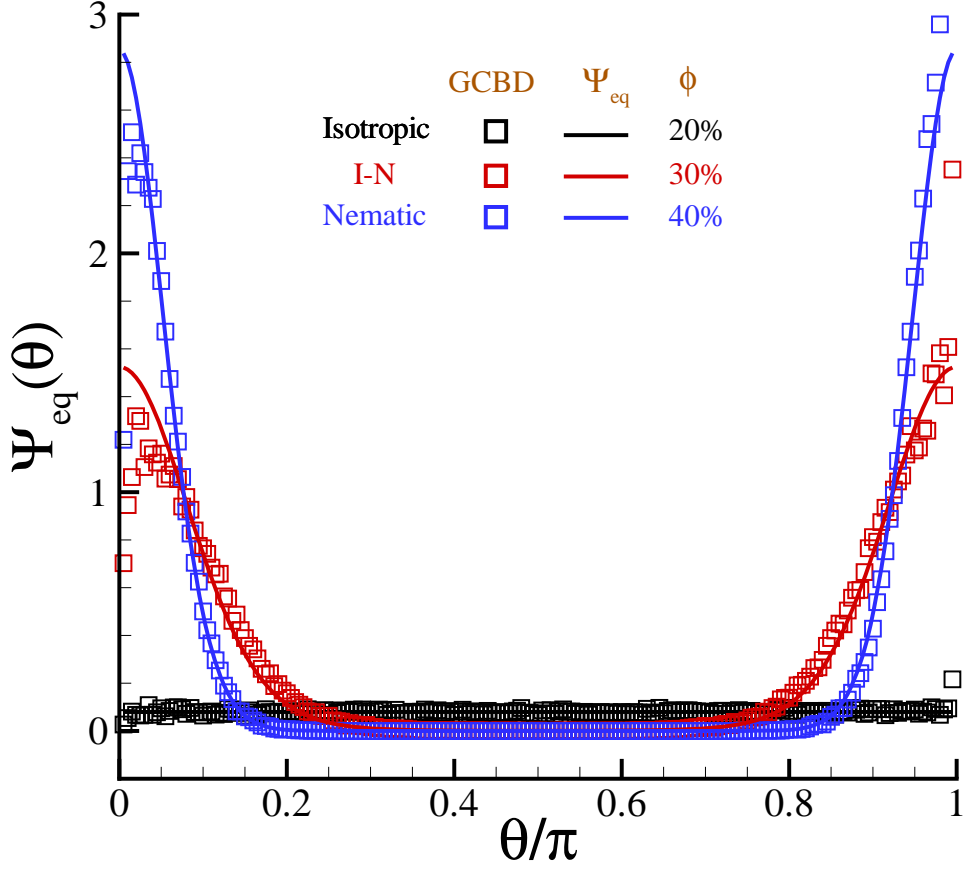


Figure 3.2: Examples of orientational PDF for $\gamma = 10$ at $\phi = 20\%$, 30% , 40% . Open squares represent the GCBD data, and the solid lines represent the results by using Ψ_{eq} in Eq.(2) in the main text.

director \hat{n} , yielding [30]

$$\mathbf{Q} = S \left(\hat{n}\hat{n} - \frac{\mathbf{I}}{3} \right), \quad (3.10)$$

where the order parameter S can be expressed as

$$S = \frac{1}{2} \int_0^{2\pi} \int_0^\pi \Psi (3 \cos^2 \theta - 1) \sin \theta d\theta d\phi. \quad (3.11)$$

By substituting (3.10) and (3.11) into (3.9), we can solve $\Psi(\theta)$ in spherical coordinates as

$$\Psi_{eq}(\theta) = \frac{\exp(\chi \cos(2\theta))}{2\pi \int_0^\pi \exp(\chi \cos(2\theta')) \sin \theta' d\theta'}, \quad (3.12)$$

with the coefficient $\chi = \frac{S\zeta_0}{2k_B T}$. For a given ϕ and γ , χ can be measured through the following steps: (1) take log on both sides of (3.12), yielding

$\log \Psi_{eq} = \chi \cos(2\theta) + \text{const}$; (2) construct a discrete orientation probability distribution from particle simulation by dividing θ uniformly into small intervals $\Delta\theta = \pi/400$; (3) take log on the discrete orientation probability distribution and convert it to be a function of $\cos(2\theta)$ and use the linear fitting to get χ . After χ is measured, a continuous PDF can be constructed based on (3.12). As examples shown in Fig. 3.2 for $\gamma = 10$ cases, the reconstructed PDF Ψ_{eq} accurately represent the numerical data.

3.4.2 Measuring D_r from quadratic OACFs

We examine the orientation relaxation process of a free probe in an equilibrium particle bath. As examples of $\gamma = 20$ shown in Fig. 3.3(a), direct measurements of long-time $\langle \mathbf{p}(t) \cdot \mathbf{p}(0) \rangle$ often show over-complicated evolution behaviors as the system deviates from the isotropic cases (e.g., $\phi = 10\%$) whose OACFs decay exponentially to zero [29]. During the I-N transition (e.g., $\phi = 17\%$ and 20%), however, the functions may exhibit extraordinary slow decays after the initial transient [68]. As an alternative approach shown in Fig. 3.3(b), when measuring the quadratic form $\langle (\mathbf{p}(t) \cdot \mathbf{p}(0))^2 \rangle$ (or equivalently $\langle P_2(\mathbf{p}(t) \cdot \mathbf{p}(0)) \rangle$, P_2 represents the *Legendre* polynomial of order 2 [69, 29, 63]), we observe that for all cases, the OACFs approach constant values after the initial decay, which can be accurately fitted into a universal form

$$\langle (\mathbf{p}(t) \cdot \mathbf{p}(0))^2 \rangle = (1 - A_\infty) \exp\left(-\frac{t}{\tau_R}\right) + A_\infty \quad (3.13)$$

with a (single) correlation time τ_R and a steady-state value A_∞ . In the isotropic regime ($\phi < 15\%$), $A_\infty = 1/3$ which has been proven analytically [29]; while

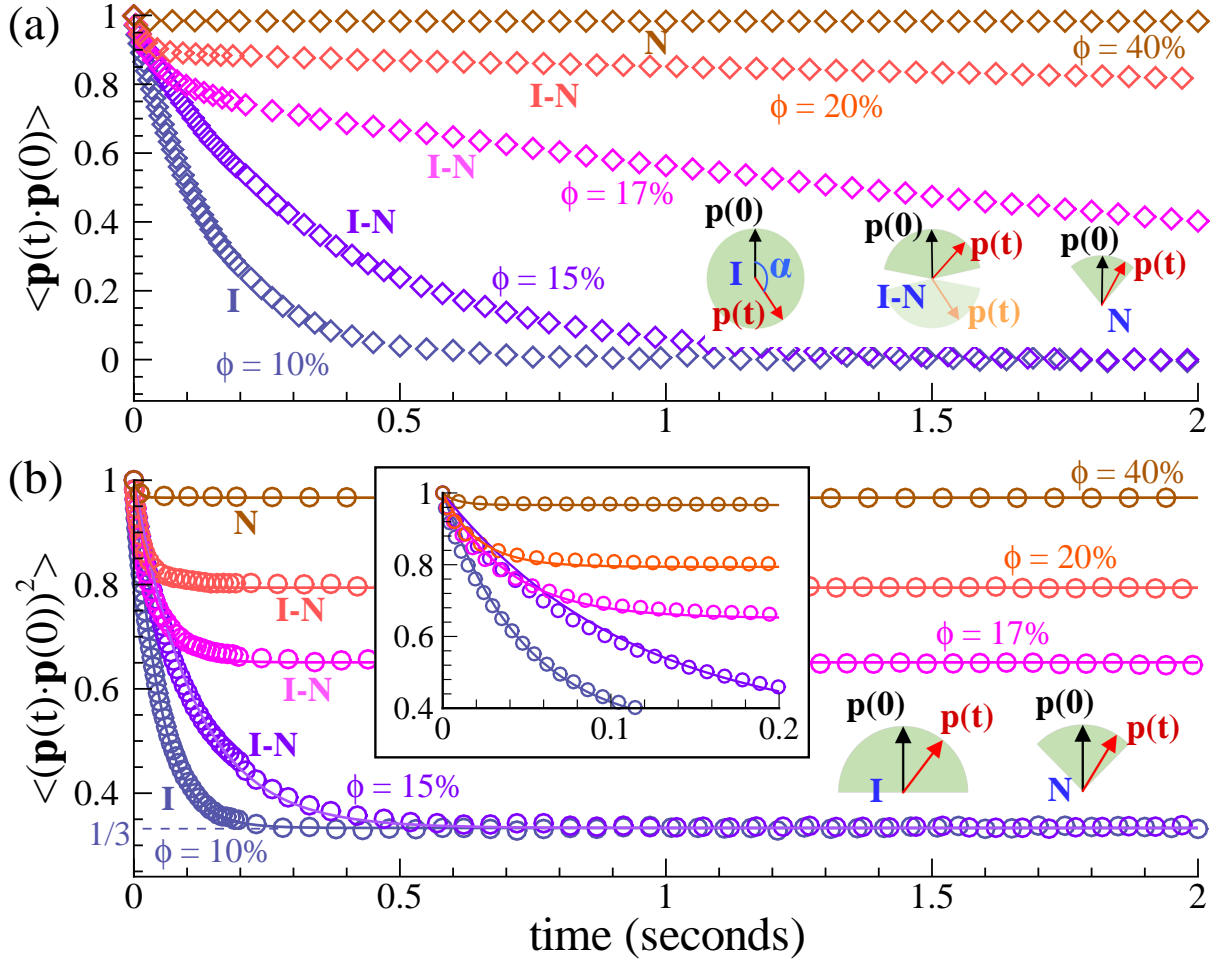


Figure 3.3: Orientation relaxation characterized by $\langle \mathbf{p}(t) \cdot \mathbf{p}(0) \rangle$ (a) and $\langle (\mathbf{p}(t) \cdot \mathbf{p}(0))^2 \rangle$ (b) across ϕ for $\gamma = 20$. The open symbols represent the GCBD data. Schematics of configurational space of $\mathbf{p}(t)$ are highlighted at the bottom for the different phases. In panel(b), the solid lines represent the fitting function in Eq. (3.13). Inset: Zoom-in window highlights that the short-time relaxation of OACF fits an exponential decay governed by a single time scale τ_R .

in the deep nematic regime ($\phi > 20\%$), $A_\infty \rightarrow 1$ and $\tau_R \rightarrow 0$, suggesting strong orientation correlations.

These behaviors can be qualitatively understood by examining the long-time orientation distribution of $\mathbf{p}(t)$ with respect to $\mathbf{p}(0)$. As sketched in the bottom of Fig. 3.3(a), the configurational space of $\mathbf{p}(t)$ exhibits spherical symmetry with the formed angle $\alpha = \arccos(\mathbf{p}(t) \cdot \mathbf{p}(0)) \in [0, \pi]$. In the deep nematic

regime, it approximately reduces to a small and narrow cone-shaped domain with an acute angle α when the probe rotation is strongly confined around $\mathbf{p}(0)$. The cone shape can be described by its maximum opening angle estimated as $\alpha_{max} \sim \pi/2 - \arcsin(S)$. During the I-N transition where steric effects are relatively weak, $\mathbf{p}(t)$ can simultaneously fall into two large cones that are symmetric about $\alpha = \pi/2$ but with unequal probabilities as marked by different colors for the cones. A biased-distribution of $\mathbf{p}(t)$ towards $\alpha = 0$ will cause a slower relaxation process (e.g., $\phi = 17\%$) towards a finite equilibrium value as $t \rightarrow \infty$. On the other hand, as shown in panel(b), a quadratic OACF maintains the fore-aft symmetry, i.e., $\langle (\mathbf{p}(t) \cdot \mathbf{p}(0))^2 \rangle = \langle (-\mathbf{p}(t) \cdot \mathbf{p}(0))^2 \rangle$. Hence the configurational domain of $\mathbf{p}(t)$ automatically switches from a half sphere in the isotropic regime to a single cone domain in the nematic regime, leading to all positive correlations at equilibrium (i.e., $A_\infty > 0$).

Next, we construct a mathematical model to connect the quadratic OACF with the Brownian diffusivity D_r defined in Eq. (3.8). We follow DE's theory [69, 29] to define $\langle (\mathbf{p}(t) \cdot \mathbf{p}(0))^2 \rangle = \int (\mathbf{p}\mathbf{p} : \mathbf{p}'\mathbf{p}') G(\mathbf{p}, \mathbf{p}'; t) \Psi_{eq}(\mathbf{p}') d\mathbf{p}d\mathbf{p}'$ where a Green's function $G(\mathbf{p}, \mathbf{p}'; t)$ represents a conditional (or joint) probability that the probe is in the direction \mathbf{p} at time t , given that it was in the direction $\mathbf{p}(0)$ at $t = 0$. It can be derived from the Smoluchowski equation that the time evolution of $G(\mathbf{p}, \mathbf{p}'; t)$ follows $\frac{\partial G}{\partial t} = D_r \mathcal{R} \cdot \left(\mathcal{R}G + \frac{G}{k_B T} \mathcal{R}U_s \right)$, with the initial condition $G(\mathbf{p}, \mathbf{p}'; t = 0) = \delta(\mathbf{p} - \mathbf{p}')$. Then the time derivative of

$\langle (\mathbf{p}(t) \cdot \mathbf{p}(0))^2 \rangle$ becomes

$$\begin{aligned} \frac{\partial}{\partial t} \langle (\mathbf{p}(t) \cdot \mathbf{p}(0))^2 \rangle = \\ D_r \int \left(\mathcal{R}^2(\mathbf{p}\mathbf{p}) : \mathbf{p}'\mathbf{p}' - \frac{1}{k_B T} (\mathcal{R}(\mathbf{p}\mathbf{p}) : \mathbf{p}'\mathbf{p}') \cdot \mathcal{R}U_s \right) G\Psi_{eq}(\mathbf{p}') d\mathbf{p}d\mathbf{p}' \end{aligned} \quad (3.14)$$

with the first term $\mathcal{R}^2(\mathbf{p}\mathbf{p}) : \mathbf{p}'\mathbf{p}' = -6\mathbf{p}\mathbf{p} : \mathbf{p}'\mathbf{p}' + 2$. Substitute expression of $U_s^{(eq)}$ into the second term, it derives

$$\begin{aligned} -\frac{1}{k_B T} (\mathcal{R}(\mathbf{p}\mathbf{p}) : \mathbf{p}'\mathbf{p}') \cdot \mathcal{R}U_s = \\ \frac{4\zeta_0 S}{k_B T} ((\hat{\mathbf{n}} \cdot \mathbf{p}')(\hat{\mathbf{n}} \cdot \mathbf{p})(\mathbf{p} \cdot \mathbf{p}') - (\hat{\mathbf{n}} \cdot \mathbf{p})^2 (\mathbf{p}\mathbf{p} : \mathbf{p}'\mathbf{p}')) \end{aligned} \quad (3.15)$$

Then we write the triple product term as $(\hat{\mathbf{n}} \cdot \mathbf{p}')(\hat{\mathbf{n}} \cdot \mathbf{p})(\mathbf{p} \cdot \mathbf{p}') = |(\hat{\mathbf{n}} \cdot \mathbf{p}')(\hat{\mathbf{n}} \cdot \mathbf{p})||\mathbf{p} \cdot \mathbf{p}'| \approx (\hat{\mathbf{n}} \cdot \mathbf{p})^2 |\mathbf{p} \cdot \mathbf{p}'|$. A Taylor expansion of the function $f(x) = \sqrt{x}$ to the first order near $x = 1$ yields $|\mathbf{p} \cdot \mathbf{p}'| \approx \frac{1}{2}(\mathbf{p}\mathbf{p} : \mathbf{p}'\mathbf{p}') + \frac{1}{2}$. The term $(\hat{\mathbf{n}} \cdot \mathbf{p})^2$ can approximated through the steady state value of $\langle \mathbf{p}\mathbf{p} : \hat{\mathbf{n}}\hat{\mathbf{n}} \rangle$, which is $(\mathbf{Q}_{eq} + \frac{I}{3}) : \hat{\mathbf{n}}\hat{\mathbf{n}}$ and it gives $(\hat{\mathbf{n}} \cdot \mathbf{p})^2 \approx \frac{2}{3}S + \frac{1}{3}$. Substitute these into Eq.(3.15) and Eq.(3.16), it gives the evolution over time

$$\frac{\partial}{\partial t} \langle (\mathbf{p}(t) \cdot \mathbf{p}(0))^2 \rangle = -6D_r \left[(1+q) \langle (\mathbf{p}(t) \cdot \mathbf{p}(0))^2 \rangle - (q + \frac{1}{3}) \right] \quad (3.16)$$

with $q(S) = \frac{2\zeta_0}{9k_B T} S(S + \frac{1}{2})$ captures the intrinsic I-N transition. After integral, we have the time-dependent solution

$$\langle (\mathbf{p}(t) \cdot \mathbf{p}(0))^2 \rangle = \frac{2}{3(1+q)} \exp[-6(1+q)D_r t] + \frac{3q+1}{3(1+q)}. \quad (3.17)$$

Therefore, comparing Eq. (3.13) and (3.17) yields $A_\infty = \frac{3q+1}{3(1+q)}$ and

$$D_r = \frac{1 - A_\infty}{4\tau_R} \quad (3.18)$$

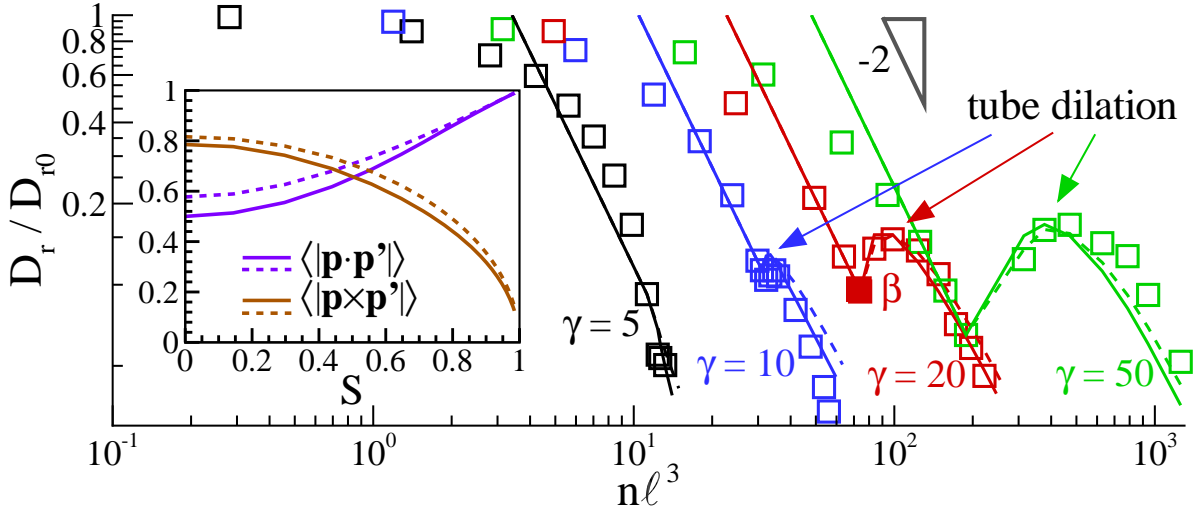


Figure 3.4: D_r/D_{r0} as functions of $n\ell^3$ across ϕ for various γ . The open squares represent the data extracted from GCBD simulations via Eq. (3.18). The solid and dashed lines represent the scaling laws in Eq. (3.20) and (3.25), respectively. The solid red square on the $\gamma = 20$ curve marks the location of the data for fitting β . Inset: $\langle |\mathbf{p} \times \mathbf{p}'| \rangle_{p'}^p$ and $\langle |\mathbf{p} \cdot \mathbf{p}'| \rangle_{p'}^p$ as functions of S , evaluated by using Ψ_{eq} (solid lines) and the quadratic-closure approximation (dashed lines) [2], respectively.

which enable us to extract D_r from OACF measurements. Note that it recovers the classical results $A_\infty = 1/3$ in the isotropic regime when $q = 0$ [29, 63]. For all cases, we present the ratio D_r/D_{r0} (open squares) as functions of a dimensionless number density $n\ell^3$ in Fig. 3.4. Although D_r/D_{r0} decays monotonically across the volume fraction for short rods (e.g., $\gamma = 5$), reverse growths are seen for rods of finite and large aspect ratios ($\gamma > 10$) during the I-N transition. In the deep nematic regime, D_r/D_{r0} becomes to be descending again, suggesting that the probe's self-diffusion motion has been fully constrained.

3.4.3 Scaling law delineated by modified tube model

To understand the complex scaling laws of D_r , as sketched in Fig. 3.5(a), we envision the rotation of a probe to be confined by surrounding neighbors that

are nematically aligned. Inspired by DE's classical theory [29], we enclose the probe in a virtual *tube*. Unlike DE's original semi-dilute model which only considers one effective side-by-side interaction between an infinitesimally-thin probe and its nearest neighbor, we simultaneously track multiple interactions (contacts) attributed from two types of collisions, side-side collisions (denoted by "type I") and end-side/end-end collisions (denoted by "type II"). Intuitively, type II collisions, which were neglected in DE's model, may significantly change the rotational motion because the collision forces have longer moment arms when it occurs at the probe's end.

The conceptual image in Fig. 3.5(a) of a restricted collision-driven rotational motion is supported by a series of GCBD simulation data that reveal intriguing geometric features. As shown in Fig. 3.5(b), we examine the fractional contributions of the two types of collisions relative to the total number of collisions, i.e., $\lambda_{I,II} = N_{I,II} / (N_I + N_{II})$, where $N_{I,II}$ represent the time-average collision numbers. For short rods (e.g., $\gamma = 5$), the type II collisions dominate in both the isotropic and nematic regimes; while for relatively long rods (e.g., $\gamma = 20$), the type I collisions are more frequent in the isotropic regime, but they are significantly reduced during the I-N transition, and become much less compared to the type II collisions in the nematic regime. Not surprisingly, all data for a re-scaled collision number ratio $\lambda_I / (\gamma \lambda_{II})$ approximately collapse onto a master curve since the collision numbers are purely determined by the surface areas of the sidewall and the ends. In panel(d), we define an orientational pair-correlation function (OPCF) in the rod's transverse direction [70, 71, 72]

$$g(r_{\perp}) = \frac{\sum_{i \neq j} \langle P_2(\mathbf{p}_i \cdot \mathbf{p}_j) \delta(r_{\perp} - \sqrt{|\mathbf{r}_{ij}|^2 - (\mathbf{r}_{ij} \cdot \mathbf{p}_i)^2}) \rangle}{\sum_{i \neq j} \langle \delta(r_{\perp} - \sqrt{|\mathbf{r}_{ij}|^2 - (\mathbf{r}_{ij} \cdot \mathbf{p}_i)^2}) \rangle}$$
 where \mathbf{r}_{ij} connects the center-of-mass positions of the i th and j th rods, and r_{\perp} measured the projected distance between the rods in perpendicular direction of \mathbf{p}_i . Again, all data for a re-scaled OPCF $\frac{g(r_{\perp}) - g_{min}}{g_{max} - g_{min}}$ by using the maximum (when $r_{\perp} = b$) and minimum (when $r_{\perp} > 4b$) values of g , especially for rods of high aspect ratios, approximately fall onto a master curve. These shape-independent features provides guidance of how to construct analytical models that accurately reflect the relative contributions of two types of steric interactions.

As illustrated in Fig. 3.5(a), we assume a probe oriented in the \mathbf{p} -direction has a thickness b and length ℓ , sitting among nematically-aligned neighbors whose orientation distribution can be described by Ψ_{eq} . We estimate the number of penetrations into a virtual *tube* that has the same rod length ℓ . As suggested by Fig. 3.5(d), the *tube* radius a_T approximately varies between b and $3b$ where the OPCFs exhibit significant correlations. Following DE's approach [29], we consider the number of rods that penetrate a small surface area ΔS with a unit normal vector \mathbf{n} can be calculated as $\Delta \mathcal{N} = n\ell \Delta S \langle |\mathbf{p}' \cdot \mathbf{n}| \rangle$ where the configurational average is performed in a representative volume along the \mathbf{p}' -direction. For the sidewall intersections (i.e., $\mathbf{n} \perp \mathbf{p}$) arising from the type I collisions, we reuse DE's calculation [29] to sum $\Delta \mathcal{N}$ over half of the sidewall area $S_I = \pi a_T \ell$ by taking into account the double-penetration from a vicinal rod, and obtain the number $\mathcal{N}_I = S_I n \ell \langle |\mathbf{p} \cdot \mathbf{n}| \rangle_{\mathbf{p}'}^p = 2n a_T \ell^2 \langle |\mathbf{p} \times \mathbf{p}'| \rangle_{\mathbf{p}'}^p$ (see the derivation details in Ref [29]). Here $\langle \rangle_{\mathbf{p}'}^p$ represents configurational averages over both \mathbf{p} and \mathbf{p}' . Likewise, the number of rods intersecting from the two ends (i.e., $\mathbf{n} \parallel \mathbf{p}$ and the

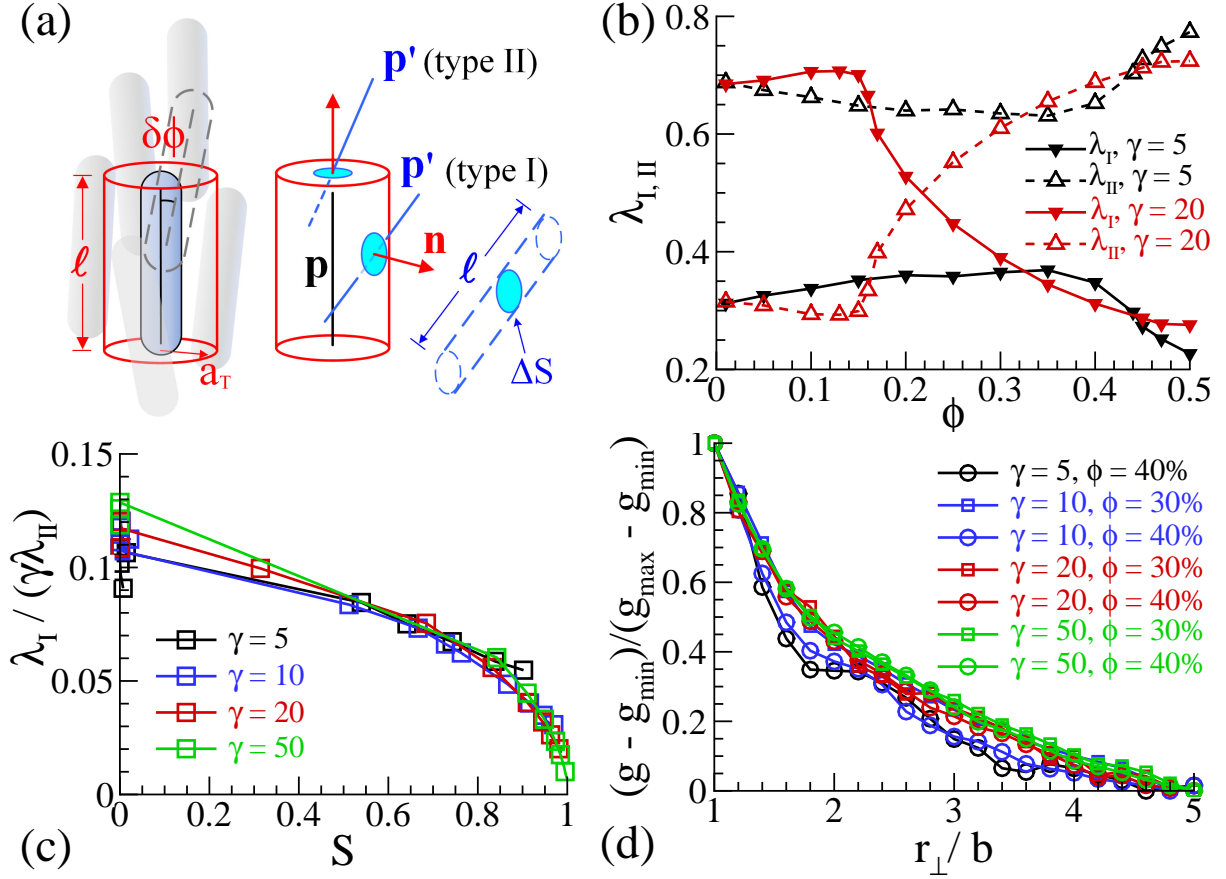


Figure 3.5: GCBD simulations motivate a new *tube* model. (a) Schematic of a virtual *tube* with penetrations from both the sidewall and the two ends. (b) Fractional contributions of the averaged collision numbers on the sidewall (λ_I) and the ends (λ_{II}) for $\gamma = 5$ and 20 as functions of ϕ . (c) The collision number ratio $\lambda_I / (\gamma\lambda_{II})$ as functions of S for various γ . (d) The OPCF $g(r_{\perp})$ in the nematic regime as functions of the dimensionless transverse distance r_{\perp}/b .

total area $S_{II} = 2\pi a_T^2$) can be calculated in a straightforward manner as $\mathcal{N}_{II} = S_{II}n\ell\langle|\mathbf{p} \cdot \mathbf{n}|\rangle_{p'}^p = 2n\pi a_T^2\ell\langle|\mathbf{p} \cdot \mathbf{p}'|\rangle_{p'}^p$ by assuming that the surrounding rods only penetrate the tube once.

To avoid double-counting the neighboring rods that penetrate from the side and one end simultaneously, we calculate the total penetration number as

$$\begin{aligned}\mathcal{N}_p &= \omega_I \mathcal{N}_I + \omega_{II} \mathcal{N}_{II} \\ &= 2\omega_I n a_T \ell^2 \langle|\mathbf{p} \times \mathbf{p}'|\rangle_{p'}^p + 2\omega_{II} n \pi a_T^2 \ell \langle|\mathbf{p} \cdot \mathbf{p}'|\rangle_{p'}^p.\end{aligned}\quad (3.19)$$

Since the calculations of $\mathcal{N}_{I,II}$ have incorporated the shape effect, according

to Fig. 3.5(c), we assume the weights $\omega_{I,II}(S)$ are shape-independent, and will be selected such that \mathcal{N}_I and \mathcal{N}_{II} coexist in the isotropic regime but \mathcal{N}_I vanishes in the “sharply-aligned” limit where all rods are perfectly aligned (i.e., $S = 1$). We assume the probe rotates a small angle $\delta\phi$ as it moves for a distance of rod length ℓ during the “reptation” time scale $\tau_0 \propto D_{r0}^{-1}$, which leads to $D_r = \delta\phi^2/\tau_0 = \beta\delta\phi^2 D_{r0}$ with β a shape-dependent constant. Considering the fact that the probe encounters these \mathcal{N}_p penetrations with equal probability, we estimate $\delta\phi = \frac{a_T}{\mathcal{N}_p \ell}$, yielding $D_r/D_{r0} = \beta(n\ell^3)^{-2} \left[\omega_I \langle |\mathbf{p} \times \mathbf{p}'| \rangle_{p'}^p + \pi\omega_{II} \left(\frac{a_T}{\ell} \right) \langle |\mathbf{p} \cdot \mathbf{p}'| \rangle_{p'}^p \right]^{-2}$. The β value for each γ case can be numerically fitted by matching D_r/D_{r0} with the GCBD data on a point at the onset of the I-N transition (as one example, see the solid red square marked on the $\gamma = 20$ curve in Fig. 3.4) [60, 61, 73, 29, 74].

After β is fixed, we find that choosing $\omega_I = \langle |\mathbf{p} \times \mathbf{p}'| \rangle_{p'}^p$, $\omega_{II} = \langle |\mathbf{p} \cdot \mathbf{p}'| \rangle_{p'}^p$, and the *tube* radius $a_T \approx 2b$ leads to excellent agreements between the GCBD data. The analytical form can be written as

$$\frac{D_r}{D_{r0}} = \beta(n\ell^3)^{-2} \left[\left(\langle |\mathbf{p} \times \mathbf{p}'| \rangle_{p'}^p \right)^2 + \frac{2\pi}{\gamma} \left(\langle |\mathbf{p} \cdot \mathbf{p}'| \rangle_{p'}^p \right)^2 \right]^{-2} \quad (3.20)$$

where the two double-configurational-averages are evaluated by using Ψ_{eq} . The inset of Fig. 3.4 reveals the intrinsic competing mechanism for the non-monotonic critical behaviors of D_r . Mathematically, we see that the enhanced rotational diffusions observed during the I-N transition are caused by the divergent behaviors of Eq. (3.20) as $\langle |\mathbf{p} \times \mathbf{p}'| \rangle_{p'}^p$ approaches zero at large S which suggests weakened side-side steric interactions as the probe reptates. Such “*tube* dilation” effect is regulated by the enhanced end-steric effects in the nematic regime as $\langle |\mathbf{p} \cdot \mathbf{p}'| \rangle_{p'}^p$ dominates, especially for relatively

short rods with small γ .

3.4.4 Approximations of the double-configurational averages

We perform analytical calculation of the two configurational averages

$\langle |\mathbf{p} \times \mathbf{p}'| \rangle_{p'}^p$ and $\langle |\mathbf{p} \cdot \mathbf{p}'| \rangle_{p'}^p$. We first define $\mathbf{m} = \mathbf{p}\mathbf{p} - \mathbf{I}/3$, and rewrite

$$\begin{aligned} |\mathbf{p} \cdot \mathbf{p}'| &= \sqrt{\mathbf{p}\mathbf{p} : \mathbf{p}'\mathbf{p}'} = \sqrt{\frac{1}{3}} \sqrt{1 + 3\mathbf{m} : \mathbf{m}'}, \\ |\mathbf{p} \times \mathbf{p}'| &= \sqrt{1 - \mathbf{p}\mathbf{p} : \mathbf{p}'\mathbf{p}'} = \sqrt{\frac{2}{3}} \sqrt{1 - \frac{3}{2}\mathbf{m} : \mathbf{m}'} \end{aligned} \quad (3.21)$$

For the first expression in (3.21), we perform Taylor expansions in terms of $\mathbf{m} : \mathbf{m}'$, leading to

$$|\mathbf{p} \cdot \mathbf{p}'| = \sqrt{\frac{1}{3}} \left(1 + \frac{3}{2}\mathbf{m} : \mathbf{m}' - \frac{9}{8}(\mathbf{m} : \mathbf{m}')^2 + \frac{27}{16}(\mathbf{m} : \mathbf{m}')^3 + \dots \right) \quad (3.22)$$

To proceed, we employ a quadratic closure to express the high-order-moments in terms of the lower-order moments, leading to $\langle \overbrace{\mathbf{m}\mathbf{m}\dots\mathbf{m}\mathbf{m}}^N \rangle_p = \overbrace{\mathbf{Q}\mathbf{Q}\dots\mathbf{Q}\mathbf{Q}}^N$.

Hence we have

$$\begin{aligned} &\langle |\mathbf{p} \cdot \mathbf{p}'| \rangle_{p'}^p \\ &\approx \sqrt{\frac{1}{3}} \left(1 + \frac{3}{2}\mathbf{Q} : \mathbf{Q}' - \frac{9}{8}(\mathbf{Q} : \mathbf{Q}')^2 + \frac{27}{16}(\mathbf{Q} : \mathbf{Q}')^3 + \dots \right) \\ &= \sqrt{\frac{1}{3}} \sqrt{1 + 2S^2}. \end{aligned} \quad (3.23)$$

Similarly, the second term in (3.21) can be calculated as

$$\langle |\mathbf{p} \times \mathbf{p}'| \rangle_{p'}^p \approx \sqrt{\frac{2}{3}} \sqrt{1 - S^2}. \quad (3.24)$$

Then Eq. (3.20) can be rewritten as

$$\frac{D_r}{D_{r0}} \approx \beta(n\ell^3)^{-2} \left[\left(1 + \frac{\pi}{\gamma} \right) + \left(\frac{2\pi}{\gamma} - 1 \right) S^2 \right]^{-2}. \quad (3.25)$$

As shown by the dashed lines in Fig. 3.4, the above equation provides accurate yet convenient form without using Ψ_{eq} . For thin rods ($\gamma \rightarrow \infty$), Eq. (3.25) captures the DE's semi-dilute theory in the isotropic regime when $S = 0$. It also recovers DE's correction in the nematic regime when $S > 0$ and $\gamma \rightarrow \infty$ by considering the *tube*-dilation effect only [75, 29, 76], which, however, becomes singular in the limit $S \rightarrow 1$. We can further predict that such dilation effects only occur for rods with $\gamma > 2\pi$ as the resultant negative sign of the S^2 term directly causes reverse growing. This can be verified by the $\gamma = 7$ case where D_r/D_{r0} approximately follows the $(n\ell^3)^{-2}$ law in the nematic regime.

3.5 Conclusion

In summary, we have built a Doi-Onsager model for characterizing the long-time Brownian diffusivity D_r in the nematic regime for concentrated rod suspensions. The non-monotonic critical behaviors of D_r are accurately captured via a new *tube* model. We have shown that when appropriately incorporating steric hindrances around a probe rod, DE's *tube* concept can elegantly yet accurately describe topologically-constrained rod rotation in a concentrated meshwork without scrutinizing detailed rod-rod interactions. While hydrodynamic interactions are neglected, we expect our scaling law remains accurate for dense rod suspensions where the short-range steric shielding dominates. We anticipate this model will provide a new angle in characterizing Brownian rotations in a wide variety of computational and experimental studies of soft condensed matter.

3.6 Future plan

There is still a lack of a thorough understanding of the long-time translational Brownian diffusivity Dt for dense suspensions of hard rods of finite aspect ratios. It is meaningful to explore the scaling of Dt as a function of volume fraction ϕ . Besides, it may be a good try to expand to the active system with hydrodynamics effect, to see what the steric interactions bring to the existing Taylor dispersion theory, which describes an effect in fluid mechanics where a shear flow can increase the effective diffusivity of particles.

Q –TENSOR MODEL FOR UNDULATORY SWIMMING IN A LIQUID CRYSTAL

4.1 Abstract

Microorganisms take full advantage of anisotropic drag forces when swimming in low-Reynolds-number flows where the inertia effect is negligible. Besides adopting various swimming gaits, they may exploit anisotropic properties of the coupling liquid medium for efficient swimming or locomotion. In this paper, we build a computation model to study the nonlinear dynamics of an undulatory microswimmer in a quasi-2D liquid-crystal polymer solution. We describe the polymer fluid phase using a hydrodynamic Q –tensor model for rigid microrods, and treat the swimmer as a finite-length fiber whose undulatory motion is actuated by imposing propagating traveling waves on the body curvature. The fluid-structure interactions are resolved via an immersed boundary method. Compared to the dynamics in Newtonian fluids, we observe rich non-Newtonian behaviors of both enhanced and retarded swimming motions when calculating the swimmer’s mean speed. We reveal the propulsion mechanism by analyzing the near-body flow fields and polymeric force distributions, together with asymptotic analysis for an idealized model built upon Taylor’s swimming sheet.

4.2 Introduction

Many organisms live in microfluidic environments, either biological or synthetic, where the fluid inertia is negligible. In the so-called Stokes (or creeping) flows, Purcell's Scallop theorem explains that performing time-reversible motions cannot generate directional swimming or locomotion due to kinematic reversibility ([77]). Instead, microswimmers often adopt special propulsion strategies (swimming gaits). Especially for those with slender shapes or having thin appendages (e.g., *C. elegans*, *E. coli*, *B. subtilis*), it is well-understood that they can perform undulation or flagellar beating to generate directional motions by breaking symmetry ([78]). On the other hand, people have conducted extensive research to reveal rich dynamics and new propulsion mechanisms of microorganisms that utilize the complex fluids' intrinsic anisotropy arising from their non-Newtonian physical and rheological properties. For example, while the extra particle stresses from shear-thinning viscoelastic (e.g., Oldroyd B) fluids generally impose additional hindrance effects, it has been found that undulatory swimmers such as *C. elegans* may leverage their finite body-length and polymeric stress relaxation to achieve a higher swimming speed than that in the Newtonian fluids ([79, 80, 81]). Furthermore, there has been a growing interest in exploring non-equilibrium physics of biosynthetic active materials "powered" by many-swimmer interactions in complex fluids that are capable of exploiting collective dynamics for useful mechanical work ([3, 5]). Of particular interest is the study of motile bacteria in lyotropic nematic liquid crystals (LC) wherein the extra stress generation is directly determined by the LC molecule orientation

(or the so-called orientation order), leading to intriguing optical and mechanical properties ([82, 83]).

So far, there have been several models proposed to study the dynamics of microswimmers in LCs. [82, 84] constructed a hydrodynamic Ericksen-Leslie (EL) model to solve for the orientation variation of the director field in the LC with motile bacteria (*B. subtilis*) with prescribed translational motions, and illustrated how the induced shear determines the ordering patterns (or birefringent cloud) around the swimmer. [85] studied the motion of Taylor’s swimming sheet with imposed small-amplitude travelling waves in LC via a similar EL model. When enforcing the local LC orientation to be tangential to the undulatory body (i.e., tangential anchoring), they derived the asymptotic solutions, which, for the first time, mathematically reveal how the undulatory gaits are controlled by LC’s material parameters ([86, 87]). Later [88] used the Immersed Boundary (IB) method to simulate a finite-length undulatory swimmer in LCs confined between two parallel walls, when subjected to large-amplitude actuation and the tangential anchoring condition, and only found retarded motions compared to the swimming speed in the Newtonian fluid. However, as they pointed out, the EL model cannot be robustly extended to more general cases, and may break down when applying other types (e.g., homeotropic) of anchoring conditions.

Motivated by the prior studies and to further seek quantitative understanding of undulatory swimming mechanisms in LCs, we present a new computational framework which is built upon a minimal Q -tensor model coarse-grained from the Doi-Onsager kinetic model for rigid microrods ([29]).

The swimmer is treated as a finite-length elastic fiber whose undulation is activated by imposing traveling waves on its body curvature. An IB method is employed to solve the fluid/structure interactions (FSIs) between the swimmer and LCs. Interestingly, our simulations reveal both enhanced and retarded swimming motions in the nematic regime, corresponding to the scenarios when the swimming direction is parallel and perpendicular to the LC's alignment directions, respectively. These observations are different from [88] who only see retarded motions. Our numerical results are qualitatively confirmed by performing the asymptotic analysis of Taylor's swimming sheet model, and can be further understood by revealing the unique near-body polymer force distributions.

4.3 Mathematical Model

In the kinetic model by [29], a probability distribution function (PDF) $\Psi(\mathbf{x}, \mathbf{p}, t)$ is employed to describe the ensemble dynamic of microrods in terms of the rod's center-of-mass (C.O.M.) position \mathbf{x} and orientation \mathbf{p} ($|\mathbf{p}| = 1$). When simulating the macro scale hydrodynamic interactions between rods and ambient flows, it is often preferred to use coarse-grained PDEs that are derived via proper moment closure to eliminate \mathbf{p} due to their low computation costs. Consider rodlike LC molecules with fore-aft symmetry and uniform length ℓ . In the fluid domain Ω_f , a two-dimensional hydrodynamic LC model can be derived for the second-moment tensor $\mathbf{D} = \int_p \mathbf{p}\mathbf{p}\Psi d\mathbf{p}$ as ([29]):

$$\nabla \cdot \mathbf{D} + 2\mathbf{E} : \mathbf{S} = 4\zeta d_r(\mathbf{D} \cdot \mathbf{D} - \mathbf{D} : \mathbf{S}) - 4d_r \left(\mathbf{D} - \frac{\mathbf{I}}{2} \right) + d_t \Delta \mathbf{D}, \quad (4.1)$$

where $\overset{\nabla}{\mathbf{D}} = \frac{\partial \mathbf{D}}{\partial t} + \mathbf{u} \cdot \nabla \mathbf{D} - (\mathbf{D} \cdot \nabla \mathbf{u} + \nabla \mathbf{u}^T \cdot \mathbf{D})$ is the so-called upper-convected time derivative, $\mathbf{E} = \frac{1}{2} (\nabla \mathbf{u} + \nabla \mathbf{u}^T)$ is the strain-rate tensor, and $\mathbf{S} = \int_p \mathbf{p} \mathbf{p} \mathbf{p} \mathbf{p} \Psi d\mathbf{p}$ is the fourth-moment tensor. The first term on the right-hand-side (R.H.S.) represents the steric alignment effects arising from the Maier-Saupe (MS) potential $U_{MS}(\mathbf{p}) = -\zeta \mathbf{p} \mathbf{p} : \mathbf{D}$, with ζ the dimensionless strength coefficient ([31]). The diffusivity coefficients d_t and d_r originate from the translational and rotational Brownian motion, respectively. The above equation is a minimal “ Q -tensor” model since the trace-free (normalized) tensor-order parameter, the so-called Q -tensor, is defined by $\mathbf{Q}(\mathbf{x}, t) = c^{-1} \mathbf{D} - \mathbf{I}/2$, with $c(\mathbf{x}, t) = 1$ the concentration field (i.e., zeroth-moment of Ψ) that remains to be homogeneous constant. In 2D, the tensor \mathbf{Q} has a maximal nonnegative eigenvalue ρ satisfying $0 \leq \rho \leq \frac{1}{2}$. Assuming that ρ is isolated, then we call its associated unit eigenvector the director \mathbf{m} , and $0 \leq S = 2\rho \leq 1$ the orientation order parameter. The incompressible fluid velocity \mathbf{u} is incorporated via a mean-field fashion, and is governed by the forced Stokes equation: $\nabla p - \mu_f \Delta \mathbf{u} = \nabla \cdot \boldsymbol{\sigma}_p + \mathbf{f}_e$, where μ_f is the fluid viscosity, and $\mathbf{f}_e(\mathbf{x}, t)$ represents the force exerted by the motile swimmer. The extra stress due to the LC polymer solution is defined as ([75, 89, 76])

$$\boldsymbol{\sigma}_p = 2\nu k_B T \left(\mathbf{D} - \frac{\mathbf{I}}{2} \right) - 2\nu k_B T \zeta (\mathbf{D} \cdot \mathbf{D} - \mathbf{S} : \mathbf{D}) + \frac{\nu k_B T \beta_0}{2d_r (\nu \ell^3)^2} \mathbf{E} : \mathbf{S} \quad (4.2)$$

where $\nu \sim \ell^{-3}$ is an effective volume fraction, $k_B T$ is the thermal energy scale, $\beta_0 (\nu \ell^3)^{-2}$ represents a crowdedness factor with β_0 being an empirical coefficient. In this study, we will choose a small empirical crowdedness factor $\beta_0 (\nu \ell^3)^{-2} \sim 10^{-3} - 10^{-4}$ as suggested by [89] and [76].

In the Lagrangian frame (Ω_L) for the undulatory swimmer of length L_s , its kinematics can be described by the parametric form $\mathbf{X}(s, t)$, with s the local arc length $s \in [0, L_s]$. The actual shape $\mathbf{X}(s, t)$ is determined by penalizing deviations from actuation imposed on the body curvature $\kappa_0(s, t)$:

$$\kappa_0(s, t) = -k^2 A_0 \sin(k s - \omega t), \quad (4.3)$$

starting from an initial configuration given by $\mathbf{X}(s, t = 0) = (s, A_0(\sin(k s)))$. Equation (4.3) describe the right-propagating traveling waves with amplitude A_0 , wavenumber k , and angular frequency ω . Imposing actuation in Eq. (4.3) produces elastic forces $\mathbf{F}_e(\mathbf{X})$ along the body, and effectively drive periodic shape changes (or swimming gaits). Following [90], the Lagrangian body force can be derived by performing the variational derivative upon the elastic energy E , i.e., $\mathbf{F}_e(\mathbf{X}) = -\frac{\delta E[\mathbf{X}(s, t)]}{\delta \mathbf{X}}$. Here the total elastic energy $E[\mathbf{X}]$ include the contributions from both stretching (denoted by subscript s) and bending (denoted by subscript b) deformation

$$E[\mathbf{X}(s, t)] = \frac{\sigma_s^0}{2} \int_{\Omega_L} \left(\left| \frac{\partial \mathbf{X}}{\partial s} \right| - 1 \right)^2 ds + \frac{\sigma_b^0}{2} \int_{\Omega_L} \left(\frac{\partial^2 \mathbf{X}}{\partial s^2} \cdot \mathbf{n} - \kappa_0 \right)^2 ds \quad (4.4)$$

where \mathbf{n} denotes the local normal direction. Using the IB method, the Eulerian forcing term \mathbf{f}_e can be calculated by

$$\mathbf{f}_e(\mathbf{x}, t) = \int_{\Omega_L} \mathbf{F}_e(s, t) \delta(\mathbf{x} - \mathbf{X}(s, t)) ds, \quad (4.5)$$

where δ denotes the Dirac delta function that maps between the Eulerian (Ω_f) and Lagrangian (Ω_L) domain. Likewise, the Lagrangian velocity can be interpolated from the nearby Eulerian grids via

$$\frac{\partial \mathbf{X}}{\partial t} = \mathbf{U}(s, t) = \int_{\Omega_E} \mathbf{u}(\mathbf{x}, t) \delta(\mathbf{X}(s, t) - \mathbf{x}) d\mathbf{x}. \quad (4.6)$$

For nondimensionalization, we choose the wavelength $\lambda = 2\pi k^{-1}$ the length scale, wave speed ω/k the velocity scale, $2\nu k_B T$ the polymer stress scale, which lead to the dimensionless equations in the LC phase after proper re-scaling:

$$\nabla \cdot \mathbf{u} = 0, \quad \nabla p - \Delta \mathbf{u} = Er \nabla \cdot \boldsymbol{\tau}_p + \mathbf{f}_e, \quad (4.7)$$

$$\boldsymbol{\tau}_p = \left(\mathbf{D} - \frac{\mathbf{I}}{2} \right) - \zeta (\mathbf{D} \cdot \mathbf{D} - \mathbf{S} : \mathbf{D}) + \beta \mathbf{E} : \mathbf{S}, \quad (4.8)$$

$$\overset{\nabla}{\mathbf{D}} + 2\mathbf{E} : \mathbf{S} = \frac{\zeta}{Pe} (\mathbf{D} \cdot \mathbf{D} - \mathbf{D} : \mathbf{S}) - \frac{1}{Pe} \left(\mathbf{D} - \frac{\mathbf{I}}{2} \right) + \frac{1}{Pe_t} \Delta \mathbf{D}. \quad (4.9)$$

Here we define two Péclet numbers, $Pe = \frac{\omega}{8\pi d_r}$ ($\sim O(1) - O(10)$) and $Pe_t = \frac{2\pi\omega}{d_t k^2}$ ($\sim O(10) - O(100)$), which represent the ratio of the time scales for rod's rotation and transport over that of undulation (i.e., ω^{-1}), respectively. Especially Pe characterizes the time evolution of LC's orientation field (so-called nematic elasticity). In comparison, we only consider minimal or negligible translational diffusion effect, and choose Pe_t to be at least one order of magnitude higher than Pe . The LC-fluid coupling is characterized by the Ericksen number $Er = \frac{4\pi\nu k_B T}{\mu_f \omega}$ ([91, 85]). Higher (lower) Er values correspond to the stronger (weaker) flow modification on the LC configuration. And $\beta = \frac{\beta_0 \omega}{8\pi d_r (\nu \ell^3)^2}$ is an effective crowding coefficient. Equations (4.3)-(4.4) and the two mapping functions (4.5) and (4.6) retain the same mathematical forms, with the dimensionless parameters $\sigma_s = \frac{\sigma_s^0 2\pi k}{\omega^2}$, $\sigma_b = \frac{\sigma_b^0 k^3}{2\pi \omega^2}$.

We fix the wavenumber $k = 2\pi$, and set the dimensionless swimmer length L be the same as the wavelength, i.e., $L = L_s k / 2\pi = 1$, and the amplitude $A = A_0 k = 0.05$. We choose a large stretching stiffness $\sigma_s = O(10^3)$ to enforce inextensibility, but vary the bending stiffness σ_b between 0.005 and 0.5.

We then use a pseudo-spectral method to solve the above equations.

4.4 Numerical method

In the solid phase, the elastic body force $\mathbf{F}_e(F_x, F_y)$ is calculated explicitly at each time step. Following the IB approaches in Refs [92, 93], we discretize the variational derivative of the bending energy functional, and derive the following component form for the i th node at the position $\mathbf{X}_i(X_i, Y_i)$:

$$\begin{cases} F_{x,i} = \frac{\sigma_s}{\Delta s} \left[\left(\frac{|\mathbf{X}_{i+1} - \mathbf{X}_i|}{\Delta s} - 1 \right) \left(\frac{X_{i+1} - X_i}{|\mathbf{X}_{i+1} - \mathbf{X}_i|} \right) - \left(\frac{|\mathbf{X}_i - \mathbf{X}_{i-1}|}{\Delta s} - 1 \right) \left(\frac{X_i - X_{i-1}}{|\mathbf{X}_i - \mathbf{X}_{i-1}|} \right) \right] \\ \quad - \frac{\sigma_b}{\Delta s^3} \left((\kappa - \kappa_0)_{i-1} (Y_{i-1} - Y_{i-2}) - (\kappa - \kappa_0)_i (Y_{i+1} - Y_{i-1}) + (\kappa - \kappa_0)_{i+1} (Y_{i+2} - Y_{i+1}) \right) \\ F_{y,i} = \frac{\sigma_s}{\Delta s} \left[\left(\frac{|\mathbf{X}_{i+1} - \mathbf{X}_i|}{\Delta s} - 1 \right) \left(\frac{Y_{i+1} - Y_i}{|\mathbf{X}_{i+1} - \mathbf{X}_i|} \right) - \left(\frac{|\mathbf{X}_i - \mathbf{X}_{i-1}|}{\Delta s} - 1 \right) \left(\frac{Y_i - Y_{i-1}}{|\mathbf{X}_i - \mathbf{X}_{i-1}|} \right) \right] \\ \quad + \frac{\sigma_b}{\Delta s^3} \left((\kappa - \kappa_0)_{i-1} (X_{i-1} - X_{i-2}) - (\kappa - \kappa_0)_i (X_{i+1} - X_{i-1}) + (\kappa - \kappa_0)_{i+1} (X_{i+2} - X_{i+1}) \right) \end{cases} \quad (4.10)$$

where the curvature κ is defined as $\kappa_i = \hat{\mathbf{e}}_z \cdot (\mathbf{X}_{i+1} - \mathbf{X}_i) \times (\mathbf{X}_i - \mathbf{X}_{i-1}) / \Delta s^3$, and $\Delta s = L/N_s$. When mapping between the Lagrangian and Eulerian (\mathbf{x}) meshes, we use a four-point smoothed Dirac delta function $\phi(r)$ [92, 94]:

$$\delta(\mathbf{x} - \mathbf{X}) = \frac{1}{h^2} \phi\left(\frac{x - X}{h}\right) \phi\left(\frac{y - Y}{h}\right) \quad (4.11)$$

where delta function $\phi(r)$ is constructed as

$$\phi(r) = \begin{cases} 0, & |r| \geq 2, \\ \frac{1}{8} \left(5 - 2|r| - \sqrt{-7 + 12|r| - 4r^2} \right), & 2 \geq |r| \geq 1, \\ \frac{1}{8} \left(3 - 2|r| + \sqrt{1 + 4|r| - 4r^2} \right), & 1 \geq |r| \geq 0. \end{cases} \quad (4.12)$$

In the LC phase, we first solve the constitutive equations for the velocity \mathbf{u} and the second-moment tensor \mathbf{D} . Here we use the method by Vaithianathan

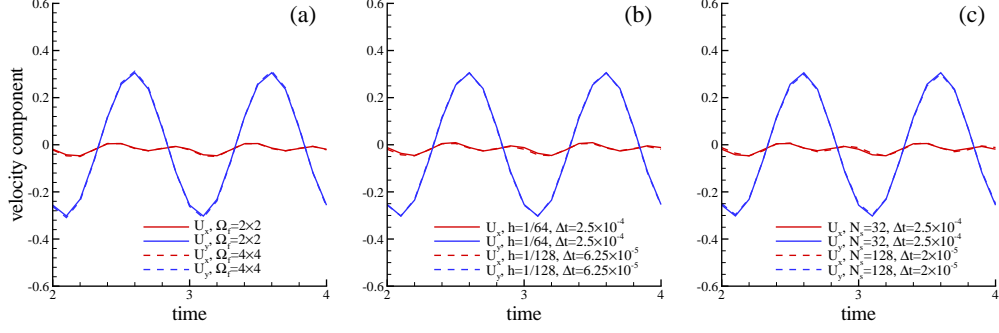


Figure 4.1: Convergence tests of a parallel moving swimmer with the time-dependent C.O.M. velocity $\mathbf{U}(U_x, U_y)$ by varying (a) domain size ($\Delta t = 6.25 \times 10^{-5}$, $h = 1/128$), (b) Eulerian grid width ($\Omega_f = 2 \times 2$), and (c) Lagrangian grid spacing ($\Omega_f = 2 \times 2$, $h = 1/128$). These parameters are fixed: $Pe = 10$, $Pe_t = 100$, $Er = 1$, $\beta = 0.005$, $\zeta = 8$, $L = 1$, $A = 0.05$, $k = 2\pi$, $\omega = 2\pi$, $\sigma_b = 0.5$, $\sigma_s = 1500$.

and Collins [95] to enforce the symmetric positive definiteness of \mathbf{D} whose diagonal components are bounded, i.e., $\text{tr}(\mathbf{D}) = D_{11} + D_{22} = 1$ where $0 \leq D_{11}, D_{22} \leq 1$. A Cholesky decomposition

$$\mathbf{D} = \mathbf{L} \cdot \mathbf{L}^T = \begin{pmatrix} l_{11} & 0 \\ l_{21} & l_{22} \end{pmatrix} \begin{pmatrix} l_{11} & l_{21} \\ 0 & l_{22} \end{pmatrix} = \begin{pmatrix} l_{11}^2 & l_{11}l_{21} \\ l_{11}l_{21} & l_{21}^2 + l_{22}^2 \end{pmatrix} \quad (4.13)$$

is used, where \mathbf{L} is a lower triangular matrix. Then we transform the components of \mathbf{L} again via

$$\begin{cases} l_{11} = \frac{1}{\pi} \arctan \eta + \frac{1}{2}, \\ l_{22} = \frac{1}{\pi} \arctan \gamma + \frac{1}{2}, \\ l_{21} = \frac{2}{\pi} \arctan \chi. \end{cases} \quad (4.14)$$

Substituting Eqs. (4.13-4.14) into the evolution equation of \mathbf{D} , we get

$$\left\{ \begin{array}{l} \frac{\partial \eta}{\partial t} + u_x \frac{\partial \eta}{\partial x} + u_y \frac{\partial \eta}{\partial y} = \pi (1 + \eta^2) \left[l_{11} \frac{\partial u_x}{\partial x} + l_{21} \frac{\partial u_x}{\partial y} - \frac{1}{2Pe} \left(l_{11} - \frac{1}{2l_{11}} \right) \right. \\ \quad \left. + \frac{1}{Pe_t} \frac{1}{2l_{11}} \Delta D_{11} - \frac{1}{2l_{11}} K_{11} \right] \\ \\ \frac{\partial \chi}{\partial t} + u_x \frac{\partial \chi}{\partial x} + u_y \frac{\partial \chi}{\partial y} \\ = \frac{\pi}{2} (1 + \chi^2) \left[l_{11} \frac{\partial u_y}{\partial x} + \frac{l_{22}^2}{l_{11}} \frac{\partial u_x}{\partial y} - l_{21} \frac{\partial u_x}{\partial x} - \frac{1}{2Pe} \left(l_{21} + \frac{l_{21}}{2l_{11}^2} \right) \right. \\ \quad \left. - \frac{1}{Pe_t} \frac{l_{21}}{2l_{11}^2} \Delta D_{11} + \frac{1}{Pe_t} \frac{1}{l_{11}} \Delta D_{12} + \frac{l_{21}}{2l_{11}^2} K_{11} - \frac{1}{l_{11}} K_{12} \right] \\ \\ \frac{\partial \gamma}{\partial t} + u_x \frac{\partial \gamma}{\partial x} + u_y \frac{\partial \gamma}{\partial y} \\ = \pi (1 + \gamma^2) \left[l_{22} \frac{\partial u_y}{\partial y} - \frac{l_{22}l_{21}}{l_{11}} \frac{\partial u_x}{\partial y} + \frac{1}{2Pe} \left(\frac{l_{21}^2}{2l_{22}l_{11}^2} - l_{22} + \frac{1}{2l_{22}} \right) \right. \\ \quad + \frac{1}{Pe_t} \frac{l_{21}^2}{2l_{22}l_{11}^2} \Delta D_{11} - \frac{1}{Pe_t} \frac{l_{21}}{l_{22}l_{11}} \Delta D_{12} + \frac{1}{Pe_t} \frac{1}{2l_{22}} \Delta D_{22} \\ \quad \left. - \frac{l_{21}^2}{2l_{22}l_{11}^2} K_{11} + \frac{l_{21}}{l_{22}l_{11}} K_{12} - \frac{1}{2l_{22}} K_{22} \right] \end{array} \right. \quad (4.15)$$

where $\mathbf{K} = 2\mathbf{E} : \mathbf{S} - \frac{\zeta}{Pe}(\mathbf{D} \cdot \mathbf{D} - \mathbf{D} : \mathbf{S})$. After solving the \mathbf{D} field, we evaluate the polymer stress $\boldsymbol{\tau}_p$, and then directly compute the 2D velocity field $\mathbf{u} = (u_x, u_y)$ in the Fourier space as:

$$\tilde{\mathbf{u}} = \frac{1}{\xi^2} \left(\mathbf{I} - \hat{\boldsymbol{\xi}} \hat{\boldsymbol{\xi}} \right) \cdot \tilde{\mathbf{f}}_{total} \quad (4.16)$$

where $\mathbf{f}_{total} = Er \nabla \cdot \boldsymbol{\tau}_p + \mathbf{f}_e$, $\hat{\boldsymbol{\xi}}$ is the wavevector with $|\boldsymbol{\xi}| = \xi$ ($\hat{\boldsymbol{\xi}} = \boldsymbol{\xi}/\xi$). All the equations in the LC phase is solved using a pseudo-spectral method, with the time integration being evaluated using the 4-th order Runge-Kutta method. For all simulations performed in this study, we choose the computation parameters as: $\Omega_f = 2 \times 2$, $h = \frac{1}{128}$, $\Delta t = 10^{-5} - 10^{-4}$, $Pe = 0.1 - 10$, $Pe_t = 10 - 100$, $Er = 1 - 10$, $\zeta = 0 - 10$, $\beta = 0.0005 - 0.005$, $N_s = 32$, $L = 1$, $A = 0.05$, $k = 2\pi$, $\omega = 2\pi$, $\sigma_b = 0.005 - 0.5$, $\sigma_s = 3000\sigma_b$.

As the examples of time-dependent velocity components shown in Fig. 4.1(a-c), we have verified the numerical results by performing convergence tests for a parallel moving swimmer. As shown in Fig. 4.2, we have performed another benchmark study for the undulatory swimming motions in an Oldroyd-B (OB) fluid where the dimensionless Deborah (De) number, playing the similar role as Pe in the LC cases, is defined as the wave frequency by the OB fluid relaxation time. We measured the mean C.O.M. swimming speed U_{OB} of the swimmer that has a long body length $L = 4$, and compared the speed ratio with the numerical data by Salazar *et al.* [96] and the asymptotic results for Taylor's swimming sheet by Lauga [97]

$$\frac{U_{OB}}{U_N} = \frac{1 + \frac{\eta_s}{\eta_s + \eta_p} De^2}{1 + De^2}, \quad (4.17)$$

where η_s and η_p respectively represent the solvent and polymer contribution to the viscosity. The Newtonian speed U_N can be derived as

$$U_N = \frac{1}{2} \left(\frac{\omega}{k} \right) (Ak)^2 + O(Ak)^4 \quad (4.18)$$

where $k = 2\pi$ is the wavenumber. We find our results agree well with the previous studies.

In the third test, we have examined the impact of varying bending stiffness σ_b when choosing high values. As shown in Fig. 4.3 for the time-dependent velocity, only small differences are seen when σ_b goes beyond 0.5. In these scenarios, the swimmer can quickly respond to the imposed target curvature, and well follow the traveling-wave actuation. Hence, in the main text, we choose $\sigma_b = 0.5$ for the cases of a stiff swimmer.

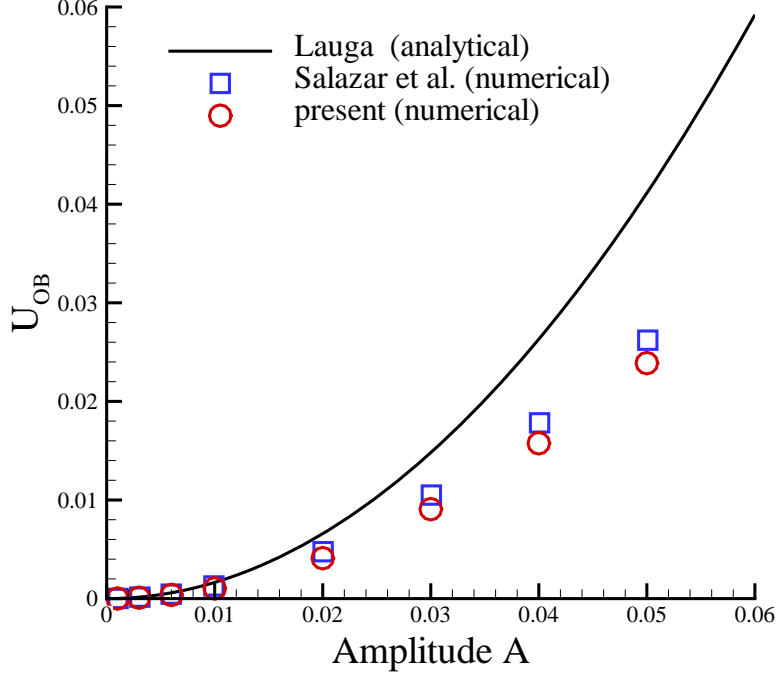


Figure 4.2: Time-averaged C.O.M. speed U_{OB} for undulatory swimming motion in an Oldroyd-B fluid. These parameters are fixed: $\Omega_f = 8 \times 8$, $h = 1/64$, $N_s = 64$, $\eta_p/\eta_s = 1/2$, $L = 4$, $De = 1$, and $\Delta t = 2.5 \times 10^{-4}$.

4.5 Asymptotic analysis

In the moving frame of the swimmer, we consider the vertical displacement of an infinitely-long wavy sheet with the described traveling-wave motion $y(x, t) = A \sin(kx - \omega t)$. When choosing $1/k$ the length scale, $1/\omega$ the time scale, and ω/k the velocity scale, the dimensionless form can be written as $y(x, t) = \varepsilon \sin(x - t)$. Here we assume a small amplitude $\varepsilon = Ak \ll 1$. Following Ref[97], we adopt a streamfunction $\varphi(x, y, t)$, and hence the velocity components can be computed as $u_x = \partial\varphi/\partial y$, $u_y = -\partial\varphi/\partial x$ with the incompressibility condition being satisfied. The boundary conditions for $\varphi(x, y, t)$ arise from conditions at infinity and on the undulatory sheet with a steady speed $-U_{LC}\hat{\mathbf{e}}_x$. Then the far-field condition at $y = \infty$ reads

$$\nabla\varphi|_{(x,\infty)} = U_{LC}\hat{\mathbf{e}}_y. \quad (4.19)$$

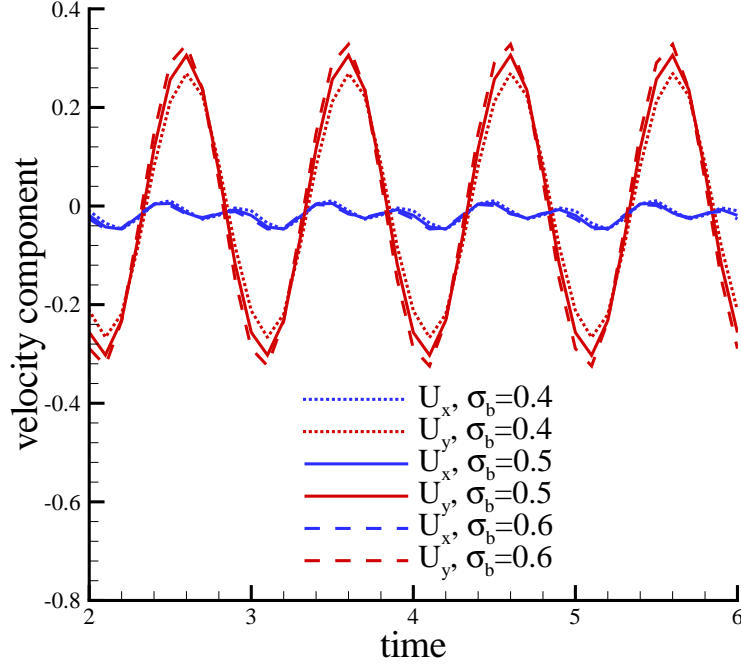


Figure 4.3: The time-dependent C.O.M. velocity $\mathbf{U}(U_x, U_y)$ for a parallel moving swimmer when choosing different values of bending stiffness σ_b . These parameters are fixed: $\Omega_f = 2 \times 2$, $\Delta t = 6.25 \times 10^{-4}$, $h = 1/128$, $Pe = 10$, $Pe_t = 100$, $Er = 1$, $\beta = 0.005$, $\zeta = 8$, $L = 1$, $N_s = 32$, $A = 0.05$, $k = 2\pi$, $\omega = 2\pi$, $\sigma_s = 1500$.

On the swimming sheet, the no-slip velocity condition is imposed as

$$\nabla \varphi|_{(x, \varepsilon \sin(x-t))} = \varepsilon \cos(x-t) \hat{\mathbf{e}}_x. \quad (4.20)$$

Recalling the forced Stokes equation

$$\nabla p = \Delta \mathbf{u} + Er \nabla \cdot \boldsymbol{\tau}_p, \quad (4.21)$$

where polymer stress, when neglecting β ($\beta \approx 0$), is given as

$$\boldsymbol{\tau}_p = \left(\mathbf{D} - \frac{\mathbf{I}}{2} \right) - \zeta (\mathbf{D} \cdot \mathbf{D} - \mathbf{D} : \mathbf{S}). \quad (4.22)$$

And the \mathbf{D} evolution equation in the LC phase

$$\begin{cases} \frac{\partial \mathbf{D}}{\partial t} + \mathbf{u} \cdot \nabla \mathbf{D} - (\mathbf{D} \cdot \nabla \mathbf{u} + \nabla \mathbf{u}^T \cdot \mathbf{D}) + 2\mathbf{E} : \mathbf{S} \\ = -\frac{1}{Pe} \left(\mathbf{D} - \frac{\mathbf{I}}{2} \right) + \frac{\zeta}{Pe} (\mathbf{D} \cdot \mathbf{D} - \mathbf{D} : \mathbf{S}) \end{cases} \quad (4.23)$$

When applying the curl on the both sides of Eq. (4.21), we have

$$\nabla \times (\nabla \cdot \boldsymbol{\tau}_p) = \frac{1}{E_r} \nabla^4 \varphi \quad (4.24)$$

Next, we expand all the variables with ε to the second order, i.e.,

$$\varphi = \varepsilon \varphi^{(1)} + \varepsilon^2 \varphi^{(2)} + O(\varepsilon^3), \quad (4.25)$$

$$\boldsymbol{\tau} = \boldsymbol{\tau}^{(0)} + \varepsilon \boldsymbol{\tau}^{(1)} + \varepsilon^2 \boldsymbol{\tau}^{(2)} + O(\varepsilon^3), \quad (4.26)$$

$$\mathbf{D} = \mathbf{D}^{(0)} + \varepsilon \mathbf{D}^{(1)} + \varepsilon^2 \mathbf{D}^{(2)} + O(\varepsilon^3), \quad (4.27)$$

$$U_{LC} = \varepsilon U_{LC}^{(1)} + \varepsilon^2 U_{LC}^{(2)} + O(\varepsilon^3). \quad (4.28)$$

After some manipulations, we can derive the following governing equations:

0th-order:

$$\begin{aligned} \frac{\partial \mathbf{D}^{(0)}}{\partial t} + \mathbf{u}^{(0)} \cdot \nabla \mathbf{D}^{(0)} - \left(\mathbf{D}^{(0)} \cdot \nabla \mathbf{u}^{(0)} + \nabla \mathbf{u}^{(0)T} \cdot \mathbf{D}^{(0)} \right) + 2\mathbf{E}^{(0)} : \mathbf{S}^{(0)} = \\ -\frac{1}{Pe} \left(\mathbf{D}^{(0)} - \frac{\mathbf{I}}{2} \right) + \frac{\zeta}{Pe} (\mathbf{D}^{(0)} \cdot \mathbf{D}^{(0)} - \mathbf{D}^{(0)} : \mathbf{S}^{(0)}), \end{aligned} \quad (4.29)$$

$$\boldsymbol{\tau}_p^{(0)} = \left(\mathbf{D}^{(0)} - \frac{\mathbf{I}}{2} \right) - \zeta (\mathbf{D}^{(0)} \cdot \mathbf{D}^{(0)} - \mathbf{D}^{(0)} : \mathbf{S}^{(0)}). \quad (4.30)$$

1st-order:

$$\begin{aligned} \frac{\partial \mathbf{D}^{(1)}}{\partial t} + \mathbf{u}^{(0)} \cdot \nabla \mathbf{D}^{(1)} + \mathbf{D}^{(1)} \cdot \nabla \mathbf{D}^{(0)} \\ - \left(\mathbf{D}^{(0)} \cdot \nabla \mathbf{u}^{(1)} + \mathbf{D}^{(1)} \cdot \nabla \mathbf{u}^{(0)} + \nabla \mathbf{u}^{(0)T} \cdot \mathbf{D}^{(1)} + \nabla \mathbf{u}^{(1)T} \cdot \mathbf{D}^{(0)} \right) \\ + 2 \left(\mathbf{E}^{(0)} : \mathbf{S}^{(1)} + \mathbf{E}^{(1)} : \mathbf{S}^{(0)} \right) \\ = -\frac{1}{Pe} \mathbf{D}^{(1)} + \frac{\zeta}{Pe} \left(\mathbf{D}^{(0)} \cdot \mathbf{D}^{(1)} + \mathbf{D}^{(1)} \cdot \mathbf{D}^{(0)} - \mathbf{D}^{(0)} : \mathbf{S}^{(1)} - \mathbf{D}^{(1)} : \mathbf{S}^{(0)} \right), \end{aligned} \quad (4.31)$$

$$\boldsymbol{\tau}_p^{(1)} = \mathbf{D}^{(1)} - \zeta (\mathbf{D}^{(0)} \cdot \mathbf{D}^{(1)} + \mathbf{D}^{(1)} \cdot \mathbf{D}^{(0)} - \mathbf{D}^{(0)} : \mathbf{S}^{(1)} - \mathbf{D}^{(1)} : \mathbf{S}^{(0)}). \quad (4.32)$$

2nd-order:

$$\begin{aligned}
& \frac{\partial \mathbf{D}^{(2)}}{\partial t} + \mathbf{u}^{(0)} \cdot \nabla \mathbf{D}^{(2)} + \mathbf{u}^{(1)} \cdot \nabla \mathbf{D}^{(1)} + \mathbf{u}^{(2)} \cdot \nabla \mathbf{D}^{(0)} \\
& - \left(\mathbf{D}^{(0)} \cdot \nabla \mathbf{u}^{(2)} + \mathbf{D}^{(1)} \cdot \nabla \mathbf{u}^{(1)} + \mathbf{D}^{(2)} \cdot \nabla \mathbf{u}^{(0)} + \nabla \mathbf{u}^{(0)T} \cdot \mathbf{D}^{(2)} \right) \\
& - \left(\nabla \mathbf{u}^{(1)T} \cdot \mathbf{D}^{(1)} + \nabla \mathbf{u}^{(2)T} \cdot \mathbf{D}^{(0)} \right) + 2 \left(\mathbf{E}^{(0)} : \mathbf{S}^{(2)} + \mathbf{E}^{(1)} : \mathbf{S}^{(1)} + \mathbf{E}^{(2)} : \mathbf{S}^{(0)} \right) \\
& = -\frac{1}{Pe} \mathbf{D}^{(2)} + \frac{\zeta}{Pe} \left(\mathbf{D}^{(0)} \cdot \mathbf{D}^{(2)} + \mathbf{D}^{(1)} \cdot \mathbf{D}^{(1)} + \mathbf{D}^{(2)} \cdot \mathbf{D}^{(0)} \right) \\
& - \frac{\zeta}{Pe} \left(\mathbf{D}^{(0)} : \mathbf{S}^{(2)} + \mathbf{D}^{(1)} : \mathbf{S}^{(1)} + \mathbf{D}^{(2)} : \mathbf{S}^{(0)} \right), \tag{4.33}
\end{aligned}$$

$$\begin{aligned}
& \boldsymbol{\tau}_p^{(2)} = \mathbf{D}^{(2)} \\
& -\zeta \left(\mathbf{D}^{(0)} \cdot \mathbf{D}^{(2)} + \mathbf{D}^{(1)} \cdot \mathbf{D}^{(1)} + \mathbf{D}^{(2)} \cdot \mathbf{D}^{(0)} - \mathbf{D}^{(0)} : \mathbf{S}^{(2)} \right) \tag{4.34} \\
& -\zeta \left(\mathbf{D}^{(1)} : \mathbf{S}^{(1)} + \mathbf{D}^{(2)} : \mathbf{S}^{(0)} \right).
\end{aligned}$$

At the 0th-order, we can solve for homogeneous solutions. Now the boundary conditions at the 1st-order become:

$$\nabla \varphi^{(1)} \Big|_{(x,\infty)} = U_{LC}^{(1)} \hat{\mathbf{e}}_y \tag{4.35}$$

$$\nabla \varphi^{(1)} \Big|_{(x,0)} = \cos(x-t) \hat{\mathbf{e}}_x \tag{4.36}$$

Note that in the above, instead of being satisfied exactly along the wavy body, the no-slip boundary condition is projected onto the x -axis, i.e., at $y = 0$. And at the 2nd-order, they take the form

$$\nabla \varphi^{(2)} \Big|_{(x,\infty)} = U_{LC}^{(2)} \hat{\mathbf{e}}_y \tag{4.37}$$

$$\nabla \varphi^{(2)} \Big|_{(x,0)} = -\sin(x-t) \nabla \left(\frac{\partial \varphi^{(1)}}{\partial y} \right) \Big|_{(x,0)}. \tag{4.38}$$

4.5.1 Isotropic cases

In the isotropic regime where $0 \leq \zeta < \zeta_c$, we close the 4th-moment tensor \mathbf{S} by expanding the PDF near the isotropy (i.e., $\Psi \rightarrow \frac{1}{2\pi}$ in the limit of random

configuration) via

$$\Psi = \frac{1}{2\pi} + \frac{2}{\pi} \left(\mathbf{p}\mathbf{p} - \frac{\mathbf{I}}{2} \right) : \mathbf{D}, \quad (4.39)$$

which leads to

$$\begin{aligned} S_{ijkl} = & -\frac{1}{24} (\delta_{ij}\delta_{kl} + \delta_{ik}\delta_{jl} + \delta_{il}\delta_{jk}) \\ & + \frac{1}{6} (\delta_{ij}D_{kl} + \delta_{ik}D_{jl} + \delta_{il}D_{jk} + \delta_{jk}D_{il} + \delta_{jl}D_{ik} + \delta_{kl}D_{ij}). \end{aligned} \quad (4.40)$$

At the $0th$ -order, we obtain $\mathbf{u}^{(0)} = 0$, $\boldsymbol{\tau}_p^{(0)} = 0$, and $\mathbf{D}^{(0)} = \text{diag}(\frac{1}{2}, \frac{1}{2})$. At the $1st$ -order, we substituting $\mathbf{D}^{(0)}$ into Eq. (4.32) and obtain

$$\boldsymbol{\tau}_p^{(1)} = (1 - \zeta/4)\mathbf{D}^{(1)}. \quad (4.41)$$

When substitute Eq. (4.41) into Eq. (4.31), we can get

$$\frac{1}{1 - \zeta/4} \frac{\partial \boldsymbol{\tau}_p^{(1)}}{\partial t} = -\frac{1}{Pe} \boldsymbol{\tau}_p^{(1)} + \frac{1}{2} \mathbf{E}^{(1)}. \quad (4.42)$$

Then we first take the divergence and then apply the curl on the both sides of Eq. (4.42) to obtain

$$\left[\frac{4}{E_r(4 - \zeta)} \frac{\partial}{\partial t} + \left(\frac{1}{E_r Pe} + \frac{1}{4} \right) \right] \nabla^4 \varphi^{(1)} = 0 \quad (4.43)$$

Given the boundary conditions in Eqs. (4.35-4.36), it is straightforward to solve for the $1st$ -order solutions as:

$$\varphi^{(1)}(x, y, t) = (1 + y)e^{-y} \sin(x - t), \quad (4.44)$$

$$U_{LC}^{(1)} = 0. \quad (4.45)$$

Next, at the $2nd$ -order, we first evaluate Eq.(4.34) to obtain

$$\boldsymbol{\tau}_p^{(2)} = \left(1 - \frac{\zeta}{4}\right)\mathbf{D}^{(2)} - \zeta(\mathbf{D}^{(1)} \cdot \mathbf{D}^{(1)} - \mathbf{D}^{(1)} : \mathbf{S}^{(1)}) \quad (4.46)$$

The Eq. (4.33) can be rewritten as

$$\begin{aligned} \frac{1}{1 - \zeta/4} \frac{\partial \boldsymbol{\tau}_p^{(2)}}{\partial t} + \frac{1}{Pe} \boldsymbol{\tau}_p^{(2)} - \frac{1}{2} \mathbf{E}^{(2)} = & -2\mathbf{E}^{(1)} : \mathbf{S}^{(1)} - \mathbf{u}^{(1)} \cdot \nabla \mathbf{D}^{(1)} \\ & - \left(\mathbf{D}^{(1)} \cdot \nabla \mathbf{u}^{(1)} + \nabla \mathbf{u}^{(1)T} \cdot \mathbf{D}^{(1)} \right) - \frac{\zeta}{1 - \zeta/4} \frac{\partial (\mathbf{D}^{(1)} \cdot \mathbf{D}^{(1)} - \mathbf{D}^{(1)} : \mathbf{S}^{(1)})}{\partial t}, \end{aligned}$$

which allows us to derive the equation for $\varphi^{(2)}$ as

$$\left[\frac{4}{E_r(4-\zeta)} \frac{\partial}{\partial t} + \left(\frac{1}{E_r Pe} + \frac{1}{4} \right) \right] \nabla^4 \varphi^{(2)} = \nabla \times \left\{ \nabla \cdot [-2\mathbf{E}^{(1)} : \mathbf{S}^{(1)} - \mathbf{u}^{(1)} \cdot \nabla \mathbf{D}^{(1)} - \left(\mathbf{D}^{(1)} \cdot \nabla \mathbf{u}^{(1)} + \nabla \mathbf{u}^{(1)T} \cdot \mathbf{D}^{(1)} \right) - \frac{\zeta}{1-\zeta/4} \frac{\partial (\mathbf{D}^{(1)} \cdot \mathbf{D}^{(1)} - \mathbf{D}^{(1)} : \mathbf{S}^{(1)})}{\partial t}] \right\} \quad (4.47)$$

Note that to solve for mean speed U_{LC} , it doesn't require that we obtain the time-dependent solution of Eq. (4.47). Instead, we can perform the time averaging (" $\langle \rangle$ ") as the following:

$$\left(\frac{1}{E_r Pe} + \frac{1}{4} \right) \nabla^4 \langle \varphi^{(2)} \rangle = \frac{4Pe^2}{(4-\zeta)^2 + 16Pe^2} (8y^2 - 24y + 8) e^{-2y} \quad (4.48)$$

with boundary conditions in Eqs. (4.37-4.38) becoming

$$\frac{\partial \langle \varphi^{(2)} \rangle}{\partial y}(\infty) = U_{LC}^{(2)}, \quad (4.49)$$

$$\frac{\partial \langle \varphi^{(2)} \rangle}{\partial y}(0) = \frac{1}{2}. \quad (4.50)$$

We can obtain

$$\frac{d}{dy} \langle \varphi^{(2)} \rangle(x, y) = a_0 \left(-y^2 + \frac{1}{2} \right) e^{-2y} + \left(\frac{1}{2} - \frac{1}{2} a_0 \right) \quad (4.51)$$

where $a_0 = \frac{E_r Pe}{4 + E_r Pe} \frac{16Pe^2}{(4-\zeta)^2 + 16Pe^2}$. So we can evaluate the mean swimming speed at the $2nd$ -order as

$$\frac{U_{LC}}{U_N} = \frac{U_{LC}^{(2)}}{U_N^{(2)}} = 1 - \frac{16E_r Pe^3}{(4 + E_r Pe) [(4-\zeta)^2 + 16Pe^2]} \quad (4.52)$$

where $U_N = U_N^{(2)} \varepsilon^2 = 1/2 \varepsilon^2$ is the swimming velocity in a Newtonian fluid. Note that in Doi's theory, the LC polymer contribution to the zero-shear-rate viscosity can be effectively defined as [98]

$$\frac{\mu_p}{\mu_f} = \alpha(S) E_r Pe \quad (4.53)$$

where $S = \sqrt{(2\mathbf{D} : \mathbf{D} - 1)/2}$ is the order parameter, $\alpha(S)$ is a concentration coefficient, and μ_p represents the polymer contribution to the viscosity. Hence, when $\zeta = 0$, we estimate $S = 0$ and $\alpha(S) = 1$, leading to

$$\frac{U_{LC}}{U_N} = \frac{1 + \left(\frac{\mu_f}{\mu_f + \mu_p/4}\right) Pe^2}{1 + Pe^2}. \quad (4.54)$$

4.5.2 Nearly-aligned cases

In the nematic regime, we adopt a classical quadratic closure to approximate \mathbf{S} [29] as

$$\mathbf{S} = \mathbf{D}\mathbf{D}, \quad (4.55)$$

corresponding to the strong alignment configuration with large ζ values when $\zeta > \zeta_c$. At the 0th-order, we solve the steady-state equation for $\mathbf{D}^{(0)} = \text{diag}\left(D_{11}^{(0)}, 1 - D_{11}^{(0)}\right)$ via

$$\zeta \left\{ D_{11}^{(0)2} - \left[D_{11}^{(0)2} + \left(1 - D_{11}^{(0)}\right)^2 \right] D_{11}^{(0)} \right\} - \left(D_{11}^{(0)} - \frac{1}{2} \right) = 0, \quad (4.56)$$

which yields two equilibrium solution. One takes the form

$$D_{11}^{(0)} = \frac{\zeta + \sqrt{\zeta^2 - 2\zeta}}{2\zeta} > \frac{1}{2}. \quad (4.57)$$

This solution represents that the LC's principal alignment direction is aligned with the x -axis. When fixing the swimmer's moving direction to be horizontal, the above solution corresponds to the parallel swimming cases. Another solution is

$$D_{11}^{(0)} = \frac{\zeta - \sqrt{\zeta^2 - 2\zeta}}{2\zeta} < \frac{1}{2}, \quad (4.58)$$

meaning the principal alignment direction of LC is along the y -axis. Hence, this solution corresponds to the swimming direction is perpendicular to the LC's alignment direction.

At the 1st-order, it is straightforward to show that

$$\boldsymbol{\tau}_p^{(1)} = (\zeta - 2)D_{11}^{(1)} \begin{pmatrix} 1 & 0 \\ 0 & -1 \end{pmatrix}. \quad (4.59)$$

Substituting Eq. (4.59) into Eq. (4.31), we have

$$\begin{cases} \frac{1}{\zeta-2} \frac{\partial \tau_{p,11}^{(1)}}{\partial t} + 4 \left(D_{11}^{(0)} - 1 \right) D_{11}^{(0)} E_{11}^{(1)} + \frac{1}{Pe} \tau_{p,11}^{(1)} = 0 \\ \frac{1}{\zeta-2} \frac{\partial \tau_{p,22}^{(1)}}{\partial t} - 4 \left(D_{11}^{(0)} - 1 \right) D_{11}^{(0)} E_{11}^{(1)} + \frac{1}{Pe} \tau_{p,22}^{(1)} = 0 \end{cases} \quad (4.60)$$

Applying the same trick in Eq. (4.24), we can further derive

$$\left(\frac{1}{\zeta-2} \frac{1}{E_r} \frac{\partial}{\partial t} + \frac{1}{E_r Pe} \right) \nabla^4 \varphi^{(1)} + \frac{4}{\zeta} \frac{\partial^4 \varphi^{(1)}}{\partial x^2 \partial y^2} = 0 \quad (4.61)$$

To facilitate further analytical manipulations, we consider the strong alignment cases when ζ is large ($\zeta \gg 1$), which allows us to neglect the second term, and obtain the same 1st-order solution as Eq. (4.44).

At the 2nd-order, using the equilibrium solutions of $\mathbf{D}^{(0)}$, we can show that

$$\begin{aligned} \boldsymbol{\tau}_p^{(2)} = & [(\zeta - 2)D_{11}^{(2)} + \zeta(3D_{11}^{(1)2} + D_{12}^{(1)2})(2D_{11}^{(0)} - 1)] \begin{pmatrix} 1 & 0 \\ 0 & -1 \end{pmatrix} \\ & + 2\zeta D_{11}^{(1)} D_{12}^{(1)} (2D_{11}^{(0)} - 1) \begin{pmatrix} 0 & 1 \\ 1 & 0 \end{pmatrix}, \end{aligned} \quad (4.62)$$

which lead to

$$\begin{cases} \frac{1}{\zeta-2} \frac{\partial}{\partial t} \left[\tau_{p,11}^{(2)} - \zeta \left(3D_{11}^{(1)2} + D_{12}^{(1)2} \right) \left(2D_{11}^{(0)} - 1 \right) \right] + G_{11} + \frac{1}{Pe} \tau_{p,11}^{(2)} = 0 \\ \frac{1}{\zeta-2} \frac{\partial}{\partial t} \left[\tau_{p,22}^{(2)} + \zeta \left(3D_{11}^{(1)2} + D_{12}^{(1)2} \right) \left(2D_{11}^{(0)} - 1 \right) \right] + G_{22} + \frac{1}{Pe} \tau_{p,22}^{(2)} = 0 \end{cases} \quad (4.63)$$

where

$$\begin{aligned} \mathbf{G} = & \mathbf{u}^{(1)} \cdot \nabla \mathbf{D}^{(1)} \\ & - \left(\mathbf{D}^{(0)} \cdot \nabla \mathbf{u}^{(2)} + \mathbf{D}^{(1)} \cdot \nabla \mathbf{u}^{(1)} + \nabla \mathbf{u}^{(1)\text{T}} \cdot \mathbf{D}^{(1)} + \nabla \mathbf{u}^{(2)\text{T}} \cdot \mathbf{D}^{(0)} \right) \\ & + 2 \left(\mathbf{E}^{(1)} : \mathbf{S}^{(1)} + \mathbf{E}^{(2)} : \mathbf{S}^{(0)} \right). \end{aligned}$$

In the end, we can derive the linear equation for $\varphi^{(2)}$ as

$$\begin{aligned} & \frac{1}{\zeta-2} \frac{\partial}{\partial t} \left[\frac{1}{E_r} \nabla^4 \varphi^{(2)} + 2 \frac{\partial^2 \left(\zeta \left(3D_{11}^{(1)2} + D_{12}^{(1)2} \right) (2D_{11}^{(0)} - 1) \right)}{\partial x \partial y} \right] + \frac{1}{E_r P e} \nabla^4 \varphi^{(2)} + \frac{\partial^2 (G_{22} - G_{11})}{\partial x \partial y} \\ & = \left(\frac{1}{\zeta-2} \frac{\partial}{\partial t} + \frac{1}{P e} \right) \left(\frac{\partial^2}{\partial x^2} - \frac{\partial^2}{\partial y^2} \right) \left[2\zeta D_{11}^{(1)} D_{12}^{(1)} (2D_{11}^{(0)} - 1) \right] \end{aligned} \quad (4.64)$$

Similar to the isotropic case, here we take the time averaging of Eq. (4.64) to obtain

$$\begin{aligned} & \frac{1}{E_r P e} \nabla^4 \langle \varphi^{(2)} \rangle = \\ & \frac{2(\zeta-2)}{P e^2 + (\zeta-2)^2} (2D_{11}^{(0)} - 1) \left[4y^2 + (8D_{11}^{(0)} - 12)y - (8D_{11}^{(0)} - 6) \right] e^{-2y}. \end{aligned} \quad (4.65)$$

When applying the boundary conditions (4.37-4.38), we obtain

$$\frac{d}{dy} \langle \varphi^{(2)} \rangle (x, y) = -\frac{a_1}{2} \left(y^2 + 2D_{11}^{(0)} y + D_{11}^{(0)} \right) e^{-2y} + \left(\frac{1}{2} + \frac{a_1 D_{11}^{(0)}}{2} \right) \quad (4.66)$$

where $a_1 = E_r P e \frac{2(\zeta-2)}{(\zeta-2)^2 + P e^2} (2D_{11}^{(0)} - 1)$. So we can eventually solve for the speed ratio at the $2nd$ -order as

$$\frac{U_{LC}}{U_N} = 1 + \frac{4E_r P e (\zeta - 2)}{(\zeta - 2)^2 + P e^2} \left(D_{11}^{(0)} - \frac{1}{2} \right) D_{11}^{(0)} \quad (4.67)$$

4.6 Results and Discussion

Without the swimmer, the pure LC phase is described by a homogeneous distribution of $\mathbf{D}_0 = \int_p \mathbf{p} \mathbf{p} \Psi_0 d\mathbf{p}$, i.e., obtained from taking the configurational

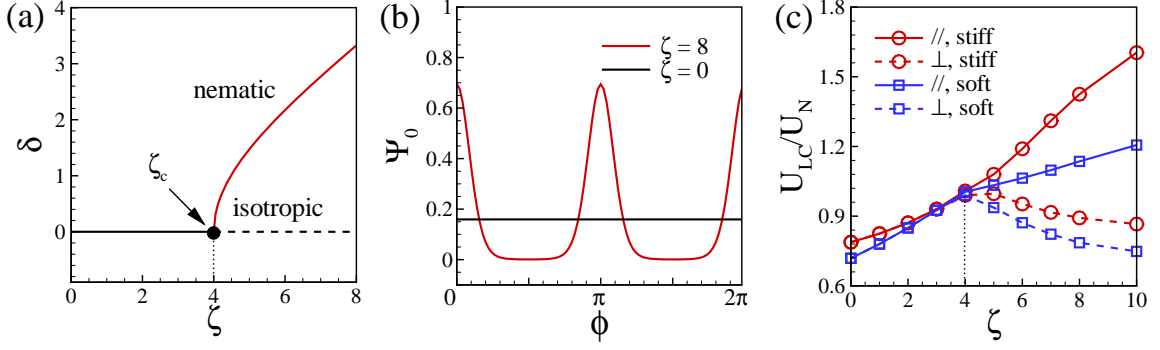


Figure 4.4: I-N phase transition led anisotropic swimming. (a) δ as a function of ζ , with the bifurcation occurring at $\zeta_c = 4$. (b) Constant and apolar distribution of $\Psi_0(\phi)$ at $\zeta = 0$ and 8. (c) U_{LC}/U_N as a function of ζ for stiff ($\sigma_b = 0.5$) and soft ($\sigma_b = 0.005$) swimmer when choosing $Pe = 1$ and $Er = 10$, for the parallel (denoted by “//”) and perpendicular (denoted by “ \perp ”) motions.

average of the equilibrium solution of the original Doi’s kinetic model:

$$\Psi_0 = \frac{\exp[\delta \cos(2\phi)]}{\int_0^{2\pi} d\phi' \exp[\delta \cos(2\phi')]}, \quad \delta = \frac{\zeta \int_0^{2\pi} d\phi' \cos(2\phi') \exp[\delta \cos(2\phi')]}{4 \int_0^{2\pi} d\phi' \exp[\delta \cos(2\phi')]}.$$
(4.68)

As shown in Fig. 1(a), $\delta(\zeta)$ admits a bifurcation at $\zeta_c = 4$, and has two solution branches for the (I)sotropic and (N)ematic states. In Fig. 4.4(b), the symmetric form of $\Psi_0(\phi)$ suggests that the rod’s primary (or principal) orientation direction is aligned with the x -axis when $\phi = 0$ and ϕ in the nematic regime ($\zeta \geq \zeta_c$), compared to the constant solution in the isotropic regime ($0 \leq \zeta < \zeta_c$). At each time step in simulation, we reconstruct Ψ_0 from the \mathbf{D} field, and then approximate $\mathbf{S}(\mathbf{x}, t) \approx \int_p \mathbf{p} \mathbf{p} \mathbf{p} \mathbf{p} \Psi_0 d\mathbf{p}$ following a quasi-equilibrium *ansatz* that \mathbf{D} and \mathbf{S} co-align in principal directions in the eigenspace. This method is also referred to as the Bingham closure ([33, 76]), which has proven to be accurate in PDF reconstruction, and has been widely used in simulating both equilibrium and non-equilibrium LCs ([76, 99, 100]).

When there are microswimmers moving in a LC, curiously, one may ask

how do they mechanically respond to this anisotropic polymer fluid? To answer this question, we consider undulatory swimming motions either parallel with or perpendicular to LC alignment direction (i.e., x -direction), for both the “stiff” ($\sigma_b = 0.5$) and “soft” ($\sigma_b = 0.005$) swimmers. When we impose traveling waves that are moving rightward, the swimmer produces leftward undulatory motions. We measure the mean C.O.M. velocity U_{LC} by performing time averaging over five undulation periods after the swimming speed reaches quasi-steady states, and compare with that for the Newtonian speed U_N . As shown in Fig. 4.4(c), the speed ratio U_{LC}/U_N as a function of ζ clearly show non-Newtonian behaviors, especially in the nematic regime where similar bifurcations occur, corresponding the motions that are parallel (denoted by symbol “//”) and perpendicular (denoted by symbol “ \perp ”) to the x -axis. More specifically, we observe enhanced swimming speeds when the swimmer moves parallel in the nematic regime; while retarded motions are seen in the isotropic regime, and in the most nematic regime during perpendicular motions. Also, while qualitatively similar behaviors are consistently observed for the stiff and soft cases in the parameter space, it is seen that the stiff swimmer can generally achieve faster mean speeds, exhibiting more significant speed gain and loss.

Figures 4.5(a-c) show the variations of U_{LC}/U_N with respect to Pe when fixing Er . When Pe is small, which corresponds to a slow undulation (or equivalently, quick rotational diffusion of LC molecules), U_{LC}/U_N is close to 1, suggesting Newtonian-like behaviors. This is because when $Pe \rightarrow 0$, the Brownian diffusion in the LC phase dominates over convection, which not only

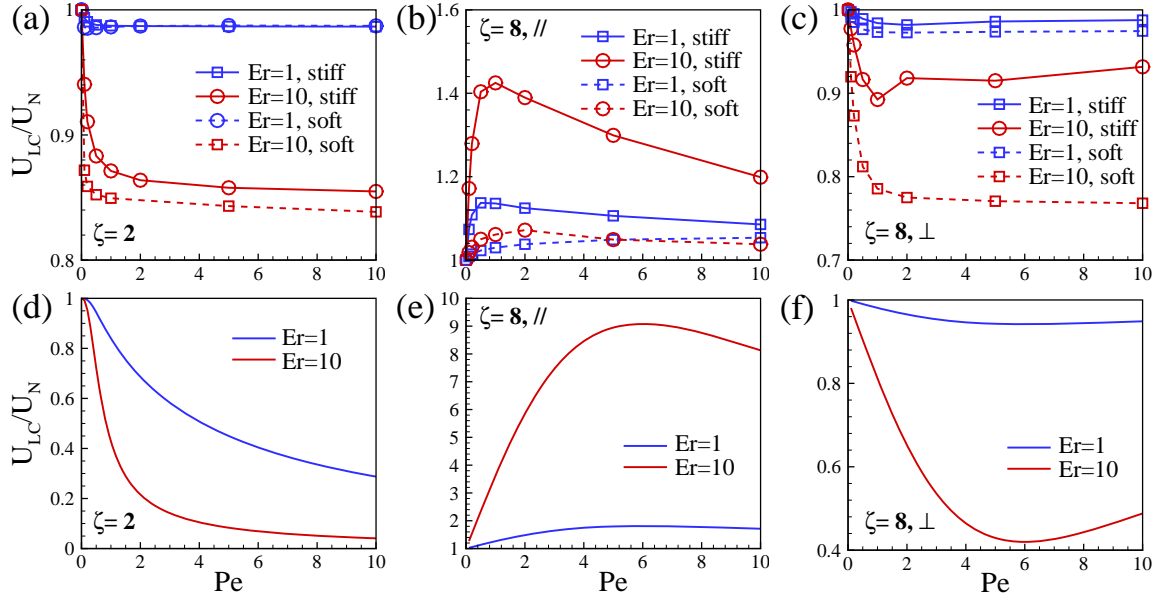


Figure 4.5: Speed ratio U_{LC}/U_N as a function of Pe at $Er = 1$ and 10 obtained from numerical simulation (a-c) and asymptotic solutions (d-f).

drives the LC structure towards equilibrium states (i.e., the R.H.S. of Eq. (4.9) is approximately 0.) but also produces smaller and smaller τ_p . On the other hand, at a high Pe where convection dominates during fast acutation, the LC's configuration is modulated by flow via constraining stress, i.e., $\mathbf{E} : \mathbf{S}$, due to rod's rigidity, which leads to more complicated behaviors. In the isotropic regime, U_{LC}/U_N monotonically decrease. Nevertheless, in the nematic regime, U_{LC}/U_N varies non-monotonically, with the maximum (minimum) occurring at small Pe ($\sim O(1)$) during the parallel (perpendicular) swimming motions.

To understand the numerical observations, we build an idealized linear model of a one-dimensional, infinitely-long sheet prescribed with small amplitude traveling waves, i.e., the so-called Taylor's swimming sheet ([101]). Its vertical displacement can be described in the moving coordinate as $y(x, t) = \varepsilon \sin(x - t)$ with amplitude $\varepsilon \ll 1$. Then we simplify the above governing equations by employing a stream function φ to replace the

incompressible fluid velocity via $\mathbf{u} = \nabla \times (\varphi \hat{\mathbf{e}}_z)$ ($\hat{\mathbf{e}}_z$ is the unit vector denoting the out-of-plane direction). By following the solution procedure that is almost identical to [102] and [85, 88], we impose the no-slip condition on the wavy sheet, and perform asymptotic analyses by expanding all the variables in terms of ε in both the isotropic and nematic regime. Moreover, we neglect the crowding effect (i.e., $\beta = 0$) in $\boldsymbol{\tau}_p$ and the translational Brownian diffusion (i.e., $Pe_t^{-1} \rightarrow 0$), and adopt different closure methods for \mathbf{S} in the isotropic and nematic regime to facilitate derivation. After some manipulations (see more derivation details in the supplemental material), we find directional motions only occur in the second order, i.e., $U_{LC} = U_{LC}^{(2)}\varepsilon^2$, and the speed ratio can be calculated as:

$$\frac{U_{LC}}{U_N} = 1 - \frac{16E_rPe^3}{(4 + E_rPe)[(4 - \zeta)^2 + 16Pe^2]}, \quad (\text{Isotropic}) \quad (4.69)$$

$$\frac{U_{LC}}{U_N} = 1 + \frac{4E_rPe(\zeta - 2)}{(\zeta - 2)^2 + Pe^2} \left(D_{11}^{(0)} - \frac{1}{2} \right) D_{11}^{(0)}, \quad (\text{Nematic}) \quad (4.70)$$

where $D_{11}^{(0)} = \frac{\zeta \pm \sqrt{\zeta^2 - 2\zeta}}{2\zeta}$ is the diagonal component of the equilibrium solution $\mathbf{D}^{(0)} = \text{diag} \left(D_{11}^{(0)}, 1 - D_{11}^{(0)} \right)$, and the plus (minus) sign corresponds to parallel (perpendicular) swimming motion with respect to the alignment direction.

As shown in Figs. 4.5(d-f), the above asymptotic solutions predict the qualitatively similar behaviors of U_{LC}/U_N as the numerical results, and reveal different scaling behaviors. In the isotropic regime, the monotonic decay as a function of Pe at a given Er is reminiscent of the behaviors in the viscoelastic (e.g., Oldroyd-B) fluids ([102, 103]). This can be witnessed by introducing an effective polymer viscosity μ_p ([29, 89]) as $\frac{\mu_p}{\mu_f} = \alpha(S)E_rPe$, where E_rPe defines the effective polymer contribution to the zero-shear-rate viscosity, and

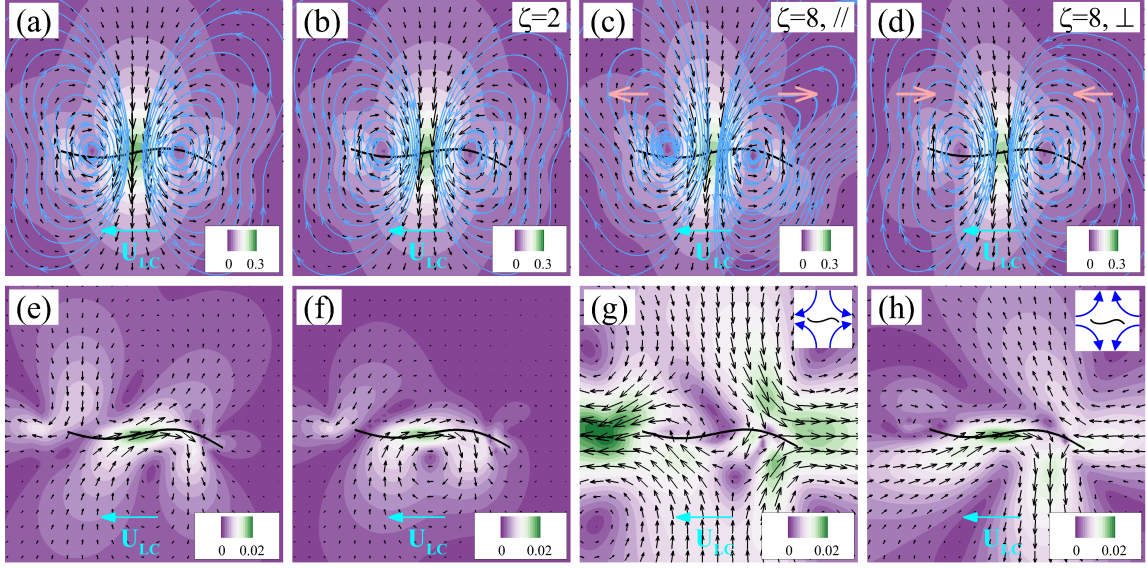


Figure 4.6: The instantaneous (a-d) and time-averaged (e-h) velocity field around a “stiff” swimmer in the body-fixed frame when choosing $\sigma_b = 0.5$, $Pe = 1$, and $Er = 10$: (a,e) Newtonian; (b,f) Isotropic, $\zeta = 2$; (c,g) Nematic and parallel, $\zeta = 8$; (d,h) Nematic and perpendicular, $\zeta = 8$. The vector field and the background color correspond to the velocity \mathbf{u} and its magnitude $|\mathbf{u}|$.

the estimated coefficient α characterizes the dependence on the order parameter S . When $\zeta \rightarrow 0$, we estimate $S \approx 0$ and $\alpha(S) \approx 1$, and hence can rewrite Eq. (4.69) as

$$\frac{U_{LC}}{U_N} = \frac{1 + \left(\frac{\mu_f}{\mu_f + \mu_p/4} \right) Pe^2}{1 + Pe^2}, \quad (\zeta \rightarrow 0) \quad (4.71)$$

resembling the asymptotic solution by [102] for Taylor’s swimming sheet in viscoelastic fluids. In the nematic regime, from Eq. (4.70), apparently the speed gain and loss are seen to be directly determined by the LC’s horizontal ($D_{11}^{(0)} > \frac{1}{2}$) and vertical ($D_{11}^{(0)} < \frac{1}{2}$) alignment direction. Moreover, in both cases, $\frac{U_{LC}}{U_N} \rightarrow 1$ in the limit of $Pe \rightarrow \infty$, suggesting diminishing non-Newtonian behaviors for very fast undulations in sharply-aligned LCs.

Next, we take a closer look at the flow patterns to uncover the nonlinear effect due to the finite length of the swimmer. As shown in Figs. 4.6(a-d), we

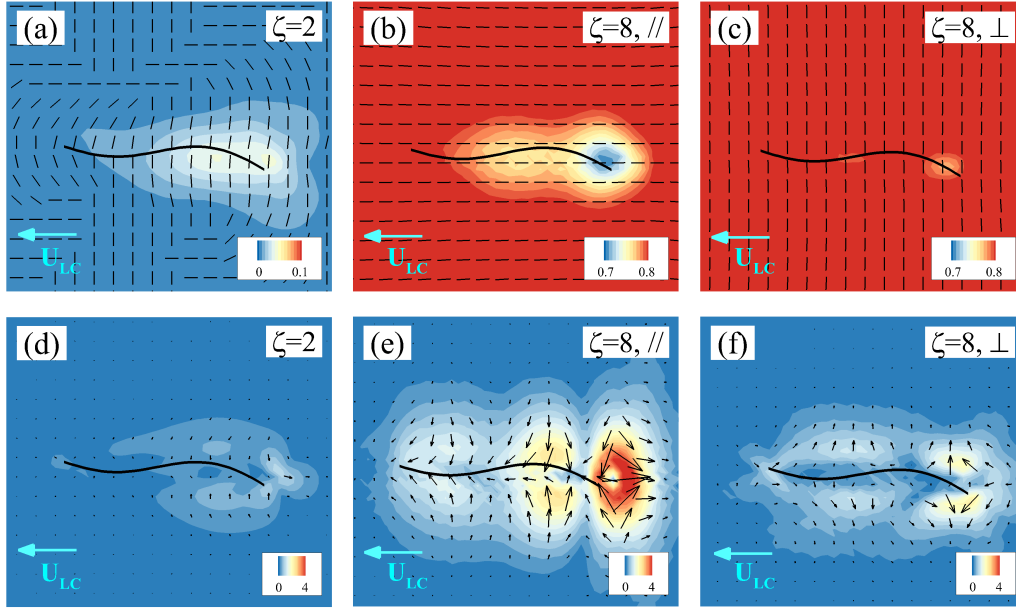


Figure 4.7: The time-averaged director and polymer force fields around a stiff swimmer corresponding to Figs. 4.6(f-h). (a-c): nematic director $\langle \mathbf{m} \rangle$ superposed on the colormap of the order parameter S . (d-f): polymer force vector $\langle \mathbf{f}_p \rangle$ superimposed on the force magnitude $|\langle \mathbf{f}_p \rangle|$.

compare the simulation results for instantaneous flow fields at the end of each period, after the time-periodic swimming motions become quasi-steady. While the isotropic ($\zeta = 2$) case in panel(b) resembles the Newtonian one in panel(a), the parallel (perpendicular) swimming case in the nematic regime in panel(c) (panel(d)) has slightly wider (narrower) circulation zones near the two ends. Indeed, when averaging over three to five periods, we consistently find the flow patterns shown in Figs. 4.6(e-h) distinctive features. Compared to the Newtonian case in panel(e), in the isotropic regime, the LC flow in panel(f), while similar, appears to be slightly weakened. More interestingly, we find that the mean flow in the nematic regime can be extensile (panel(g)) and contractile (panel(h)), corresponding to the parallel and perpendicular motions, respectively.

Figures 4.7(a-c) reveal the characteristics of the nematic field. Without

imposing particular anchoring conditions for \mathbf{D} along the wavy body, we find the time-averaged (denoted by “ $\langle \rangle$ ”) director distribution $\langle \mathbf{m} \rangle$ approximately follow the global equilibrium ordering, i.e., random (panel(a)) and aligned (panels(b,c)). But due to the finite length of the swimmer, the resultant LC structures lack left-right symmetry. The disturbances on the nematic field are concentrated in the areas around the body’s rear side without propagating further away from where strong steric interactions (i.e., characterized by large values of ζ) enforce local alignment. Also, when comparing the two scenarios in the nematic regime in panel(b) and (c), it appears that parallel motions can impact larger areas. This is because the vertical oscillations during undulation are a lot faster ($\sim 5 - 10$ times) than the resultant horizontal migration, and can lead to stronger momentum exchange along the y -direction. Hence, it is easier for the shear-induced force tends to re-orient the LC molecules perpendicularly, which leaves larger low-order zones during parallel motions.

Further examination of the time-averaged polymer force, $\langle \mathbf{f}_p \rangle = \langle \nabla \cdot \boldsymbol{\tau}_p \rangle$, in Fig. 4.7 reveal more precise propulsion mechanisms. Since the periodic elastic body force have a zero mean, i.e., $\langle \mathbf{f}_e \rangle = 0$, from Eq. (4.7), the near-body fluid flows are driven by $\langle \mathbf{f}_p \rangle$ at a finite Er . As typically shown in panel(d), isotropic LCs can only produce small $\langle \mathbf{f}_p \rangle$ without showing clear correlations with the swimming direction. In comparison, nematic LCs apparently create much stronger and left-right asymmetrical $\langle \mathbf{f}_p \rangle$ in panel(e) and (f), with the largest values at the “tail”. And they are clearly seen to be extensile and contractile, respectively, suggesting to be the driving forces of the flow patterns in Fig. 4.6(g) and (h). More intriguingly, unlike the isotropic cases,

the near-body distributions of $\langle \mathbf{f}_p \rangle$ in the nematic regime highly correlate with the swimming direction. In panel(e), the projected force vectors at $y = 0$ all approximately point leftwards to “push” the swimmer forward; while in panel (f), the projected force along the x –direction, while weaker, appears to be overall pointing rightward, and “pull” the swimmer backward. In fact, when considering more general scenarios when there are disturbances (e.g., small oscillations) occurring in nematic LCs, our results suggest anisotropic propagation of mechanical signals as the induced force transmissions are in favor of nematic alignment directions.

4.7 Conclusion

This work has built a Q –tensor model to study the nonlinear dynamics of undulatory swimming motions in LCs in the limit of vanishing Reynolds numbers. Combining direct numerical simulations and asymptotic analysis, we have revealed both enhanced and retarded swimming behaviors for a flexible swimmer moving in LC solutions which may exhibit different orientation orders. Compared to those top-down macro models of EL or Landau-de Gennes (LG) type ([32]), ours is derived bottom-up, and hence has accurate microscopic origins but fewer computation parameters. Moreover, it avoids to use any orientational derivatives, and hence does not require applying ad-hoc anchoring conditions to enforce LC molecule alignment on the boundaries or interfaces, which can significantly reduce complexity in constructing numerical algorithm and facilitate asymptotic analytical analysis. Our results suggest that besides adopting wavy body undulations to break

symmetry, it is possible for a finite-length flexible swimmer to make use of the unique near-body fluid dynamics and polymer force generation to adjust the migration speed. We expect to apply the same methodology to generally study microorganism's motion, both individually and collectively, in anisotropic complex-fluids environments.

PUBLICATION

- [1] Lin, ZW., Chen, S., and Gao, T., 2021. Q-tensor model for undulatory swimming in a liquid crystal. submitted to Journal of Fluid Mechanics.
- [2] Chen, S., Yan, W. and Gao, T., 2020. Scaling law of Brownian rotation in dense hard-rod suspensions. Physical Review E, 102(1), p.012608.
- [3] Chen, S., Gao, P. and Gao, T., 2018. Dynamics and structure of an apolar active suspension in an annulus. Journal of Fluid Mechanics, 835, p.393.
- [4] Chen, S. and Gao, T.,. Transport of an Apolar Active Suspension in a Rectangular Channel. finished

BIBLIOGRAPHY

BIBLIOGRAPHY

- [1] S. Chen, P. Gao, and T. Gao. Dynamics and structure of an apolar active suspension in annulus. *J. Fluid Mech.*, 835:393–405, 2018.
- [2] See supplementary information.
- [3] S. Ramaswamy. The mechanics and statistics of active matter. *Ann. Rev. Cond. Matt. Phys.*, 1:323–345, 2010.
- [4] M. Marchetti, J. Joanny, S. Ramaswamy, T. Liverpool, J. Prost, M. Rao, and R. Simha. Hydrodynamics of soft active matter. *Rev. Mod. Phys.*, 85:1143–1189, 2013.
- [5] M. Shelley. The dynamics of microtubule/motor-protein assemblies in biology and physics. *Annu. Rev. Fluid Mech.*, 48:487–506, 2016.
- [6] A. Sokolov, I. Aranson, J. Kessler, and R. Goldstein. Concentration dependence of the collective dynamics of swimming bacteria. *Phys. Rev. Lett.*, 98:158102, 2007.
- [7] T. Sanchez, D. Chen, S. DeCamp, M. Heymann, and Z. Dogic. Spontaneous motion in hierarchically assembled active matter. *Nature*, 491:431–434, 2012.
- [8] G. Henkin, S. J. DeCamp, D. T. N. Chen, T. Sanchez, and Z. Dogic. Tunable dynamics of microtubule-based active isotropic gels. *Phil. Trans. R. Soc. A*, 372(2029), 2014.
- [9] F. Woodhouse and R. Goldstein. Spontaneous circulation of confined active suspensions. *Phys. Rev. Lett.*, 109:168105, 2012.
- [10] M. Ravnik and J. Yeomans. Confined active nematic flow in cylindrical capillaries. *Phys. Rev. Lett.*, 110:026001, 2013.
- [11] H. Wioland, F. Woodhouse, J. Dunkel, J. Kessler, and R. Goldstein. Confinement stabilizes a bacterial suspension into a spiral vortex. *Phys. Rev. Lett.*, 110:268102, 2013.
- [12] A. Bricard, J. Caussin, N. Desreumaux, O. Dauchot, and D. Bartolo. Emergence of macroscopic directed motion in populations of motile colloids. *Nature*, 503:95–98, 2013.

- [13] B. Ezhilan and D. Saintillan. Transport of a dilute active suspension in pressure-driven channel flow. *J. Fluid Mech.*, 777:482–522, 2015.
- [14] A.C.H. Tsang and E. Kanso. Density shock waves in confined microswimmers. *Phys. Rev. Lett.*, 116:048101, 2016.
- [15] Pau Guillamat, Jordi Ignés-Mullol, and Francesc Sagués. Control of active liquid crystals with a magnetic field. *Proceedings of the National Academy of Sciences*, 113(20):5498–5502, 2016.
- [16] Pau Guillamat, Jordi Ignés-Mullol, Suraj Shankar, M Cristina Marchetti, and Francesc Sagués. Probing the shear viscosity of an active nematic film. *Physical review E*, 94(6):060602, 2016.
- [17] M. Theillard, R. Alonso-Matilla, and D. Saintillan. Geometric control of active collective motion. *Soft Matter*, 13:363–375, 2017.
- [18] K. Wu, J. Hishamunda, D. Chen, S. DeCamp, Y. Chang, A. Fernández-Nieves, S. Fraden, and Z. Dogic. Transition from turbulent to coherent flows in confined three-dimensional active fluids. *Science*, 355(6331), 2017.
- [19] T. Gao, M. Betterton, A. Jhang, and M. Shelley. Analytical structure, dynamics, and coarse-graining of a kinetic model of an active fluid. *Phys. Rev. Fluids*, 2:093302, 2017.
- [20] T. Gao and Z. Li. Self-driven droplet powered by active nematics. *Phys. Rev. Lett.*, 119:108002, 2017.
- [21] D. W. Adams and J. Errington. Bacterial cell division: assembly, maintenance and disassembly of the z ring. *Nat. Rev. Micro.*, 7:642–653, 2009.
- [22] M. Davies Wykes, J. Palacci, T. Adachi, L. Ristroph, X. Zhong, M. Ward, J. Zhang, and M. Shelley. Dynamic self-assembly of microscale rotors and swimmers. *Soft Matter*, page accepted, 2016.
- [23] E. Jewell, W. Wang, and T. Malloukl. Catalytically driven assembly of trisegmented metallic nanorods and polystyrene tracer particles. *Soft Matter*, 12:2501–2504, 2016.
- [24] D. Saintillan and M. Shelley. Active suspensions and their nonlinear models. *C. R. Phys.*, 14:497–517, 2013.
- [25] H. Wioland, E. Lushi, and R. Goldstein. Directed collective motion of bacteria under channel confinement. *New J. Phys.*, 18, 2016.

- [26] D. Saintillan and M. Shelley. Instabilities, pattern formation, and mixing in active suspensions. *Phys. Fluids*, 20:123304, 2008.
- [27] T. Gao, R. Blackwell, M. Glaser, M. Betterton, and M. Shelley. Multiscale polar theory of microtubule and motor-protein assemblies. *Phys. Rev. Lett.*, 114:048101, 2015.
- [28] C. Hohenegger and M. Shelley. *Dynamics of complex bio-fluids*. Oxford University Press, 2011.
- [29] M. Doi and S. Edwards. *The theory of polymer dynamics*, volume 73. Oxford University Press, USA, 1988.
- [30] B. Ezhilan, M. Shelley, and D. Saintillan. Instabilities and nonlinear dynamics of concentrated active suspensions. *Phys. Fluids*, 25:070607, 2013.
- [31] W. Maier and A. Saupe. Eine einfache molekulare theorie des nematischen kristallinflüssigen zustandes. *Zeit. Nat. Teil A*, 13:564, 1958.
- [32] P. G. DeGennes. *The physics of liquid crystals*. Oxford University Press, 1974.
- [33] Christopher Bingham. An antipodally symmetric distribution on the sphere. *The Annals of Statistics*, pages 1201–1225, 1974.
- [34] C. Chaubal and L. Leal. A closure approximation for liquid-crystalline polymer models based on parametric density estimation. *J. Rheol.*, 42:177–201, 1998.
- [35] T. Gao and H. H. Hu. Deformation of elastic particles in viscous shear flow. *J. Comput. Phys.*, 228:2132–2151, 2009.
- [36] H. H. Hu, M. Y. Zhu, and N. Patankar. Direct numerical simulations of fluid solid systems using the arbitrary lagrangian eulerian technique. *J. Comput. Phys.*, 169:427–462, 2001.
- [37] Sumesh P Thampi, Amin Doostmohammadi, Ramin Golestanian, and Julia M Yeomans. Intrinsic free energy in active nematics. *EPL (Europhysics Letters)*, 112(2):28004, 2015.
- [38] R. Voituriez, J. Joanny, and J. Prost. Spontaneous flow transition in active polar gels. *Europhys. Lett.*, 69:404–10, 2005.

- [39] L. Giomi, L. Mahadevan, B. Chakraborty, and M. Hagan. Excitable patterns in active nematics. *Phys. Rev. Lett.*, 106:218101, 2011.
- [40] L. Giomi, L. Mahadevan, B. Chakraborty, and M. Hagan. Banding, excitability and chaos in active nematic suspensions. *Nonlinearity*, 25(8):2245, 2012.
- [41] L. Giomi, M. Bowick, X. Ma, and M. Marchetti. Defect annihilation and proliferation in active nematics. *Phys. Rev. Lett.*, 110:228101, 2013.
- [42] S. Thampi, R. Golestanian, and J. Yeomans. Instabilities and topological defects in active nematics. *Europhys. Lett.*, 105:18001, 2014.
- [43] E. Lushi, H. Wioland, and R. Goldstein. Fluid flows generated by swimming bacteria drive self-organization in confined fluid suspensions. *Proceedings of the National Academy of Sciences*, 111:9733–9738, 2014.
- [44] T. Gao, R. Blackwell, M. Glaser, M. Betterton, and M. Shelley. Multiscale modeling and simulation of microtubule/motor protein assemblies. *Phys. Rev. E*, 92:062709, 2015.
- [45] D. Koch and G. Subramanian. Collective hydrodynamics of swimming microorganisms: living fluids. *Annu. Rev. Fluid Mech.*, 43:637–659, 2011.
- [46] D. Takagi, A. Braunschweig, J. Zhang, and M. Shelley. Dispersion of self-propelled rods undergoing fluctuation-driven flips. *Phys. Rev. Lett.*, 110:038301, 2013.
- [47] A. Kaiser, A. Peshkov, A. Sokolov, B. ten Hagen, H. Löwen, and I. Aranson. Transport powered by bacterial turbulence. *Phys. Rev. Lett.*, 112:158101, 2014.
- [48] A. Sokolov, M. Apodaca, B. Grzybowski, and I. Aranson. Swimming bacteria power microscopic gears. *Proc. Natl. Acad. Sci.*, 107:969–974, 2010.
- [49] D. Saintillan and M. Shelley. Instabilities and pattern formation in active particle suspensions: Kinetic theory and continuum simulations. *Phys. Rev. Lett.*, 100:178103, 2008.
- [50] J. Jeong and C. Jang. Slow motion of a circular cylinder in a plane poiseuille flow in a microchannel. *Phys. Fluids*, 154:123104, 2014.

- [51] A. Duarte, A. Miranda, and P. Oliveira. Numerical and analytical modeling of unsteady viscoelastic flows: The start-up and pulsating test case problems. *J. Non-Newtonian Fluid Mech.*, 154:153–169, 2008.
- [52] S. Woltman, G. Jay, and G. Crawford. Liquid-crystal materials find a new order in biomedical applications. *Nat. Mater.*, 6:929–938, 2007.
- [53] T. White and D. Broer. Smectic phase in suspensions of gapped dna duplexes. *Nat. Mater.*, 14:1087–1098, 2015.
- [54] M. Salamonczyk, J. Zhang, G. Portale, C. Zhu, E. Kentzinger, J. Gleeson, A. Jakli, C. De Michele, J. Dhont, S. Sprunt, and E. Stiakakis. Smectic phase in suspensions of gapped dna duplexes. *Nat. Commun.*, 7:13358, 2016.
- [55] G. Vroege and H. Lekkerkerker. Phase transitions in lyotropic colloidal and polymer liquid crystals. *Rep. Prog. Phys.*, 55:1241–1309, 1992.
- [56] M. Fixman. Dynamics of semidilute polymer rods: An alternative to cages. *Phys. Rev. Lett.*, 55:2429–2432, 1985.
- [57] A. Perera and G. N. Patey. The solution of the hypernetted-chain and Percus–Yevick approximations for fluids of hard spherocylinders. *J. Chem. Phys.*, 89(9):5861–5868, 1988.
- [58] Hartmut Graf and Hartmut Löwen. Density functional theory for hard spherocylinders: Phase transitions in the bulk and in the presence of external fields. *J. Physics: Condens. Matter*, 11(6):1435, 1999.
- [59] H. Hervet, L. Léger, and F. Rondelez. Self-diffusion in polymer solutions: A test for scaling and reptation. *Phys. Rev. Lett.*, 42:1681–1684, 1979.
- [60] J. F. Maguire, J. P. McTague, and F. Rondelez. Rotational diffusion of sterically interacting rodlike macromolecules. *Phys. Rev. Lett.*, 45:1891–1894, 1980.
- [61] K. Zero and R. Pecora. Rotational and translational diffusion in semidilute solutions of rigid-rod macromolecules. *Macromolecules*, 15:87–93, 1982.
- [62] P. Cobb and J. Butler. Simulations of concentrated suspensions of rigid fibers: Relationship between short-time diffusivities and the long-time rotational diffusion. *J. Chem. Phys.*, 123:054908, 2005.

- [63] Y. Tao, W. den Otter, J. Padding, J. Dhont, and W. Briels. Brownian dynamics simulations of the self- and collective rotational diffusion coefficients of rigid long thin rods. *J. Chem. Phys.*, 122:244903, 2005.
- [64] Y. Tao, W. den Otter, J. Dhont, and W. Briels. Isotropic-nematic spinodals of rigid long thin rodlike colloids by event-driven brownian dynamics simulations. *J. Chem. Phys.*, 124:134906, 2006.
- [65] W. Yan, H. Zhang, and M. Shelley. Computing collision stress in assemblies of active spherocylinders: Applications of a fast and generic geometric method. *J. Chem. Phys.*, 150:064109, 2019.
- [66] P.G. Bolhuis, A. Stroobants, D. Frenkel, and H.N.W. Lekkerkerker. Numerical study of the phase behavior of rodlike colloids with attractive interactions. *Journal of chemical physics*, 107(5):1551–1564, 1997.
- [67] Mihai Anitescu, James F Cremer, and Florian A Potra. Formulating three-dimensional contact dynamics problems. *Journal of Structural Mechanics*, 24(4):405–437, 1996.
- [68] A. Perera, S. Ravichandran, M. Moreau, and B. Bagchi. Single particle and collective orientational relaxation in an anisotropic liquid near the isotropic–nematic transition. *J. Chem. Phys.*, 106:1280–1283, 1997.
- [69] B. Berne and R. Pecora. *Dynamic light scattering*. Wiley, New York, 1976.
- [70] H. Löwen. Brownian dynamics of hard spherocylinders. *Phys. Rev. E*, 14:1232–1242, 1994.
- [71] D. Saintillan and M. Shelley. Orientational order and instabilities in suspensions of self-locomoting rods. *Phys. Rev. Lett.*, 99, 2007.
- [72] Stavros D Peroukidis, Ken Lichtner, and Sabine HL Klapp. Tunable structures of mixtures of magnetic particles in liquid-crystalline matrices. *Soft Matter*, 11(30):5999–6008, 2015.
- [73] D. Frenkel and J. Maguire. Molecular dynamics study of the dynamical properties of an assembly of infinitely thin hard rods. *Mol. Phys.*, 49:503–541, 1983.
- [74] J. Rallison. Brownian diffusion in concentrated suspensions of interacting particles. *J. Fluid Mech.*, 186:471–500, 1988.

- [75] Masao Doi. Molecular dynamics and rheological properties of concentrated solutions of rodlike polymers in isotropic and liquid crystalline phases. *Journal of Polymer Science: Polymer Physics Edition*, 19(2):229–243, 1981.
- [76] J Feng, CV Chaubal, and LG Leal. Closure approximations for the doi theory: Which to use in simulating complex flows of liquid-crystalline polymers? *Journal of Rheology*, 42(5):1095–1119, 1998.
- [77] E. M. Purcell. Life at low reynolds number. *Am. J. Phys.*, 45:3–11, 1977.
- [78] E. Lauga and T. Powers. The hydrodynamics of swimming microorganisms. *Reports on Progress in Physics*, 72(9):096601, 2009.
- [79] J. Teran, L. Fauci, and M. Shelley. Viscoelastic fluid response can increase the speed and efficiency of a free swimmer. *Phys. Rev. Lett.*, 104:038101, 2010.
- [80] B. Thomases and R. Guy. Mechanisms of elastic enhancement and hindrance for finite-length undulatory swimmers in viscoelastic fluids. *Phys. Rev. Lett.*, 113:098102, 2014.
- [81] D. Salazar, A. Roma, and H. Ceniceros. Numerical study of an inextensible, finite swimmer in stokesian viscoelastic flow. *Phys. Fluids*, 28:063101, 2016.
- [82] S. Zhou, A. Sokolov, O. Lavrentovich, and I. Aranson. Living liquid crystals. *Proc. Nat. Acad. Sci.*, 111:1265–1270, 2014.
- [83] O. Lavrentovich. Active colloids in liquid crystals. *Current Opinion in Colloid & Interface Science*, 21:97 – 109, 2016.
- [84] S. Zhou, O. Tovkach, D. Golovaty, A. Sokolov, I. Aranson, and O. Lavrentovich. Dynamic states of swimming bacteria in a nematic liquid crystal cell with homeotropic alignment. *New Journal of Physics*, 19:055006, 2017.
- [85] M. Krieger, S. Spagnolie, and T. Powers. Microscale locomotion in a nematic liquid crystal. *Soft Matter*, 11:9115–9125, 2015.
- [86] M. Krieger, M. Dias, and T. Powers. Minimal model for transient swimming in a liquid crystal. *Eur. Phys. J. E*, 38:94, 2015.
- [87] J. Shi and T. Powers. Swimming in an anisotropic fluid: How speed depends on alignment angle. *Phys. Rev. Fluids*, 2:123102, 2017.

- [88] M. Krieger, S. Spagnolie, and T. Powers. Swimming with small and large amplitude waves in a confined liquid crystal. *J. Non-Newtonian Fluid Mech.*, 273:104185, 2019.
- [89] J. Feng and L. Leal. Simulating complex flows of liquid-crystalline polymers using the doi theory. *J. Rheol.*, 41:1317–1335, 1997.
- [90] L. Fauci and C. Peskin. A computational model of aquatic animal locomotion. *Journal of Computational Physics*, 77:85–108, 1988.
- [91] R. G. Larson. *The Structure and Rheology of Complex Fluids*. Oxford University Press, New York, 1999.
- [92] Pilhwa Lee and Charles W Wolgemuth. An immersed boundary method for two-phase fluids and gels and the swimming of *caenorhabditis elegans* through viscoelastic fluids. *Physics of Fluids*, 28(1):011901, 2016.
- [93] Lisa J Fauci and Charles S Peskin. A computational model of aquatic animal locomotion. *Journal of Computational Physics*, 77(1):85–108, 1988.
- [94] Charles S Peskin. The immersed boundary method. *Acta numerica*, 11:479–517, 2002.
- [95] T Vaithianathan and Lance R Collins. Numerical approach to simulating turbulent flow of a viscoelastic polymer solution. *Journal of Computational Physics*, 187(1):1–21, 2003.
- [96] Daniel Salazar, Alexandre M Roma, and Hector D Ceniceros. Numerical study of an inextensible, finite swimmer in stokesian viscoelastic flow. *Physics of Fluids*, 28(6):063101, 2016.
- [97] Eric Lauga. Propulsion in a viscoelastic fluid. *Physics of Fluids*, 19(8):083104, 2007.
- [98] J Feng and LG Leal. Simulating complex flows of liquid-crystalline polymers using the doi theory. *Journal of Rheology*, 41(6):1317–1335, 1997.
- [99] T. Gao and Z. Li. Self-driven droplet powered by active nematics. *Phys. Rev. Lett.*, 119:108002, 2017.
- [100] T. Gao, M. Betterton, A. Jhang, and M. Shelley. Analytical structure, dynamics, and coarse-graining of a kinetic model of an active fluid. *Phys. Rev. Fluids*, 2:093302, 2017.

- [101] G.I. Taylor. Analysis of the swimming of microscopic organisms. *Proc. R. Soc. Lond. Ser. A*, 209:447, 1951.
- [102] Eric Lauga. Propulsion in a viscoelastic fluid. *Phys. Fluids*, 19(8):083104, 2007.
- [103] X. Shen and P. Arratia. Undulatory swimming in viscoelastic fluids. *Phys. Rev. Lett.*, 106:208101, 2011.